VILNIUS UNIVERSITY
CENTER FOR PHYSICAL SCIENCES AND TECHNOLOGY

Jurgis Pilipavičius

AMORPHOUS SILICA-BASED CARBON NANOTUBE AND SILVER NANOPRISM COATINGS: SYNTHESIS AND INVESTIGATION OF THEIR OPTICAL PROPERTIES

Doctoral Dissertation
Physical Sciences, Chemistry (03 P)

Vilnius, 2016

The dissertation was carried out in Vilnius University in the period of 2011-2015

Scientific supervisor:

Prof. (HP). Dr. Aldona Beganskienė

(Vilnius University, Physical Sciences, Chemistry 03P)

CONTENTS

List of Abbreviations

AEAPTMS – N-[3-(trimethoxysilyl)propyl]ethylenediamine
AFM – atomic force microscopy
AgNP – silver nanoparticle
AgNPR – silver nanoprism
APTES – (3-aminopropyl)triethoxysilane
ATR – attenuated total reflectance
BSPP – bis(p-sulfonatophenyl) phenylphosphine dihydrate dipotassium salt
CA – contact angle
CNT – carbon nanotube
CTAB – cetyltrimethylammonium bromide
CTAT – cetyltrimethylammonium p-toluenesulfonate
CVD – chemical vapor deposition
DDA – discrete dipole approximation
DLS – dynamic light scattering
DMF – N,N-dimethylformamide
DNA – deoxyribonucleic acid
DOS – density of states
dsDNA – double stranded DNA
DWCNT – double-walled carbon nanotubes
EM – electromagnetic field
FMN – flavin mononucleotide
FTIR – Fourier transform infrared spectroscopy
FWHM – full width at half maximum
HiPco – high-pressure CO conversion
LSPR – localized surface plasmon resonance
MHA – 16-mercaptohexadecanoic acid
MPTMS – (3-mercaptopropyl)triethoxysilane
MWCNTs – multi-walled carbon nanotubes
NaC – sodium cholate
NLO – nonlinear optics
NMP – N-Methyl-2-pyrrolidone
NP – nanoparticle
NPR – nanoprism
NSL – nanosphere lithography

OTMS – octadecyltrimethoxysilane
P4VP – poly(4-vinylpyridine)
PAH – polycyclic aromatic hydrocarbons
PAMAM – polyamidoamine
PDMS – polydimethylsiloxane
PEF – plasmon-enhanced fluorescence
PEG – polyethylene glycol
PL – photoluminescence
PSSS – poly(sodium styrenesulphonate)
PVA – poly (vinyl alcohol)
PVP – poly (vinylpyrrolidone)
RBM – radial breathing mode
SA – saturable absorber
SDBS – sodium dodecylbenzenesulfonate
SDS – sodium dodecylsulfate
SEIAS – surface-enhanced infrared absorption spectroscopy
SEM – scanning electron microscope
SERS – surface enhanced Raman scattering
SESAM – semiconductor saturable absorber mirror
SFE – surface free energy
SP – surface plasmons
SPP – surface plasmon polariton
SPR – surface plasmon resonance
SWCNT – single-walled carbon nanotube
TEM – transmission electron microscopy
TEOS – tetraethoxysilane
TMOS – tetramethoxysilane
TPA – two-photon absorption

Chapter 1. Introduction

The deeper understanding in the manipulation on materials structure and properties at the nanoscale delivers new gateways and great opportunities in creating innovative materials having exclusive performance. Application of new generation materials such as advanced liquid crystals, functional polymers, and nanostructures, including carbon nanotubes (CNTs) and plasmonic nanoparticles may provide good cost to performance ratio and high flexibility in manufacturing of various devices.

The increased knowledge in production of new miniaturized photonic components having good performance to cost ratio opened new possibilities for integrated optics, such as high performance laser sources on small chip-based devices. Generally, nanosecond or picosecond laser sources are primary choice for many scientific, and industrial applications. The ultra-short laser pulses can be generated by passive mode-locking technique where the main component is saturable absorber (SA). Efficient SA should have strong nonlinearity, fast response time, broad wavelength range, high power handling, low cost and should be easily integrated into an optical system. Currently used semiconductor saturable absorber mirrors (SESAMs) does not satisfy these all criteria. Semiconducting single-walled carbon nanotubes (SWCNTs) exhibit strong optical absorption in a spectral range from UV to near IR and already showed a high potential in laser mode locking [1-3]. SWCNTs have fast response time, low optical loses and strong non-linearity. Moreover, they can be integrated in optical component as a polymeric composite film, which provides compact setup of the optical system [4]. However, integration of SWCNTs in a polymer or other matrix might be complicated. Typical SWCNTs exist in a form of bundles, containing hundreds of single nanotubes entangled together. SWCNTs have very low solubility in organic and aqueous media. The lack of solubility and the difficult manipulation limits any practical use of SWCNTs.

These obstacles can be overcome through the functionalization of SWCNTs by grafting functional groups to a nanotube surface or wrapping by the polymers or surfactants. However, the polymer matrix has its own drawbacks – it will degrade in more extreme conditions such as high temperature or high intensity light irradiation. Thus, inorganic matrix such as silica may provide much higher stability for SWCNTs composites. The sol-gel process provides the ability to prepare such composites in a cost effective wet chemistry approach. To date, only few reports are published representing SWCNT-silica composite preparation via sol-gel process [5]. Combining colloidal silica and SWCNTs which have completely different chemical ant physical properties is not a trivial task. Thus, the production of such composites should be studied in more detail.

Over the past few decades, numerous significant achievements were made in noble metal nanoparticle research. Success in the development and production of new metal nanostructures opened new possibilities for molecular sensing [6], novel optical materials [7, 8], integrated circuits [9-11], communications [12] and cancer treatment [13-15]. Most of these applications are based on unique optical properties of metal nanoparticles such as localized surface plasmon resonance (LSPR). Depending on size and origin of the particles LSPR of spherical noble metal nanoparticles typically occurs in near-UV and visible light region. By introducing anisotropy into particle shape, it is possible to shift LSPR to NIR region.

A great deal of recent scientific interest is concentrated in the field of laser-matter interaction [4] and underlying physical phenomena, where optical fields tune the properties of the matter and the response becomes nonlinear. The natural interest in metal nanoparticales, nanoapertures in metal films and metamaterials comes from the possibility of enhancing local electromagnetic fields which can enormously facilitate weak nonlinear light-matter interactions [6, 7]. Anisotropic silver nanoparticles, such as silver nanoprisms (AgNPRs), exhibit strong LSPR in 600 – 1200 nm range, which is important for application in surface-enhanced Raman spectroscopy (SERS). Currently many studies are directed towards plasmon driven

SERS materials [16-21]. Successful application of SERS nanomaterials in determination of otherwise untraceable amounts of molecules is well known [22-25]. However, more quantitative analysis and higher versatility in the determination of various molecules is still in need. Nanomaterials prepared by lithography stands out for their reproducible SERS enhancements whereas materials made by chemical approaches have considerably higher SERS enhancements and are less expensive. Production of uniform colloidal silver nanoparticle layers on a solid surface could be the method of choice, since it combines high enhancement typical to colloidal nanoparticles as well as increased repeatability due to uniform SERS substrate layers.

Due to the strong interactions between nitrogen atom and silver nanoparticle surface it is possible to deposit high-density AgNPRs layers on the amino group rich solid surface. Such surfaces can be prepared via silanization process by using alkoxysilanes having amino or thiol groups. This approach may provide cost effective synthesis of high efficiency SERS substrates. However, exist only few studies related to self-assembly of AgNPRs on functionalized surface [26]. Therefore, the comprehensive study of AgNPRs self-assembly on functionalized surface is in demand.

Scientific novelty:

1. It was shown, that silica matrix improves thermal stability of SWCNT, therefore such composites may be applied in high intensity laser systems.
2. Was suggested effective method for preparation of amine group functionalized surfaces by preparing hybrid silica-APTES coatings, which allows to tune amino group content on the coating.
3. In thesis for the first time was presented comprehensive study of AgNPRs self-assembly on amino group functionalized surface.
4. It was shown, that the use of hybrid silica-APTES coatings provides more controllable AgNPRs self-assembly process.

At the present, the new preparation methods of AgNPRs or SWCNTs composites have importance not only in scientific area but also in high-tech industry applications. Therefore, **the aims of this doctoral dissertation is as follows*:***

1. Prepare and SWCNT-silica composite coatings via sol-gel route and investigate their optical properties.
2. Investigate optical properties of AgNPRs, find the optimal synthesis conditions for preparation of self-assembled AgNPRs layers and investigate their performance in SERS.

For this reason, there were formulated tasks as follows:

1. Investigate the solubility of SWCNTs in alcohol media by using different surfactants and examine a saturable abortion of different type of SWCNTs.
2. Prepare SWCNT-silica composite coatings via sol-gel route, characterize their morphology, optical properties and thermal stability.
3. Optimize AgNPRs synthesis conditions and investigate their nonlinear optical properties.
4. Investigate self-assembly of AgNPRs on silanized surface containing different functional groups at different silanization conditions.
5. Prepare hybrid silica-APTES ((3-aminopropyl)triethoxysilane) coatings, investigate the influence of functional group content, particle size effects to the assembly of AgNPRs and evaluate the performance in SERS of self-assembled AgNPRs.

Statements of defense:

1. Semiconductive nanotubes have lower saturation energy and non-saturable loses compared to unsorted SWCNTs.
2. SWCNT-silica composite coatings demonstrate higher thermal stability compared to SWCNT-P4VP (poly(4-vinylpyridine)) coatings.

3. AgNPRs demonstrate third-order optical nonlinearities including both positive nonlinear absorption and saturable absorption. Which effect taking place is determined by particle lateral dimensions.
4. Most uniform and dense self-assembled AgNPRs layers forms on surfaces silanized by APTES.
5. Prepared hybrid silica-APTES coatings provides the tuneability of amino group content on the surface resulting in more controllable AgNPRs deposition process.

Chapter 2. Carbon Nanotubes: Properties, Application and Chemical Functionalization

Carbon atoms distinguish the unique ability to form robust covalent bonds between one another or other nonmetals in different hybridization states, like sp, sp^2 or sp^3, which result broad range of structures from nano to macro scale. This particular property is fundamental in organic chemistry and biochemistry. Moreover, the carbon itself may form wide range of well-known allotropes such as amorphous carbon, diamond, graphite as well as nanoscale allotrope structures like graphene, fullerenes, single-walled and multi-walled nanotubes (SWCNTs and MWCNTs), nanohorns, carbon dots, graphene quantum dots, nanodiamonds [27] (figure 1). Generally, latter nanostructures are categorized as 0D, 1D, 2D or 3D dimension structures. Thus, a piece of graphene sheet could in principle be wrapped up to form the 0D fullerene, rolled up to form a 1D SWCNT, or stacked with additional sheets of graphene to form multilayered 2D carbon nanosheets or graphite.

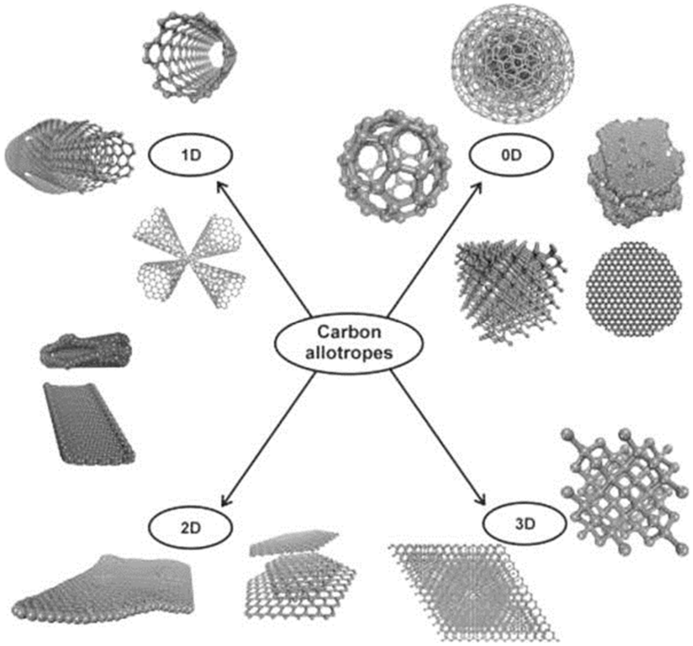

Figure 1. Representation of possible carbon allotropes [27].

2.1. Structure, classification, and electronic properties of carbon nanotubes

One of the major steps in the development of carbon nanostructures was the discovery of carbon nanotubes by *Ijima* [28]. Contrary to other carbon nanostructures, specific size, and shape of the carbon nanotubes result in completely different electrical, optical and chemical properties. The general term "Carbon nanotubes" covers a broad range of tubular nanostructures with similar structures and shapes. Ideally, these structures have a hexagonal lattice of sp^2 carbon atoms, which is rolled in a cylindrical tube. CNTs can be single-walled, double-walled (DWCNT) or multi-walled. Size and shape determines the properties of these nanomaterials, which can strongly differ from one another. SWCNTs are considered as tubes having a wall thickness of one atom and diameter ranging from 0.6 to 4 nm. The length of tube can vary from few hundred nanometers up to 1 mm. MWCNTs are larger, and consist of many single-walled tubes stacked one inside the other and may have a total diameter up to 15 nm. These concentric nanotubes are held together by van der Waals forces.

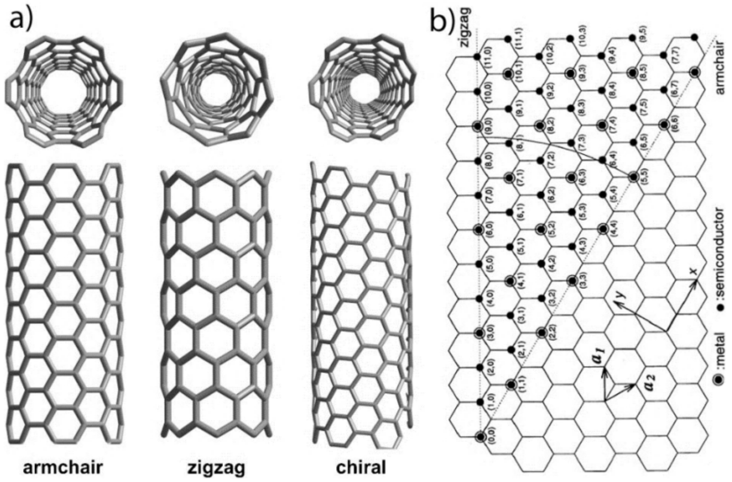

Figure 2. Molecular models of SWCNTs exhibiting different chiralities a) and schematic representation of b) formation of SWCNTs by rolling of a graphene sheet along lattice vectors [29, 30].

Another important factor describing the structure of CNTs is nanotube chirality. CNTs can exhibit three different possible chiralities – zigzag, armchair and chiral conformations (figure 2) [29]. The tube chirality is defined as a chiral vector C_n ($C_n = \mathbf{m}a_1 + \mathbf{n}a_2$), which determines the direction of rolling a graphene sheet, in which a lattice point (m, n) is superimposed with an origin defined as (0, 0). It also determines the tube diameter *d* of SWCNT, which can be expressed as:

$$d = \frac{a\sqrt{m^2 + mn + n^2}}{\pi}$$

where $a = 1.42\sqrt{3}$Å is lattice constant of graphene layer [30, 31]. Value 1.42 corresponds to the C-C bond distance of sp^2 hybridization. Theoretically, all armchair nanotubes, as well as zigzag cylinders having *m* and *n* values multiples of three are metallic. In fact, SWCNTs can be either metallic or semiconducting depending on *n, m* values, although there is no difference on chemical bonding or doping in carbon nanotube skeleton. The unique electronic properties of CNTs are caused by the quantum confinement of electrons normal to nanotube axis. In the radial direction, electrons are confined by monolayer thickness of graphene sheet, which allows electrons propagate only along tube axis. This results in a number of one-dimensional conduction and valence bands, which effectively depend on the standing waves that are present around the circumference carbon nanotube. The sharp intensities (spikes) that are visible in the density of states (DOS) of the tubes are known as van Hove singularities and are the result of this one-dimensional quantum conduction (figure 3) that is not present in an infinite graphite crystal.

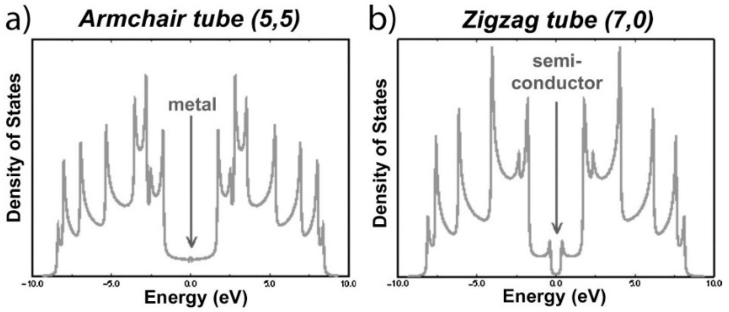

Figure 3. Density of states (DOS) exhibiting the valence, the conduction band and the Fermi energy for (a) metallic armchair (5, 5) tube and (b) zigzag semiconducting tube [29].

In fact, the CNTs may exhibit superior electrical properties. Early observations showed exclusive properties such as ballistic conductance – electron transport without scattering [32, 33]. At low temperature the 1D structure of nanotubes also leads to strong many-body effects, such as a Luttinger liquid. In fact, some nanotube devices show the properties, which follow the predicted Luttinger liquid behavior [34-36].

For ballistic transport, the relation between the current (I) and the voltage (V) is $I=GV$, where G is the quantum conductance. Because a metallic nanotube has two extended electron bands crossing at the Fermi level, it should behave as an ideal two-channel ballistic conductor: every electron injected into it should pass through without scattering. In theory, at larger electron energies, the electrons are able to probe additional bands, which would give a corresponding increase in G. In practice, the propagating electrons will be scattered by lattice defects and eventually by phonons, and the transfer of electrons must proceed through contacts, which can also induce strong scattering [37].

Due to the sp^2 hybridization of carbon nanotubes, they have a higher tensile strength than steel and Kevlar. These carbon-carbon bonds are even stronger than the sp^3 bond found in diamond. Theoretically, SWCNTs may have a tensile strength hundreds of times stronger than steel. Carbon nanotubes also distinguish its elasticity – they can hold high force and press sitting and when exposed to great axial compressive forces, it can bend, twist, kink without damaging the nanotube structure [38]. However, the elasticity of CNTs have its limits – under very physically powerful forces presses, it is possible to permanently deform the original shape. Deformation induced defects in the nanotube structure can weaken a CNTs strength and change electrical and optical properties [38].

2.2. Optical properties of SWCNTs

The optical properties of SWCNTs are determined by their electronic structure, mainly depends on nanotube radius, length, chirality and structural defects. Optical absorption of SWCNTs usually appears with peaks in the far-ultraviolet (~200 nm) to the near-infrared (~2500 nm) regions of the spectrum.

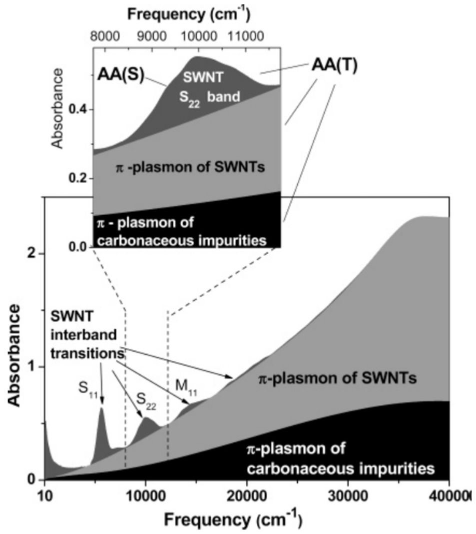

Figure 4. Schematic illustration of the electronic spectrum of a typical SWCNT sample produced by the electric arc method. The inset shows the region of the S22 interband transition utilized for NIR purity evaluation [39].

Displayed peaks represent particular electronic transitions from the valence to conduction bands [40]. These transitions usually appear as sharp bands and can be used to identify the type of SWCNTs [39, 41-43]. Due to flocculation, aggregation and bundling, broadening of peaks may occur. The bundling may strongly affect photoluminescence [43], but it has much weaker effect on optical absorption and Raman scattering. Therefore, latter two techniques are widely used in quality determination of SWCNTs. Figure 4 shows a schematic illustration of typical absorption spectrum SWCNTs sample, where characteristic abortion SWCNTs and carbonaceous impurities shown in different colors. However, it is not yet possible to analytically separate these contributions [44]. The π-plasmon absorption from both SWCNTs and carbonaceous impurities dominates at the high energies, and gradually decrease on the far-IR region. On the NIR-visible region of the spectrum SWCNTs shows characteristic absorption peaks, resulting from the interband transitions of semiconducting and metallic SWCNTs and the background arising from π-plasmons. The type, purity and quality of SWCNTs can be evaluated by analyzing and comparing these features [39, 44].

Raman spectroscopy is the most widely used method for characterization of CNTs. SWCNTs has resonant Raman scattering – the signal obtained is only from CNTs having one of the bandgaps which matches the wavelength of exciting laser. Moreover, this resonance can lead to greatly enhanced intensity of the Raman scattering, which enables to probe SWCNTs in low concentrations, and detect minor defects in its structure [45]. SWCNTs have characteristic features in Raman spectra, which differs from double-walled or multi-walled CNTs. It is practically insensitive to bundling, which facilitates the sample preparation. Moreover, this technique can be used in determination of SWCNT type, chemical changes, structural defects and deformations.

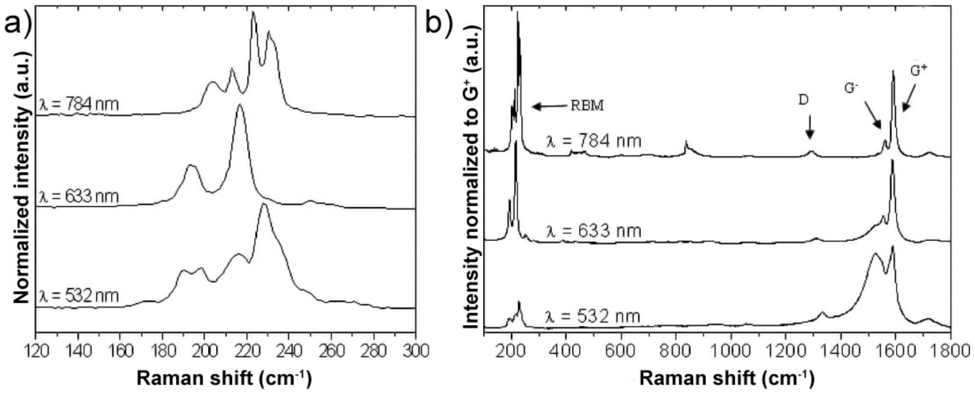

Figure 5. Raman scattering spectra of SWCNTs measured with different excitation wavelengths: a) RBM region and b) D and G regions [46].

Typical Raman spectrum of SWCNT contains particular modes which represents their structural properties (figure 5). It should be noted, that intensities of these modes strongly depend on the laser excitation wavelength. This is related to resonant scattering – at particular wavelength some modes are more excited than others. The radial breathing mode (RBM) typically observed in low frequency (100 – 300 cm^{-1}) spectral region and it corresponds to radial expansion-contraction of the nanotube lattice. Its frequency depends on the diameter of SWCNTs and if the intensity of RBM mode is relatively strong, the overtone of can be observed in double frequency. Therefore, the RBM mode can be used in determination of the diameter of nanotube and/or dispersity of the sample. However, bundling of nanotubes also affects the RBM mode, consequently the evaluation of nanotube diameter requires well dispersed sample [47].

Another important mode is D (Disorder-Induced Feature) mode which typically occurs in 1200 – 1400 cm^{-1} spectral region. This mode arises from structural defects in SWCNT lattice and usually present in all graphitic carbon structures. In fact, this mode is especially common in SWCNTs prepared by arc discharge, laser ablation and various CVD techniques [46, 48-50], which conclude that defect-free SWCNTs barely exist. Nevertheless, recently published paper presents more sophisticated method, which shows, that is possible to produce defect-free SWCNTs [51]. The D mode is also important, when covalent chemical functionalization of SWCNTs is involved. The increased intensity of latter mode helps to evaluate the quantity of defects caused by functionalization. However, there is no direct relation between functionalization degree of SWCNTs and D mode signal intensity, and usually requires additional evaluation techniques.

The great importance mode observed in 1540 – 1595 cm^{-1} spectral region is called G mode (Tangential Mode), which corresponds to the graphite E_{2g} phonon, an optical in-plane vibration. This mode is observed in all graphite-like carbon structures, but in case of SWCNT the mode is typically observed in lower frequencies relative to graphite. The longitudinal and the transverse optical phonons in graphite at the Γ point (a point in Brillouin zone) are equivalent and therefore give rise to only one mode in the Raman spectrum. The curvature of the tube wall in nanotubes, causes a rehybridization of the carbon valence orbitals from sp^2 (planar graphene) to sp^3-like. This results splitting of G mode into two, the G^- and G^+ modes [52] and are respectively related to the circumferential (TO) and axial (LO) atomic vibrations. As the splitting of D mode depends on the tube-wall curvature, it has a small frequency dependence on tube diameter that can be used to append the diameter information obtained from the RBM mode. The intensity of

TO and LO peaks are also dependent on chiral angle for both metallic and semiconducting tubes.

The most important feature of the TO peak is the strong peak shape dependence on the type of tube and its doping. Peak of circumferential TO mode in semiconducting SWCNT observed in lower frequency (takes place of G^- peak) than the axial LO mode (takes place of G^+ peak). In metallic tubes is typically visible opposite effect – the LO mode is visible in higher frequency (takes place of G^+ peak) than the TO mode (takes place of G^- peak) and it exhibits a broad and asymmetric peak shape. The ratio between G^+ and G^- mode reveals, weather the CNT is semiconducting or metallic [53]. However, the assignment is not that simple and metallic tubes can exhibit a “semiconducting-like” G band. Asymmetric G^- band in metallic tubes has been used to identify doping effects – due to changes in the Fermi level the band broadens/sharpens and increases/decreases in intensity. The doping changing the position of G^+ peak – peak shifts positively for donor doping and negatively for acceptor doping. Typically doping does not impact D^+ peak shape. This applies for both semiconducting and metallic tubes, although the frequency shift vs. doping behavior is not yet established quantitatively or even well understood [47].

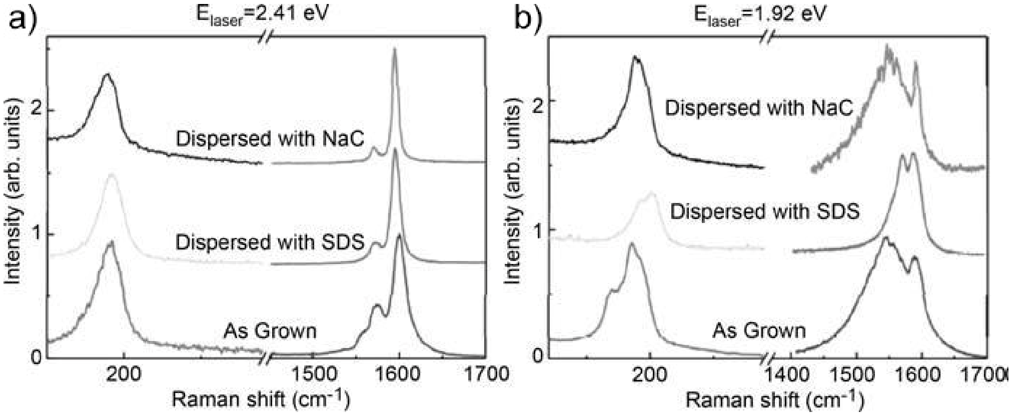

Figure 6. Raman spectra of SWCNTs in bundles as-grown, and dispersed in aqueous solution with two different surfactants (SDS and NaC), obtained with two different excitation laser energies: a) metallic SWCNTs, and b) semiconducting SWCNTs [47].

The other interesting effect of the G band is related with changing the tube environment. The left panel in figure 6 shows a peak broadening when comparing isolated and bundled semiconducting tubes, and this effect can be used for dispersability characterization [54]. Moreover, the considerable broadening of the G^+ band may also indicate the presence of defective material and/or amorphous carbon. This effect is related to the observation of the D mode, already discussed above. In fact, the ratio of D and G^+ modes linewidth reveals the defective structure and is generally used for primary evaluation of SWCNTs quality. The more defective is the material, the larger and broader the D band, and the larger intensity ratio of D and G bands. However, mentioned effects can't be used for quantitative analysis of metal/semiconducting, doping and dispersability characterizations based on the G-band profile.

As already mentioned, SWCNTs have strong optical absorption in a broad spectral range from UV to near IR, and their band gap varies inversely with diameter, which can be tuned by modifying the growth parameters. Isolated semiconducting SWCNTs and small SWCNT bundles exhibit photoluminescence (PL) in the near-IR spectral range. PL is strongly quenched as the bundle size increases, which increases the probability of having metallic SWCNTs near semiconductive SWCNTs. The PL properties of SWCNTs have been extensively investigated over the past few years, and the excitonic nature of electronic transitions in SWCNTs has been theoretically predicted and experimentally proved. Sub-picosecond carrier relaxation time has also been observed in SWCNTs. In addition, they show significant third-order optical nonlinearities, as theoretically predicted and experimentally confirmed [4, 47].

2.3. Saturable absorption of SWCNTs

Saturable absorption is a one of the nonparametric nonlinear optical processes and therefore optical nonlinearity must be described in more detail. Nonlinear optical phenomena are “nonlinear” in the sense that they occur when the response of a material system to an applied optical field depends in a nonlinear manner on the strength of the optical field. Let us consider how the dipole moment per unit volume, or polarization P, of a material system depends on the strength E of an applied optical field. In the case of linear optics, the induced polarization depends linearly on the electric field strength in a manner that can often be described by the relationship [55]:

$$P = \varepsilon_0 \chi E$$

where constant χ is the dielectric susceptibility, and ε_0 is the permittivity of free space. When high electric fields are applied, nonlinear optical process becomes apparent and first equation is not sufficient to fully describe total response. Instead, polarization has to be expressed as a power series in the electric field:

$$P = \varepsilon_0 (\chi_1 E + \chi_1 E^2 + \chi_1 E^3 + \cdots$$

where, χ_1 is the linear susceptibility, while χ_2 and χ_3 are the second- and third-order nonlinear susceptibilities. Second order nonlinearities can be associated with second-harmonic generation, sum- and difference-frequency generation, optical parametric oscillation, while third order nonlinearities a related to nonlinear phenomena such as third-harmonic generation, self-focusing, saturable absorption, two-photon absorption, etc.

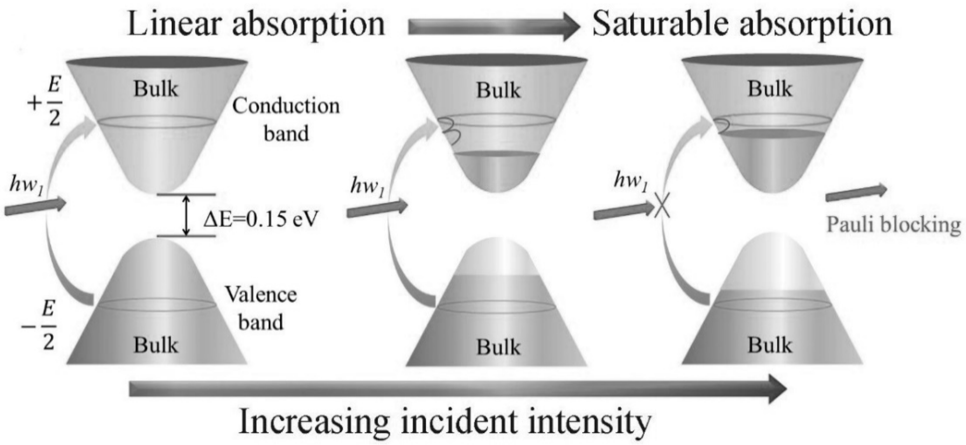

Figure 7. Schematic representation of saturable absorption phenomena in direct bandgap semiconductors [56].

In direct bandgap semiconductors at wavelengths near the bandgap energy the change in absorption and refractive index with intensity is particularly large. Increased intensity of propagating light induces a photoexcitation which causes the states near the edge of the conduction and valence bands to fill, and blocks further absorption. Due to restriction of two electrons filling the same state the bandfilling occurs which is responsible to saturable absorption (figure 7). At high enough intensity the semiconductor becomes transparent to light at photon energies just above the bandedge [57]. This process is also called Pauli blocking or phase space filling [58]. The absorption of saturable absorber (SAs) can be described as:

$$\alpha(I) = \frac{\alpha_0}{1 + I/I_{sat}} + \alpha_{ns}$$

where I is intensity of the input optical pulse, $\alpha(I)$ is the intensity-dependent absorption coefficient, α_0 and α_{ns} are the linear limit of saturable absorption and non-saturable absorption, respectively [57, 59]. The saturation intensity I_{sat} is the intensity necessary to reduce the absorption coefficient to half the initial value, considering $\alpha_{ns} = 0$. The recovery time (τ_A) is important property for SAs which defined as the time necessary to reduce the number of carriers by a factor of $1/e$. In general, for SAs a high increment in transmission at higher power irradiation is desirable. Moreover, it is important to have value of α_{ns} as low as possible. This is usually achieved by reducing elastic scattering active material, decreasing amount carbonaceous impurities and avoiding polymer matrices having absorption at working wavelength, which might increase non-saturable absorption losses. Most materials can show some saturable absorption, but often only with relatively low recovery times and at very high light intensities which may damage the material. At the present, III–V group binary and ternary semiconductors in the form of multiple quantum wells are the most widely used as SAs [60-62]. They are called semiconductor SA mirrors (SESAMs). To date, SESAMs have been widely used in mode-locking of solid-state lasers in a broad spectral range between 800 and 1550 nm. InGaAs/AlAs/ AlAsSb coupled quantum wells used in conventional SESAMs, have third-order nonlinearity of χ^3~5.3×10^{-8} esu (1 esu=1.11×10^{-9} m^2V^{-2}) [63]. SESAMs can typically cover a narrow (several tens of nm) operation wavelength range, consequently they have to be specially designed for each working wavelength. Moreover, production process of SESAMs is quite tedious and has strict fabrication requirements. They are grown on distributed Bragg reflectors by molecular beam epitaxy or metal–organic vapor phase epitaxy and often followed by high-energy heavy-ion implantation to create defects in order to reduce the recovery time [57, 64, 65].

Semiconductive SWCNTs can be used as effective SAs. Reported high third order nonlinearity of SWCNTs, associated with saturable absorption was χ^3~10^{-10} esu and χ^3~10^{-7} esu when carbon nanotube was in resonance mode [3, 66]. These measured nonlinearities are higher than other nanomaterials and semiconductors, which are being investigated, as alternatives for conventional SESAMs. For example, χ^3~10^{-12} esu was reported for $AgInSe_2$ nanorods, ~10^{-8} esu in CdSe, and ~10^{-12} esu in PbS [4, 67, 68].

The choice of SWCNTs is truly becomes important when optimum performance of SAs is targeted. The effective saturable absorption determined by on the number of tubes in resonance with the incident light. As mentioned before, the transition energies of SWCNTs are inversely proportional to the diameter of the nanotube, consequently saturable absorption at a particular wavelength depends on the SWCNTs diameter distribution. As nanotube length has only minor influence to the transition energies it has minor effect to saturable absorption. However, due to higher amount of possible defects on tube ends, shorter tubes might have higher non-saturable loses. Though the SWCNTs has defined transition states, for some incident wavelength deviations up to ~200 nm from the peak resonance, appreciable saturable absorption can be still observed. However, in such conditions, higher laser intensity is needed in order to achieve saturable absorption. This may lead to faster degradation of SAs component followed by decreased performance of a device.

Therefore, the matching of SWCNT absorption band and laser operation wavelength is important.

Different growth methods result in SWCNTs with different diameter distributions, consequently absorption spectra profiles may vary (figure 8) [4, 69-72]. By varying growth parameters and sorting SWCNTs is possible to obtain SAs at desired wavelength. However, the matching can be tedious when desired deviations are in range of ten nanometers. In such case, for example, if device working at telecommunications wavelength (1550 nm) the arc discharge and HiPco (high-pressure CO reduction) synthesized SWCNT may also be used (figure 8), but saturable absorption will be observed in higher laser intensity. Nevertheless, these SWCNTs would show better performance in shorter wavelength working devices, better matching absorption profile [1, 2]. Tuning the SWCNT mean diameter may improve mode-locking and thus increase performance of the device

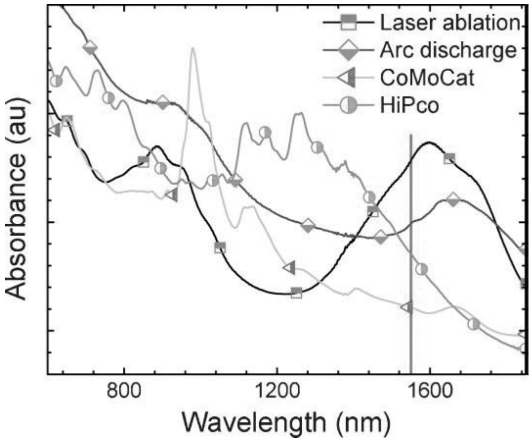

Figure 8. Absorption spectra of SWCNTs grown by different methods, with varying absorption profiles [4].

2.4. Solubilization and functionalization of SWCNTs

As mentioned before, optical properties of nanotubes depend not only on internal structure, but also are influenced by their arrangement. Even though SWCNTs show good nonlinear absorption and have huge potential as SAs, there are some complications, which may decrease the interest of their application. The main complexity is related to SWCNTs insolubility in and bundling. Unlike SESAMs it is not easy to integrate nanotubes in the device. In early implementations production of SWCNTs-based SAs involved the use of dispersed low concentration SWCNTs solutions, spray-coated quartz substrates or even direct deposition of SWCNT films on fiber ends [73-75]. However, these implementations often result increment of non-saturable absorption associated with impurities, particle aggregation, and solvent evaporation. More promising way to produce SWCNT-based SAs is to integrate SWCNT in polymer host [1, 76-78]. Well dispersed SWCNTs in polymer matrix is crucial in SAs fabrication. Production of uniform SWCNT-polymer composite is not a trivial task. Though SWCNTs generally considered insoluble in any solvents it is still possible to obtain dispersions in some aprotic solvents such as dimethylformamide (DMF), N-metylpyrrolidone (NMP) by ultrasonic treatment. However, obtained dispersions typically are in low concentration, not very stable. In fact, in such dispersions, SWCNTs more likely form sub-micrometer bundles rather than individually dispersed tubes. In order to obtain stable, highly concentrated SWCNTs dispersions functionalization of nanotubes must be involved. Carbon nanotubes can be chemically functionalized to improve solubility in various solvents and compatibility with various materials. The main approaches for the functionalization of CNTs can be grouped into two categories, which include the covalent attachment of chemical groups onto p-conjugated skeleton of CNTs and the noncovalent adsorption or wrapping with various functional molecules.

2.4.1. Covalent functionalization of single-walled carbon nanotubes

The covalent functionalization involves attaching of functional groups to tube ends or sidewalls. The tube caps having a semifullerene-like structure distinguish highest chemical reactivity among other CNT sites. Chemical functionalization of CNTs has been carried out mainly by oxidative treatments. Oxidation of CNT generally results opened tubes with oxygen-containing functional groups such as carboxylic acid, at both the sidewall and the tube endings. These groups can then be used as chemical attachment sites for further derivatization. The curvature of the nanotube sidewall is important factor for addition reactions – the cylindrical nanostructure is more favorable than in a flat graphene sheet. In addition, increment of exohedral chemical reactivity with increasing curvature of the sidewall has been showed in several experimental studies. This has been attributed to curvature induced strain that originates from pyramidalization of the sp^2-hybridized carbon atoms and the misalignment of π-orbitals [79].

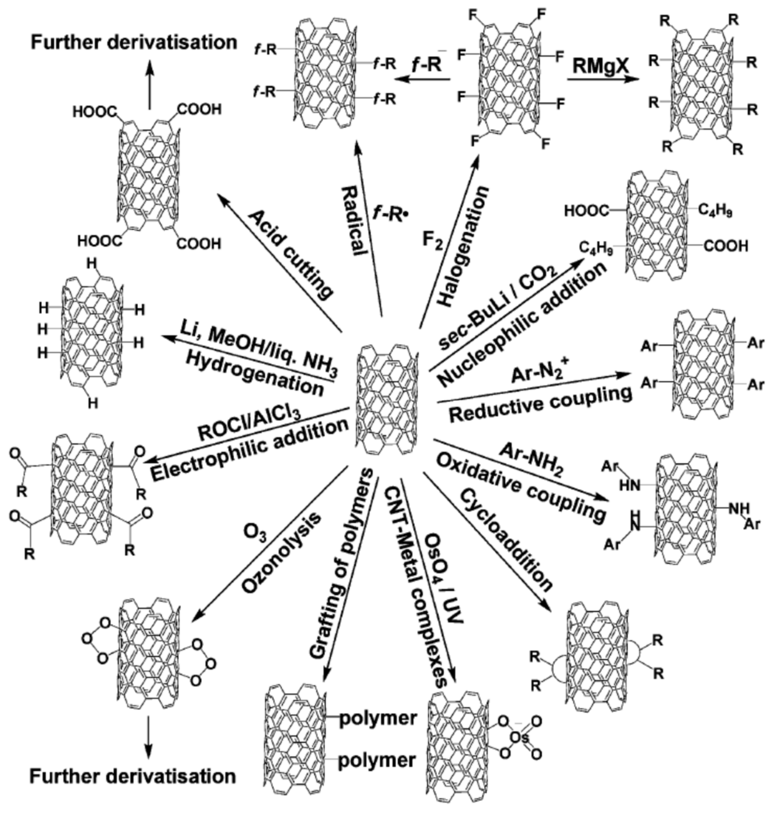

Figure 9. Covalent surface functionalization ways of carbon nanotubes [80].

Presence of structural defects has significant impact to the chemical reactivity of CNTs. As general rule, approximately 2% of the carbon atoms in SWCNTs exist in non-hexagonal rings. The sidewall defects such as vacancies or pentagon-heptagon pairs (Stone-Wales defects) enhance a local chemical reactivity of the CNTs. It should be noted, that covalent sidewall functionalization results in sp^3

carbon sites on CNTs outer structure, which disrupt the band transitions of π electrons, and cause the loss of electrical conductivity, mechanical strength and optical properties. Partial restoring of the CNT structure to the initial stage can be accomplished by thermal treatment of the functionalized tubes at temperatures between 300 and 500 °C [79]. Nevertheless, many applications of CNTs rely on successful surface functionalization. Figure 9 represents various ways of covalent functionalization of CNTs.

Oxidation of CNTs is probably the most widely studied among various surface functionalization techniques. First functionalization methods involved gas-phase oxidation in air and oxidative plasmas [81]. This way simplifies the oxidation procedure by avoiding filtration, washing, and drying steps. However, these techniques give low functionalization degree and generally considered not efficient. Most widely used functionalization oxidation-based technique is performed in liquid-phase. This mainly accomplished by acidic oxidation by nitric acid or sulfuric/nitric acid mixtures. However, loss of SWCNT metallic character was also showed in recent studies. The differentiation of the influence of physical properties for different types of MWCNTs via nitric acid purification and functionalization was demonstrated. The over-oxidation of CNTs by nitric acid was observed which led to exfoliated CNTs fragments [82-84].

Microwave radiation can also be used in the chemistry of CNTs. *Resasco et al.* in their study functionalized SWCNTs sidewalls by carboxylic and sulfonated groups by mixture of nitric and sulfuric acid in help with short time microwave treatment [85]. The functionalized SWCNTs displayed a great dispersibility in deionized water and ethanol. Some reduction in the average length of the nanotubes as well as an enhanced disorder in the sidewalls was also observed. Study also showed decrement in SWCNTs conductivity approximately 30% compared to untreated material. Nevertheless, the conductivity was fully recovered to the initial state after high-temperature treatment under argon atmosphere [86].

The oxidation reaction of piranha (H_2SO_4/H_2O_2) solutions onto SWCNTs was reported by *Ziegler et al.* [87]. Study showed, that high temperature treatment of CNTs with the oxidizing solution induce reaction in existing defect sites, which produce holes in the sidewalls and their accumulation results in shortening of the CNTs. Long reaction times induce considerably shorter nanotubes as well as selective etching of the smaller diameter nanotubes. On the other hand, if the reaction proceeds in room temperature piranha treatment may deliver minimal carbon loss, slow etch rates, and little sidewall damage.

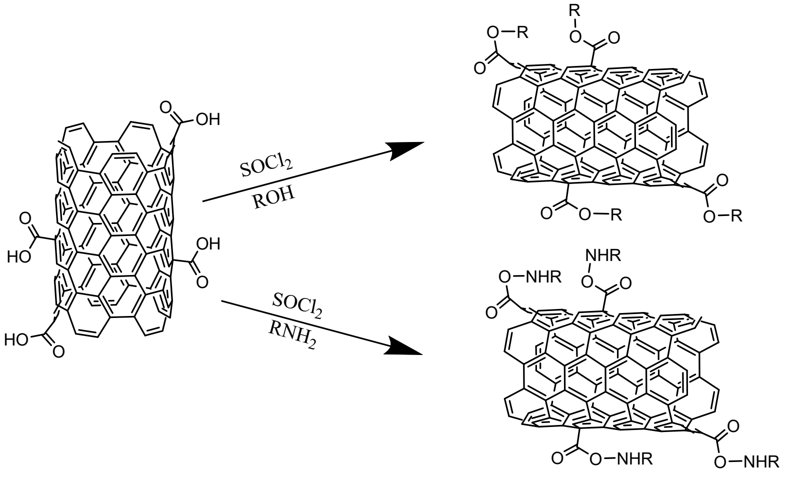

Figure 10. Scheme of CNT esterification and amidation.

Carboxylated CNTs were extensively used as precursors for further covalent modification of CNTs. Generally, it is realized via esterification or amidation reactions (figure 10). Carboxylic groups that are present on the sidewalls and tips of CNTs are converted to acyl chloride groups by introduction of thionyl or oxalyl chloride, followed by the reaction with the appropriate alcohol or amine. A great number of substituents, such as several organic substances, biomolecules, polymers, or photosensitive compounds, can be attached to CNTs by this procedure [88-93]. Grafting CNTs by long polyethylene glycol (PEG) chain is common technique to prepare water soluble CNTs and PEGylated SWCNTs are already commercially available. In order to obtain good solubility in non-polar media CNTs generally modified by long alkyl chains containing amines or alcohols [94, 95].

Some specific substituents such as biomolecules, functional polymers, organic molecules and nanoparticles may be introduced by this way for more advanced applications.

Carbenes and nitrenes can react with CNTs via cycloaddition reactions. *Haddon et al.* was first who employed functionalization of SWCNTs by in situ generated dichlorocarbene in mixture of chloroform/sodium hydroxide. Obtained carboxylate groups on the SWCNTs can be further modified for other applications. 1,3-Cycloaddition of azomethine ylides on the sidewalls of CNTs is well known method for functionalization of SWCNTs. In this way the SWCNTs surface can be modified by a pyrrolidine ring, which can be derivatized by large variety of functional groups such as PAMAM dendrimers, phthalocyanine addends, superhydrophobic perfluoroalkylsilane groups, and ethyleneglycol groups [96-98]. Surface chemical functionalization by introducing azomethine ylide groups containing phenol structures showed higher zeta potential values for functionalized SWCNTs compared to unmodified SWCNTs [99]. Another study demonstrated 1,3-dipolar cycloaddition reaction by using N-methylglycine and 3,4-dihydroxybenzaldehyde. Modified SWCNTs showed good stability in polar solvents dispersions, including water [100].

Radical functionalization of SWCNTs was studied by theoretical calculations and was showed that there is a great probability of reaction of radicals on the sidewalls of CNTs [101]. In fact, covalent sidewall functionalization via radical addition by diazonium salt was proven experimentally. Electrochemical reduction of substituted aryl diazonium salts in organic media generates an aryl radical in situ, which covalently attaches to the surface of SWCNTs [102, 103]. By using water-soluble diazonium salts, which reacts selectively with metallic CNTs, functionalized nanotubes are well dispersed in DMF or aqueous solutions [104, 105].

2.4.2. *Non-covalent functionalization of single-walled carbon nanotubes*

Alternative approach to solubilize the SWCNTs is realized via non-covalent functionalization. In this frame, the surface of SWCNT can be modified in favor of van der Waals forces and π-π interactions. Nanotubes can be wrapped by polycyclic aromatic compounds, surfactants, polymers, or even biomolecules. Contrary to covalent functionalization the non-covalent functionalization not involve direct chemical reactions with sp^2 carbon lattice on CNT sidewall or tube ends. Therefore, the original structure and electronic network of SWCNTs is preserved. In the last decade, preparation of aqueous and organic solutions of SWCNTs via non-covalent surface modification of by surfactants or polymers was widely used. This approach can provide highly stable suspensions of individually dispersed nanotubes. In figure 11 are represented few examples of compounds used for CNTs solubilization in polar and non-polar media.

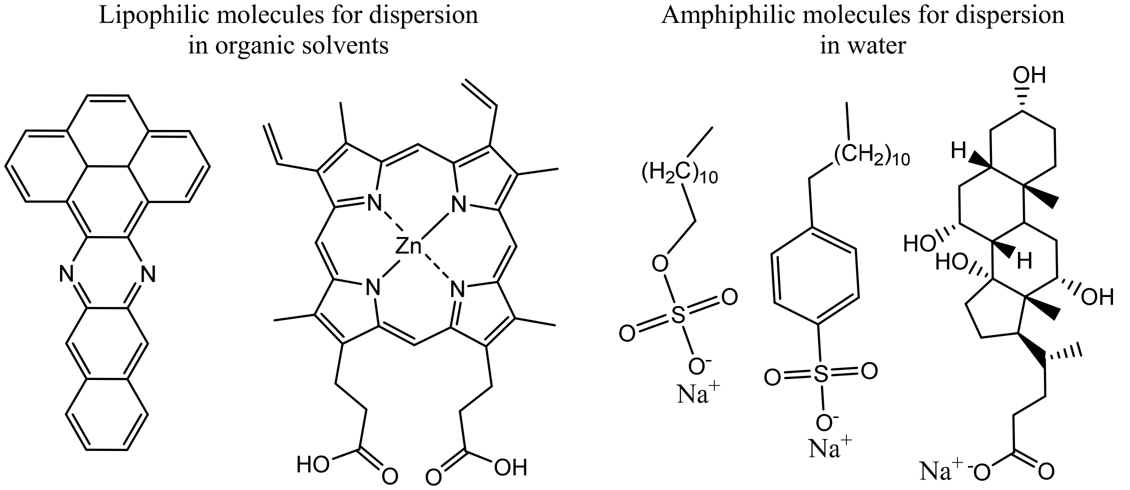

Lipophilic molecules for dispersion in organic solvents

Amphiphilic molecules for dispersion in water

Diazapentacene derivative [106]

Zn-protoporphyrin [107]

SDS [108]

SDBS [109]

NaC [110]

Figure 11. Some examples of compounds used for dispersion CNTs in organic solvents and water.

Due to conjugated π orbitals, aromatic molecules have strong affinity for graphitic surfaces and are widely be used for SWCNTs solubilization in non-aqueous solvents [111]. The adsorption of different polycyclic aromatic hydrocarbons (PAH) such as pyrene, anthracene, tetracene and phenanthrene on

SWCNTs has been extensively investigated. *Zhang et al.* demonstrated existing strong interactions between short SWCNTs and different anthracene derivatives [112]. Another study investigated affinity of tetracene and pentacene to SWCNTs [113]. The strong π–π interactions between PAH and the external SWCNT surface was confirmed by in Raman spectra observed higher frequency shift of the RBM mode. Research showed the remarkable difference between the adsorption amounts of tetracene and phenanthrene which was caused by the nanoscale curvature effect of the tube surface, resulting a difference in the amount of contact between the molecule and the tube surface. Relationship between phenanthrene or naphthalene adsorption to CNTs and the hydrophobicity of the corresponding PAH was demonstrated by *Wang et al.* [114]. Production in of SWCNT stable dispersions in tetrahydrofurane (THF) by introducing diazapentacene and room temperature sonication was also demonstrated [106]. Porphyrins can be also used for preparation SWCNTs dispersions in organic solvents. Study showed that the solid SWCNTs–Zn-protoporphyrin nanocomposite is easily separable from the solution and can be easily redissolved in DMF [107].

Tromp et al. proposed novel physical−chemical method for diameter-selective SWCNT separation. The method is based on noncovalent matching of an appropriate anchor molecule to the wall of the SWCNT [115]. They demonstrated selective separation in the 1−2 nm diameter range using easily synthesized oligo-acene adducts as a diameter-selective molecular anchor. Method offer diameter-selective CNT separation which is simple, effective and that allows up-scaling to large volumes at modest cost.

For preparation of aqueous SWCNT dispersions surfactants are most widely used. Generally, these materials are low cost, commercially available and easily handled. Typical surfactant molecules consist of a hydrophobic tail and a hydrophilic head group, where hydrophobic head interacts with nanotube walls and the hydrophilic with the solvent. In one of the first implementations, CNTs was purified by 1% sodium dodecyl sulfate (SDS) in help of ultrasonic treatment [116].

On SWCNT surface adsorbed SDS molecules debundles SWCNTs and prevents aggregation via electrostatic repulsion between polar heads which interacts with water molecules.

Numerous studies demonstrated successful preparation of stable SWCNT dispersions in water by using ionic and non-ionic surfactants such as sodium dodecylbenzenesulfonate (SDBS), cetyltrimethylammonium bromide (CTAB), cetyltrimethylammonium p-toluenesulfonate (CTAT), and sodium cholate (NaC) by ultrasonic treatment [117]. By using SDBS is possible to obtain SWCNT dispersions up to 0.06% (w/w) in water. Recent study [118] determined binding strengths of the most common surfactants used in solubilization of SWCNTs. Results revealed quantitative binding strengths of surfactants as SDBS > NaC ≈ FMN (Flavin mononucleotide) > SDS, irrespective of electronic types of SWNTs. NaC has been used in sorting water-filled and empty SWCNTs prepared by arc discharge via ultracentrifugation to equilibrium by exploiting a density gradient [110]. Study demonstrated successful separation of different diameter SWCNTs which was identified by absorption and Raman spectra (figure 12).

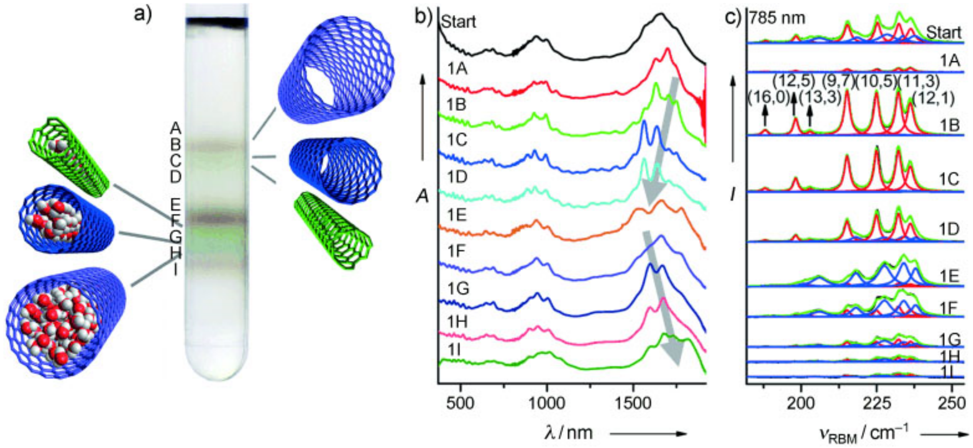

Figure 12. Sorting of empty- and water-filled arc SWCNTs (2% w/v SC). a) Centrifuge tube containing sorted arc SWCNTs; b) Absorption spectra of the original solution and of the sorted fractions; c) Resonance Raman spectra of the different fractions excited at 785 nm [110].

PAH functionalized with hydrophilic ends can be used for solubilization SWCNTs in water and non-covalent functionalization to provide particular functionalities [119, 120]. A water soluble perylene derivatives has been used to exfoliate and suspend SWCNTs through strong π–π interactions in water [121]. In this study electron transfer between SWCNTs and perylene molecule was investigated, where SWCNTs acts as electron donor and perylene as electron acceptor.

Most representative biocompatible polymer used for solubilization of SWCNTs is DNA and numerous examples of functionalized SWCNTs with DNA have been published [122-125]. Double stranded DNA (dsDNA) has more rigid structure consequently its affinity is to the SWCNT sidewalls is lower, while single-stranded DNA (ssDNA) can efficiently wrap SWCNTS and produce stable dispersions. In fact, SWCNTs treatment by ssDNA and sonication yielded concentrated solution with SWCNTs as much as 25 mg/L [126].

There are numerous studies where polymers are used for dispersion of CNTs in water. It is worth mentioning that the majority of polymers such as poly(styrene sulfate), polyoxyethylene and block copolymers have been demonstrated to wrap the nanotube exposing their polar ends to the aqueous environments while favoring the contact of their hydrophobic domains with the nanotube surface [127, 128].

Rouse group successfully prepared SWCNTs dispersions in alcoholic media by using poly(4-vinylpiridine) having the solution stability greater than 6 weeks [129]. The stability of dispersions was investigated in eight different alcohols including methanol, ethanol, isopropanol and others. The highest SWCNTs concentration was achieved in ethanol and exceeded up to 0.3 mg/mL. Lower solubility in less polar alcohols implies that P4VP have in moderate polarity solvents. Moreover, they demonstrated applicability of the latter dispersion system for fabrication of SWCNT-silica composites. In order to obtain composite materials via sol-gel process the solubility of SWCNTs in alcohols is extremely important.

Chapter 3. Silver Nanostructures: Synthesis, Optical Properties and Applications

The crucial role in plasmonics has metals, because they have free electrons which can interact with propagating electromagnetic waves by creating collective oscillations called surface plasmon polaritons (SPPs) (also called surface plasmons (SP)). In plasmonics, metal nanostructures can convert light into localized electric fields so called nanoantennas or can be used as nanometer precision waveguides. Precise control of nanostructures size and shape allows to effectively manipulate light with high accuracy [130, 131]. Plasmonic materials have high potential in application of many new technologies such as invisibility cloaks, superlenses, quantum computing and photovoltaic devices [132-137].

3.1. Surface plasmon polaritons and localized surface plasmon resonance

Surface plasmon resonance is categorized in two distinct forms: localized surface plasmon resonance (LSPR) and propagating surface plasmon polaritons (SPPs) also called propagating surface plasmons. The LSPR occurs when the dimensions of a metallic nanostructure are less than the wavelength of incident light and generally observed in metal nanoparticles or nanostructured metal surfaces. The SPP modes are attributed to oscillations of free electrons in thin metal film. The LSPR and SPP strongly depends on the refractive index of the surrounding medium, which is the basis of plasmonic sensors [138]. In contrast to SPP, LSPR concentrates the incident electromagnetic (EM) field around the nanostructure. Created EM field can strongly influence optical processes such as fluorescence, Raman scattering and infrared absorption, which reveals new application areas in plasmon-enhanced fluorescence (PEF), surface enhanced Raman scattering (SERS), and surface-enhanced infrared absorption spectroscopy (SEIAS).

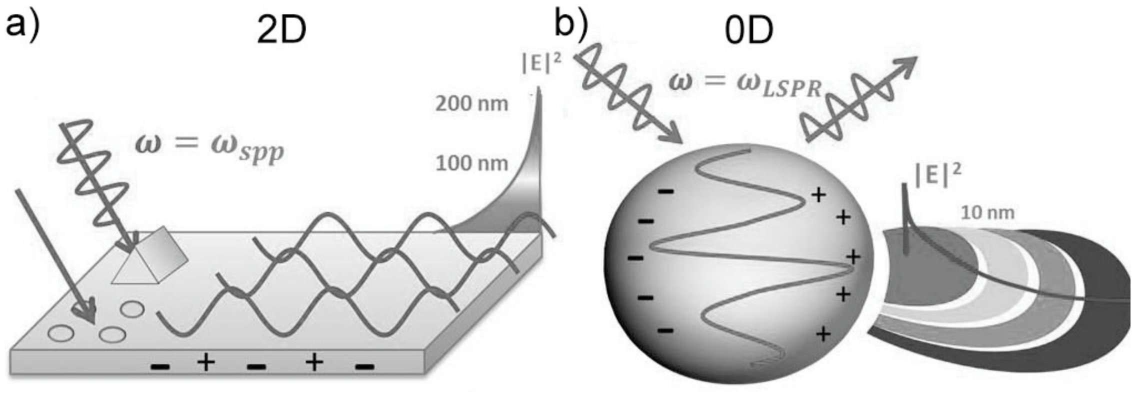

Figure 13. Schematic representation of a) propagating surface plasmons and b) localized surface plasmons [138].

SPP is observed when thin metal film, typically 40 nm gold is illuminated through a glass prism (figure 13). The light is reflected from the film at all angles except for a narrow range of angles where the film absorbs the light. This absorption is associated by resonant electron oscillations induced in the film by the propagating electromagnetic wave. Resonant absorption occurs at the metal surface when the in-plane wave vector (k_X) of the incident light matches the wave vector of the surface plasmons k_{SPP}. The surface plasmon wave vector is determined by the incident free-space wave vector k_0 and the dielectric constants of the metal film (ε_m) and of the sample (ε_s) [139, 140]:

$$k_{SPP} = k_0 \left(\frac{\varepsilon_m \varepsilon_s}{\varepsilon_m + \varepsilon_s} \right)$$

This gives the dispersion curve for the SPP, which shows the wave vector of light necessary to excite a SPP for particular interface. The wave vector of the oscillating charge wave is always greater than that of the massless photon. Therefore, SPP can be only excited in Kretschmann geometry, or by a grating to provide the extra momentum.

The strong influence of dielectric environment on the SPP frequency at the interface gives ability to use plasmonic materials for molecular sensing. The EM field resulting from the electron cloud oscillations is observed in ~100 – 200 nm distance from the surface [141]. The changes of a local environment in this distance will cause a change in a dielectric constant and subsequent shift of the SPP frequency. This results in change of the dispersion curve and SPP excitation the angle, which can be measured experimentally. The narrow absorption line shape and high angular sensitivity of the SPP provides excellent signal-to-noise ratio. However, these SPP based sensors requires complex geometries needed for detection, which decreases its attractiveness [140].

The complex setup required for SPP can be eliminated by using metal nanoparticles. If the nanoparticle dimensions are smaller than the wavelength of light, the electron density will have uniform displacement across the particle surface and strong restoring force from the positive ionic core background. This force causes the specific oscillation frequency in the metal electrons. This phenomenon is known as LSPR. Due to particle geometry provided extra momentum, the LSPR can be excited directly by the incident light [142]. LSPR band position is sensitive to a change in dielectric environment which can be registered by simple UV-Vis spectroscopy. The LSPR peak position depends on the shape and size of particle [143, 144]. The larger and/or higher aspect ratio particles, the smaller the repulsion for electrons at opposite surfaces, and the more red-shifted the plasmon will be [145, 146]. In contrast to incident EM field of SPP LSPR has several orders higher intensity local EM field. In case of nanoparticles with sharp edges such as nanoprisms, the field will be concentrated, which results in increased sensitivity in change of local environment. It is worth mentioning, that the EM field in LSPR decays in ~10 – 30 nm and is therefore more sensitive to changes in close distance but insensitive in a longer distances [147].

In LSPR the plasmons can also re-radiate its energy into the far field as scattering [148]. If size of metal particle is considerably small (less than ~15 nm) the LSPR energy is converted into heat via electron-electron scattering resulting strong absorption. Increased size of the particle reduces electron-electron scattering, therefore in this case LSPR energy will be re-radiated into far field resulting in a strong scattering cross-section (figure 14) [142, 149, 150].

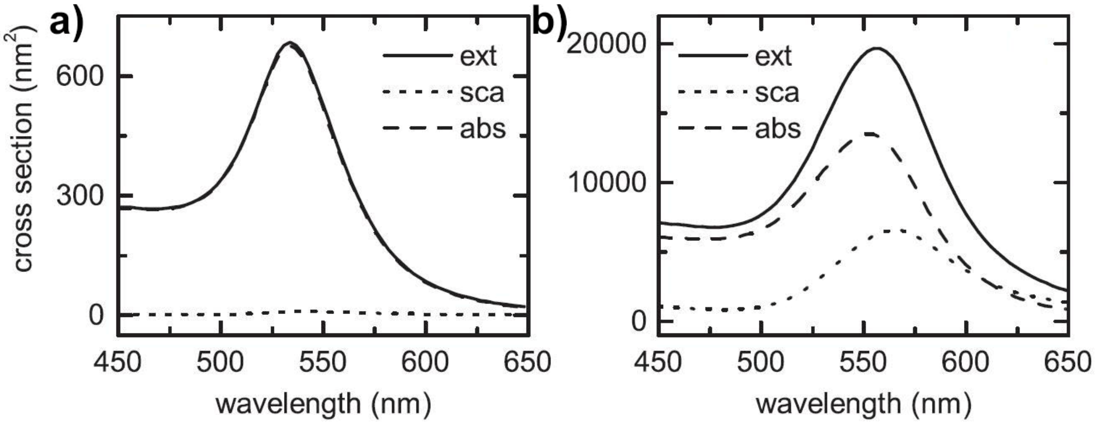

Figure 14. Extinction, scattering and absorption spectra of a metal particle with a radius of a) 10 nm and b) 30 nm. In both cases, the refractive index of the environment is 1.5 [151].

Coupling of local fields is also interesting phenomena, which may occur between two plasmonic nanostructures when they are in distance of EM field decay length [140]. This coupling can highly enhance intensity of local EM field and induce shift in the spectral position due to interference between the modes. For example, the enhancement of local EM field of two spherical particles goes from ~10 to ~10^4 when they are in close distance [140, 142]. Coupling of the LSPR mode can be realized by aggregating several plasmonic structures. However, too close distance between particles in the aggregate may decrease the LSPR, due to damping. Therefore, some particular distance must be maintained between the particles.

The SP strength is directly proportional to quality factor (Q). The larger values of Q mean the stronger plasmons (both LSPs and SPPs). The Q can be described using the formula [152, 153]:

$$Q = \frac{\omega(d\varepsilon_r/d\omega)}{2\varepsilon_i^2}.$$

For majority plasmonic applications Q should be larger than 10. Silver metal has the largest quality factor the spectrum from 300 to 1200 nm (figure 15). Aluminum has high Q factor in UV region, where other metals generally have low values. High Q of gold and copper is only observed above 600 nm. This can be related to interband electronic transitions from valence to conduction band, which damp the SP modes [152, 154]. In case of Ag these transitions take place at much lower wavelengths than the LSPRs.

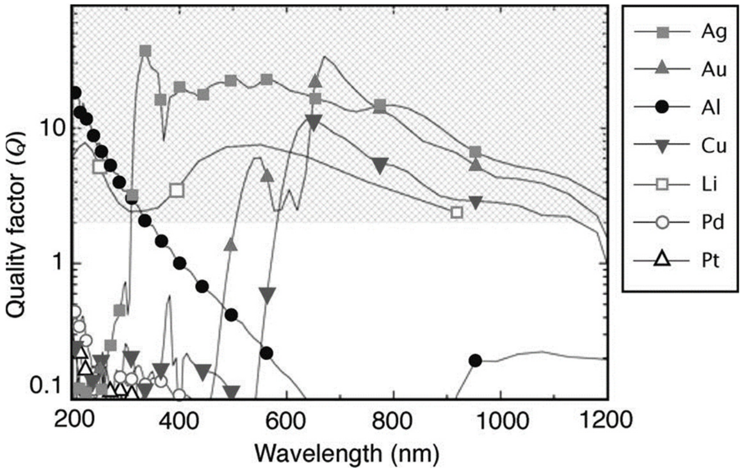

Figure 15. Quality factor (Q) of the LSPR for a metal/air interface. The shaded area represents the region of interest for many plasmonic applications [152].

In practice, other properties must to be taken into account before selecting proper material (figure 15). For example, Li has high Q factor and theoretically may generate high intensity LSPR in broad spectral region. However, lithium is very reactive and therefore is hard to handle such material. Copper nanostructures also are not very stable – they tend to oxidize when exposed to air. Although silver is not oxidized in air atmosphere, but it may form a silver sulfide layer on its surface, which might decrease LSPR intensity and refractive index (RI) sensitivity [155, 156]. In solution exposed Ag nanostructures may release Ag^+ ions which considered being toxic and therefore are less biocompatible than Au. On in other hand, Ag^+ ions toxicity can be taken as an advantage by applying Ag nanostructures for antibacterial or anti-fouling purposes. Nevertheless, Ag nanostructures can be coated by some protective layer decreasing its chemical reactivity and solubility.

Gold nanostructures are generally considered very inert, therefore suitable for *in vivo* applications [157]. In case of Ag nanostructures, they are largely used in plasmonic applications including optical materials, or sensors used outside a living organism, where they have better performance than Au-based nanostructures.

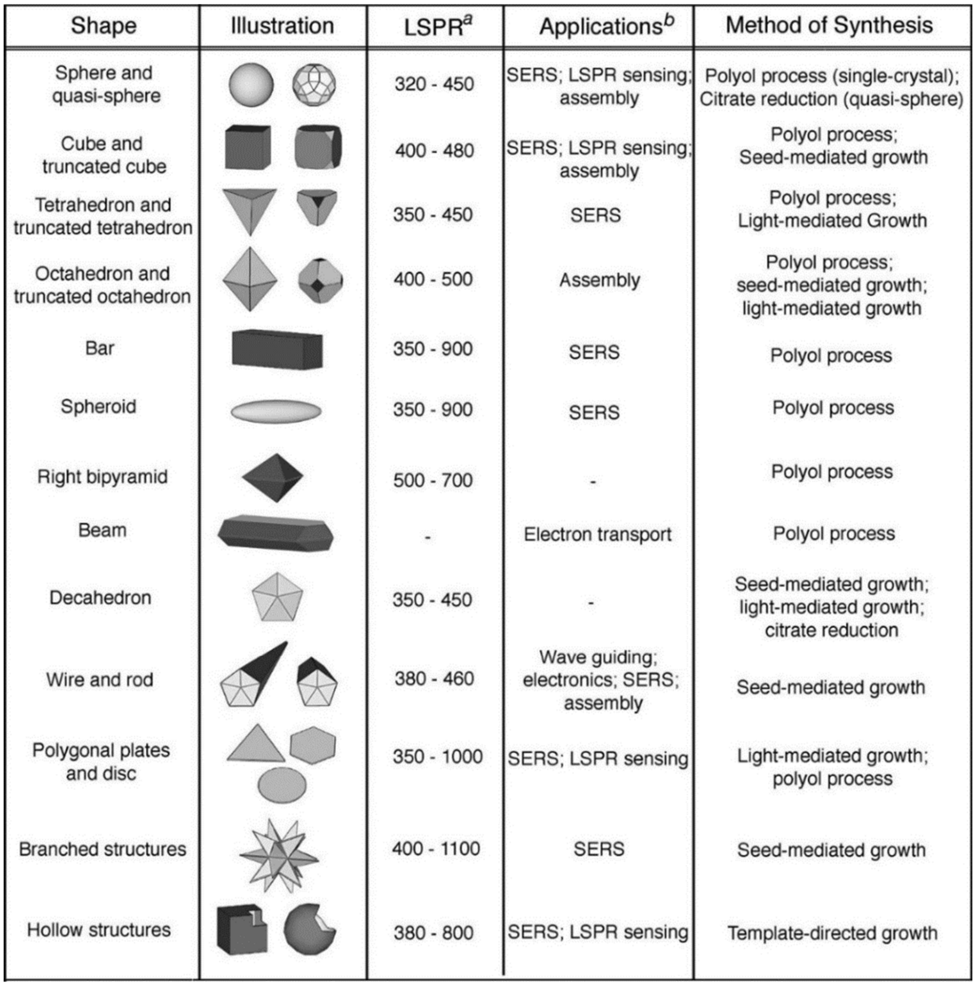

Shape	Illustration	LSPR^a	Applications^b	Method of Synthesis
Sphere and quasi-sphere		320 - 450	SERS; LSPR sensing; assembly	Polyol process (single-crystal); Citrate reduction (quasi-sphere)
Cube and truncated cube		400 - 480	SERS; LSPR sensing; assembly	Polyol process; Seed-mediated growth
Tetrahedron and truncated tetrahedron		350 - 450	SERS	Polyol process; Light-mediated Growth
Octahedron and truncated octahedron		400 - 500	Assembly	Polyol process; seed-mediated growth; light-mediated growth
Bar		350 - 900	SERS	Polyol process
Spheroid		350 - 900	SERS	Polyol process
Right bipyramid		500 - 700	-	Polyol process
Beam		-	Electron transport	Polyol process
Decahedron		350 - 450	-	Seed-mediated growth; light-mediated growth; citrate reduction
Wire and rod		380 - 460	Wave guiding; electronics; SERS; assembly	Seed-mediated growth
Polygonal plates and disc		350 - 1000	SERS; LSPR sensing	Light-mediated growth; polyol process
Branched structures		400 - 1100	SERS	Seed-mediated growth
Hollow structures		380 - 800	SERS; LSPR sensing	Template-directed growth

Figure 16. Summary of the shapes, LSPR absorption peaks, demonstrated applications, and methods for synthesis of Ag nanostructures prepared in solution phase [152].

The size and shape of nanostructures determine their plasmonic properties. At present, many methods are available for generating Ag nanostructures with different sizes and shapes. Figure 16 represents Ag structures, that have been synthesized in the solution phase.

Especially interesting are particles with the triangular-like particle shape, called nanoprisms (NPRs). NPRs can be synthesized in the form of a nanoparticle via solution methods or can be fabricated in the form of nanostructures by nanosphere lithography (NSL) with well-defined mutual distances and orientation. Due to the unique optical properties of the NPRs, such as strong electric field enhancement on the tip, they have already found an application in the SERS and the plasmonic solar cell construction.

3.2. Optical properties of Silver Nanoprisms

3.2.1. Linear optical properties of AgNPRs

As mentioned previously, LSPR intensity and wavelength of silver nanoprism is determined by its dimensions and shape factor. In general, size of the nanoprism is described by edge length and the thickness. The ratio between these two values so-called 'aspect-ratio' is most important factor for the spectral position of LSPR. Contrary to small spherical NPs, anisotropic metal NPs such as nanoprisms exhibit multiple LSPR modes occurring at different wavelengths [158].

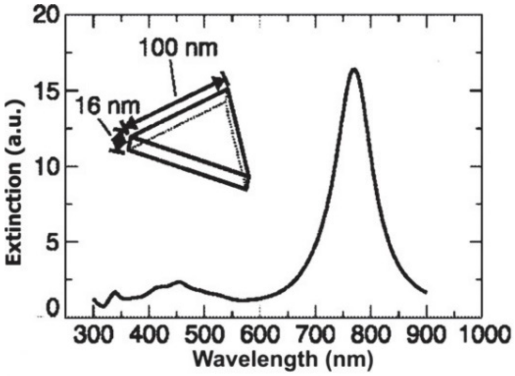

Figure 17. DDA simulations of the orientation averaged extinction efficiency spectra of a perfectly triangular nanoprism [159].

The highest intensity LSPR band is generally assigned to dipole mode resonance occurring at nanoprism tips. Ag nanoprism theoretical calculations by discrete dipole approximation (DDA) method were firstly published by *Schatz et. al.* [159], which were used to identify the plasmon bands measured from nanoprism dispersions. Calculations were based on 100 nm edge-length and 16 nm thickness AgNPR. Together with dipole mode researchers at the first time distinguished two quadrupolar LSPR modes (figure 17). The peak at 770 nm was assigned to the in-plane dipole plasmon resonance, the weaker peak at 470 nm to the in-plane quadrupolar resonance, a small but sharp peak at 340 nm was identified as the out-of-plane quadrupole, and a weak shoulder around 410 nm was assigned to the out-of-plane dipolar resonance though it is barely discernible. The study also revealed that maximum enhancement occurs at the tips for dipole resonance and its generated E-field decays in longer distance than quadrupole mode.

The direct relationship between optical spectra and LSPR modes has been studied by *Nelayah et al*. [160]. The study demonstrated direct mapping of plasmon modes in silver nanoprisms by using high resolution electron energy-loss spectroscopy (EELS). EELS spectra acquired at three discrete areas (tips, edge and center) on an AgNPR (10 nm thick and 78 nm edge-length) showed well-defined in-plane dipole, in-plane quadrupole and out-of-plane quadrupole resonance modes at 1.75, 2.70 and 3.20 eV, respectively. Figure 18 presents EELS amplitude maps of different modes in the triangular particle. Moreover, obtained results show good correlation between theoretical calculations and experimental results.

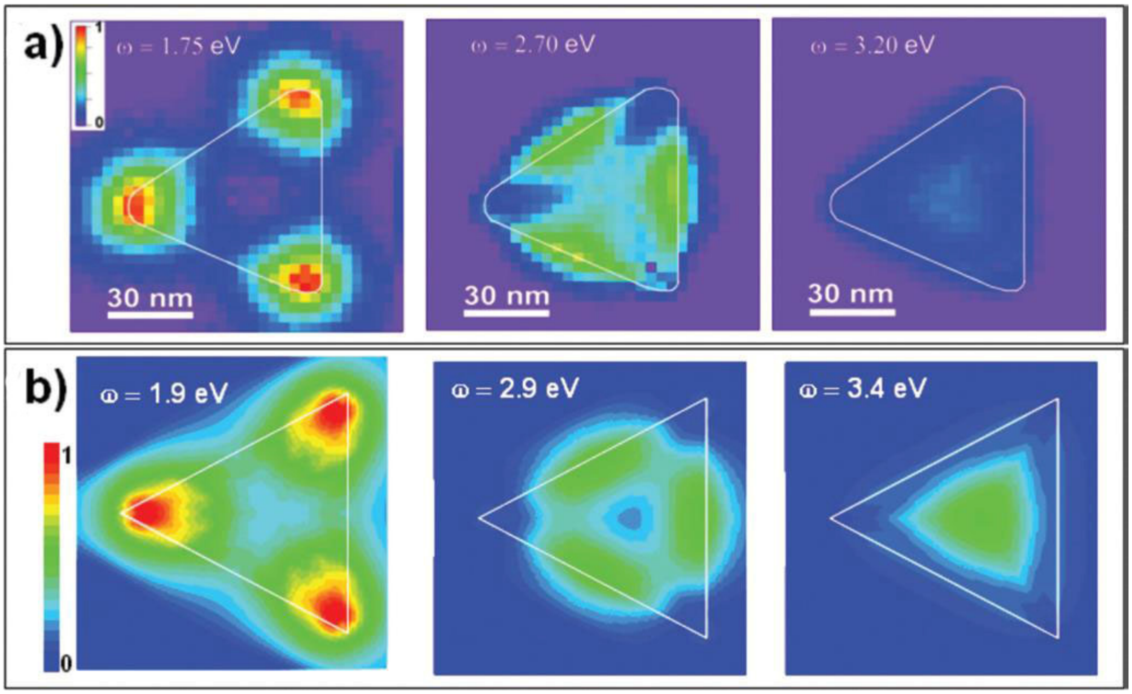

Figure 18. Experimental (a) and simulated (b) EELS amplitude maps for an Ag nanoprism [158, 160].

In other theoretical calculations it was also observed [159, 161, 162] that the peak of both the in-plane dipole and quadrupole modes may also shift in longer wavelengths when nanoprism size increased. However, due to central position of quadrupole mode in nanoprism, this mode is considerably less sensitive to particle size than in-plane dipole mode. In practice, colloidal nanoprisms are often found to be truncated rather than perfect triangular shape. Therefore, the effect of snipping was also studied by using DDA method (figure 19). Obtained results showed great sensitivity of in-plane dipole resonance peak to snipping - the 10 nm snipped prism gives a peak that is blue-shifted by 100 nm as compared to the perfect prism. However, the other modes are more weakly sensitive to snipping[159].

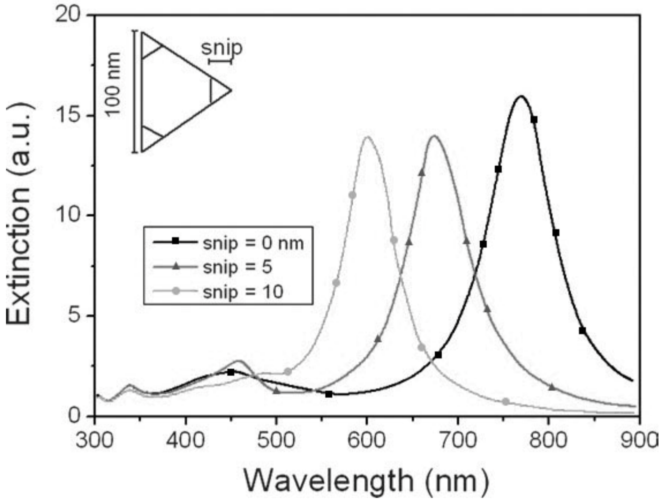

Figure 19. DDA simulations of the extinction efficiency for trigonal prisms based on a 100 nm edge dimension with snips of 0, 10, and 20 nm [159].

As mentioned previously LSPR frequency of plasmonic particle depends on its dielectric environment, or otherwise on the refractive index of the surrounding medium, which is the basis of plasmonic biosensors. The study published by *Pastoriza-Santos et. al.* [163] demonstrated a correlation between LSPR frequency of Ag nanoplates and refractive index of the solvent at different DMF and water ratios. Results showed blue-shift of the in-plane dipolar resonance exceeding 40 nm which is quite strong compared to 5 nm shift for spherical silver nanoparticle [158, 164]. Other study showed 100 nm blue-shift in LSPR frequency when AgNPRs thin film were transferred from water to air atmosphere. *Van Duyne et al. [165]* measured AgNPRs dark-field scattering spectra in four different dielectric environments demonstrating the AgNPRs sensitivity to the surrounding environment.

3.2.2. Nonlinear optical properties of AgNPRs

While the linear optical properties of metal nanoparticles have been extensively investigated, there still lacking knowledge about the application of these materials in nonlinear optics (NLO). Nevertheless, because superior NLO responsivity is largely a matter of attaining superior electronic polarizability and hyperpolarizability, one might expect metal nanoparticles, with their exceptionally high density of delocalized electrons, to be good-candidate NLO materials [166].

The presence of a LSPR enhances the third order susceptibility of metal nanoparticles, which makes metal nanoparticles suitable for NLO materials. The third order nonlinear polarization gives rise to self-focusing, self-phase modulation, soliton propagation, and phase conjugate reflection [167]. The size and shape of the nanoparticles play a crucial role in the surface plasmon absorption band and, hence, the optoelectronic properties of these materials [168, 169]. Several research groups reported the nonlinear optical features of metal nanoparticles [170-172]. The third order nonlinear optical properties depend on sizes and shapes of the particles [173-175].

Ag nanoparticles have the potential to obtain the largest enhancement factors due to the strength of the local field that gives rise to SPR and large third order nonlinearity. The SPR energy of silver is far from the interband transition energy. This facilitates the separate investigation of nonlinear effects arising from interband transitions and those due to the SPR.

Ganeev et al. studied saturable absorption and nonlinear refraction of Ag-doped silicate glass at 352 nm wavelength [176]. It was shown that saturated absorption was dominated at small laser intensities and decreased with the growth of intensity. Another study demonstrated ultrafast nonlinear response time as fast as 200 fs and a third-order nonlinear optical susceptibility of 0.94 x 10^{-10} esu of small Ag nanoparticles embedded in porous silica film [177]. The nonlinear response and the enhanced nonlinearity were attributed to intraband transitions of the free electrons.

Two-photon absorption (TPA) of large (80 nm) silver nanoparticles was also demonstrated when laser wavelength matches AgNP quadrupole mode excitation wavelength [178]. *Qu et al.* investigated saturable absorption and reverse saturable absorption of different shape Ag nanoparticles. Results revealed, that highly branched AgNPs (such as Ag nanoflowers) shows reverse saturable absorption, where silver nanowires exhibited saturable absorption at the lower incident intensity and reverse saturable absorption at the higher incident intensity [179].

Optical limiting effects of AgNPRs was studied by *Polavarapu et al.* Fluence-dependent transmittance measurements using 7 ns laser pulses of 532 nm wavelength showed that the optical limiting properties of plain and gold coated AgNPRs in solution are slightly better than that of carbon nanotube suspensions, which is known as a benchmark optical limiter. The study demonstrated great nonlinear scattering caused by plain. Nonlinear scattering experiments suggested that nonlinear scattering should play an important role in the observed optical limiting effects [180].

3.3 Synthesis methods and growth mechanisms of AgNPRs

To date, a variety of synthesis methods have been developed to prepare prismatic, plate-like nanostructures such as nanoprisms, nanotriangles, nanoplates, or nanodiscs. Au and Ag nanoprisms typically have edge lengths in the ~40nm to 1µm range and thickness ranging from ~5 to 50 nm [181]. However, usually micrometer sized nanoprisms does not distinguish the optical or chemical properties which have their smaller analogs [182-184].

3.3.1. Light-mediated synthesis methods of AgNPRs

The first reproducible and high yielding AgNPR preparation methods was based on photochemical route. The photo-induced method was first suggested by *Jin* and co-workers [185] which relied on the photoconversion of citrate-capped Ag seed particles (spherical nanoparticles, smaller than 10 nm) into large AgNPRs by irradiating Ag-seed solution with visible light in the presence of bis(p-sulfonatophenyl) phenylphosphine dihydrate dipotassium salt (BSPP). The study revealed the importance of the illumination type - when the Ag-seed solution was illuminated by NIR or UV only formation of larger spherical particles took place. In solution stored in the dark no conversion to nanoprisms was observed. The mechanism of the process was also proposed. There was suggested that Ag seeds are firstly converted into small clusters, together with the formation of small nanoprisms, followed by the growth of the AgNPRs at the expense of the small clusters via light-induced Oswald ripening (figure 20). Study also emphasized the importance of BSPP as primary shape-directing agent.

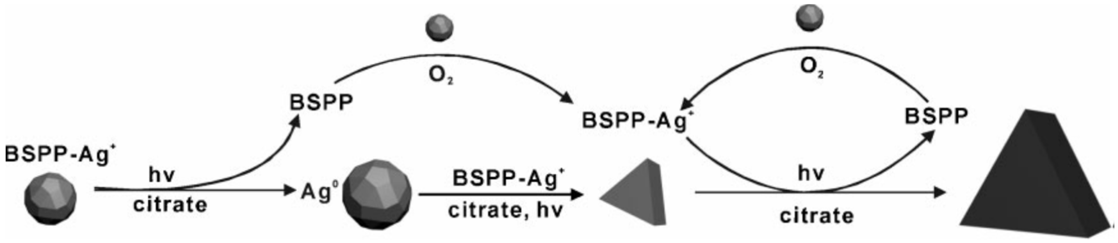

Figure 20. Proposed photo-induced growth pathway of Ag nanoprisms from spherical nanoparticles [181].

However, *Gehlen et al.* [186] displayed a very similar approach where BSPP was replaced by poly (vinylpyrrolidone) (PVP) which also resulted formation of AgNPRs. Other study suggested that while PVP is mainly responsible for the formation of small and well-dispersed Ag seeds and citrate ions acts as shape directing molecule. They claimed that citrate molecule can selectively adsorb to (111) facets of silver surface and subsequently inhibit further growth on the (111) plane and promote growth to 100 facet.

C. A. Mirkin group in their study [187] investigated the role of light in this photochemical conversion process. They used dual-beam excitation for Ag-seeds conversion to AgNPRs. The wavelengths of irradiated light were selected to overlap the dipole (primary beam) and quadrupole SPR (secondary beam) modes of the final Ag nanoprisms. When Ag-seed solution was irradiated only by primary beam it resulted in two different edge length AgNPRs – 70 and 150 nm. In contrast, simultaneous excitation light resulted in smaller AgNPRs only. The results suggest that excitation matching quadrupole mode inhibits the fusion of the smaller AgNPRs. Moreover, by varying wavelength of the primary beam over the visible spectrum (450 – 750 nm), authors obtained nanoprisms with edge lengths ranging from 40 to 120 nm (figure 21).

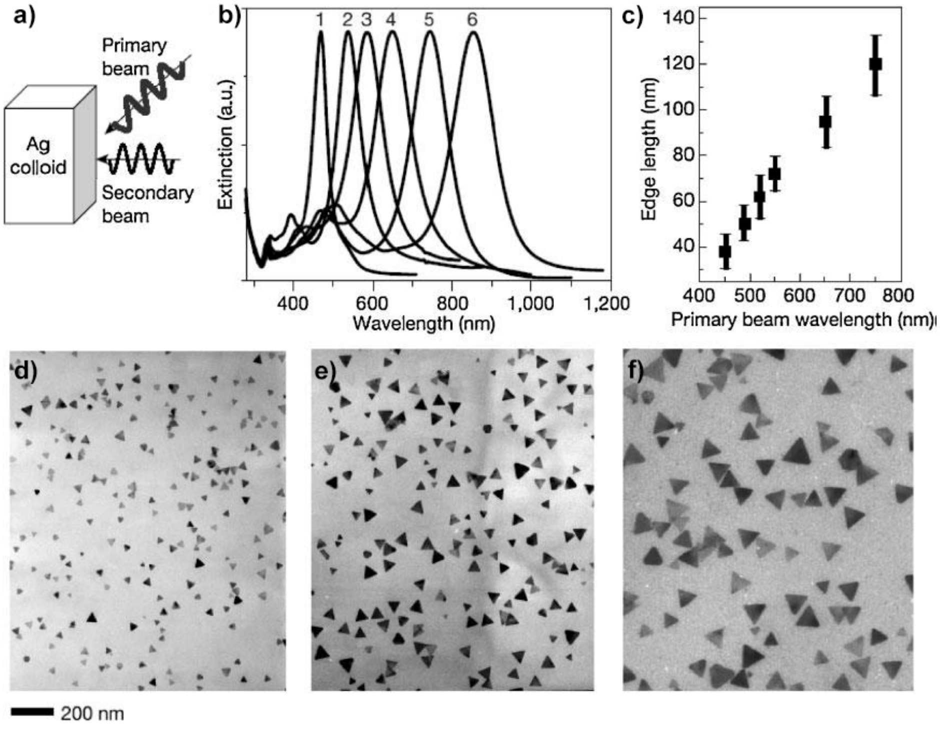

Figure 21. The unimodal growth of nanoprisms using dual-beam excitation: a) schematic diagram of dual-beam excitation, b) the optical spectra (normalized) for six different-sized nanoprisms prepared by varying the primary excitation wavelength and coupled with a secondary wavelength, c) edge length as a function of the primary excitation wavelength, d–f) TEM images of Ag nanoprisms with average edge lengths [187].

In another report by *Bastys et al.* [12] was presented improved photo-induced method based on illumination of the Ag seeds with light emitting diodes (LEDs). They prepared silver nanoprisms having intensity LSPR in the NIR region at telecommunication wavelengths. Particles with having dipole mode LSPR band at 1037 nm or 1491 nm were obtained using LEDs with emission bands centered at 518 nm and 653 nm, respectively. Was observed, that the selected wavelength determines particle size, without noticeable effect on the shape and thickness of the particles. Recently, *Xue et al*. [188] presented improved photo-induced strategy to produce high monodispersity AgNPRs. Contrary to common approach, in place of PVP or BSPP authors were used OH^- ions to improve the monodispersity of silver seeds, as well as to control the growth process through inhibiting the oxidation of silver nanoparticles, by removal of oxygen. Moreover, good particle size control allowed to aggregate particles into six-tip based hotspots which resulted SERS enhancement up to 10^7.

3.3.2. Seed-mediated synthesis methods of AgNPRs

Soon after the first report on photo-induced formation of AgNPRs, other wet-chemistry methods were reported. The study published by *Chen et al.* [189] presented solution phase method for preparation of AgNPRs without illumination. The approach was based on seed-mediated reduction of silver ions on Ag-seeds using ascorbic acid as reducing agent in the presence of cetyltrimethylammonium bromide (CTAB). CTAB adsorbs on the (111) plane of the silver seeds allowing selectively grow to the other crystal planes. Another study demonstrated ability to control of the lateral dimensions of the nanoplates between 40 and 300 nm by adjusting CTAB and Ag-seed concentrations [190]. However, this method results in relatively low yield of nanoplates and a mixture of various other shapes particles. Study published by *Smith and Korgel* demonstrated very interesting results regarding CTAB importance on the colloidal seed-mediated synthesis of gold nanorods. They compared CTAB obtained from different suppliers and results revealed the dramatic differences. With the same recipe, three of the CTABs did not yield any nanorods and produced only spherical gold particles, whereas the other CTABs yielded nanorods with nearly 100% yield. Interestingly, remains unclear whether the impurity in the CTAB either induces or disrupts nanorod formation, because some higher purity CTABs resulted in less yield of nanorods. Indeed, CTAB might contain small amount of iodine, which can also induce formation of anisotropic nanoparticles including AgNPRs [191].

Pastoriza-Santos and Liz-Marzan [163] suggested completely different method to prepare AgNPRs. Authors presented a simple method providing truncated silver nanoprisms by refluxing silver nitrate solution in DMF, in the presence of PVP. There DMF acts as solvent and reducing agent. The proposed mechanism involved the formation of small silver spheres, which would then aggregate and subsequently recrystallize into particles with well-defined edges, through a melting-like process. A continuous variation of nanoprism size during the boiling experiment was observed. However, the latter method results in a mixture of nanoprisms and nanospheroids.

Aherne et al. in their study [192] devised highly reproducible and rapid seed-mediated synthesis of AgNPRs in high yield. Particles were prepared in two stages – preparation of Ag-seed solution and further growth of AgNPRs. The first step involved Ag-seeds formation through the reduction of Ag^+ ions with $NaBH_4$ in presence of poly(sodium styrenesulphonate) (PSSS) and trisodium citrate. In second step AgNPRs were produced by slow addition of $AgNO_3$ in presence of ascorbic acid and particular amount of Ag-seed solution. Study demonstrated, that the key ingredient in production of high quality samples was PSSS. If PSSS is left out or only added to the seed solution after seed production, then there is a diversity of nanoparticle shapes and sizes. The PSSS is not simply playing a shape-directing role through preferential adsorption to certain crystal faces during the growth stage, but rather it must have a strong influence on the defect structure of the seeds and indeed a preference for seeds whose structure predisposes them for growth into nanoprisms.

Moreover, by this method the spectral position of the SPR can be tuned by controlling the size of the nanoprisms, without any significant variation in thickness. This can be achieved through adjustment of the amount of Ag-seed solution in the growth mixture (figure 22). In the proposed mechanism authors claimed that triangular shape and constant thickness of nanoprisms results from highly selective lateral growth from the edges. TEM study showed lamellar defect structure of the nanoprisms, which it is precisely at these edges where the defects are exposed to the growth solution. The hcp crystal faces (or defect-rich regions) at the edges must support a much faster rate for the addition of silver atoms during growth, compared to the (111) or (100) faces which provides two-dimensional growth of AgNPRs.

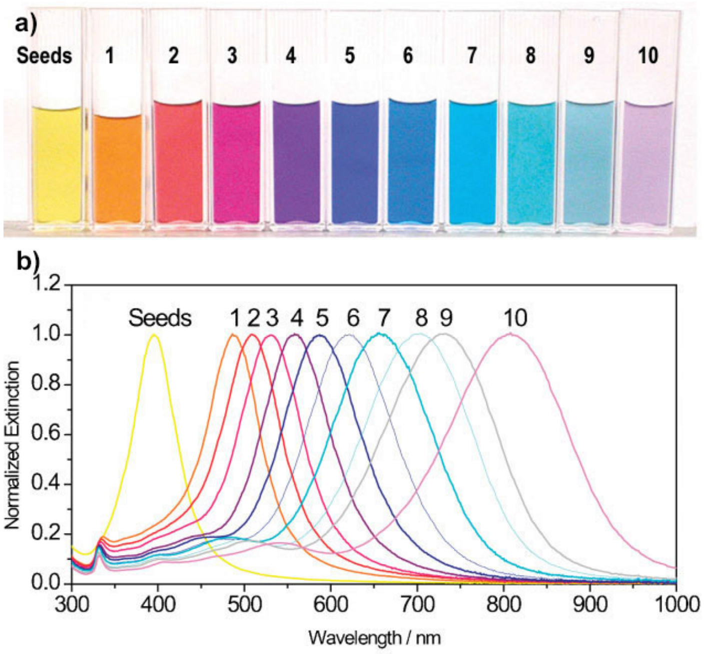

Figure 22. a) Photograph of series of samples illustrating range of colors obtained. The purple color in sample 10 is largely the result of extinction by the in-plane quadrupole. b) Normalized spectra of a series of as-prepared samples obtained using different volumes of seed solution [192].

Based on previous studies other researchers developed flow-through synthesis methods for preparation of AgNPRs [193-195]. *Knauer et al.* [194] presented multistep microcontinuous flow-through synthesis procedure for the generation of homogeneous, high-quality Silver nanoprisms. The particle synthesis is based on previous study where PSSS were used. Because of the fast segment-internal mixing, a clear improvement in the particle quality was achieved. In later study by same group was presented successful particle immobilization into hydrogels [193].

3.4 Application of Ag nanostructures for surface enhanced Raman scattering (SERS)

Raman scattering spectroscopy is a one of the major methods used in determining chemical information of the materials, which can be applied in qualitative and semi-quantitative analysis. The method is based on inelastic scattering of monochromatic light of UV-VIS-NIR range, so called Raman scattering, which was at the first observed by *Raman and Krishnan* in 1928 [196]. However, only small portion of the energy of the incident light is converted to Raman scattering, therefore in to obtain good spectrum it is necessary to have high amount of the analyte. First observations of unusual high intensity spectrum of the pyridine than expected was observed in 1974 when roughened silver electrode were used as substrate [197]. However, the authors attributed latter enhancement to an increase of surface area rather than recognizing a new phenomenon. In 1979 *Moskovits* and co-authors provided theoretical explanation of the enhancement relying on plasmon resonance and adsorbed molecule interactions which was named surface enhanced Raman scattering [198]. This enhancement occurs preferentially in the gaps, cavities, or sharp features of plasmonic materials, which are made by nanostructurization of noble metals (i.e. silver, gold, and copper).

In general, SERS is a technique used to significantly increase the weak signal of analyte resulting in enhancements of up to about $10^8 – 10^{11}$ [199]. At the present, significant number of studies exist related with SERS [200] which includes applications in bio-sensing [201], detection contaminants in food [202], even single molecule detection. However, due to the complications related to surface preparation, measurement technique and limited understanding of the SERS mechanism, the potential of SERS has yet not been fulfilled.

The major problem of the method is that even very small variations in substrate nanostructure can cause significant changes in the SERS performance and reproducibility, therefore preparation of reproducible SERS substrates is the leading topic in this area. The preparation methods of SERS substrates can be grouped in two main categories: top-down approach including lithography-based fabrication [203-205] and bottom-up approach [206, 207], such as plasmonic metal nanoparticle preparation by wet-chemistry methods [208, 209]. The main advantage provided by lithography based techniques is the ability to precisely control the geometric parameters of the nanostructures with high reproducibility. However, the latter approach generally requires sophisticated and expensive setups and is very time-consuming. On the contrary, wet-chemistry methods deliver ability to fabricate nanostructured SERS substrates in lower cost.

One of the approaches, to fabricate SERS substrate by wet-chemistry methods is to aggregate colloidal metal nanoparticles. The aggregation can be realized by adding the analytes to the colloidal solution of metal nanoparticles, which induce nanoparticle aggregation. However, in order to obtain reproducible SERS signal, it is necessary to control the aggregation process. There are many methods to control the aggregation of plasmonic nanoparticles for sensitive and reproducible SERS. Molecules having thiol or amine groups can strongly interact with metal nanoparticle surface. Thus the addition of bi-functional molecules such as dithiols or diamines can successfully aggregate metal nanoparticles.

Theoretical and experimental studies already demonstrated anisotropic metal nanoparticles ability to concentrate high electromagnetic fields at specific locations at their surface [162], thereby forming hot spots. Therefore, anisotropic nanoparticles can provide high SERS enhancement without their aggregation.

Moreover, the plasmon band can be matched with Raman laser excitation wavelength by changing the aspect ratio of the particle [210].

As mentioned previously, silver nanoparticles have highest Q factor among all metals used in plasmonics. Therefore, anisotropic Ag nanoparticles are most promising materials in SERS [211]. Recent study reported high SERS enhancement by using star-shaped nanoparticles (also called nanostars) prepared via chemical reduction of Ag^+ by neutral hydroxylamine, followed by a capping−reduction process induced by citrate. Obtained SERS enhancement factor exceeded ~ 10^5, which is considerably higher compared to spherical nanoparticles [212]. Another study reported by *Vo-Dinh et al.* displayed high SERS enhancement by using bimetallic silver coated gold nanostars [213]. Such particles provided over an order of magnitude of signal enhancement compared to uncoated nanostars.

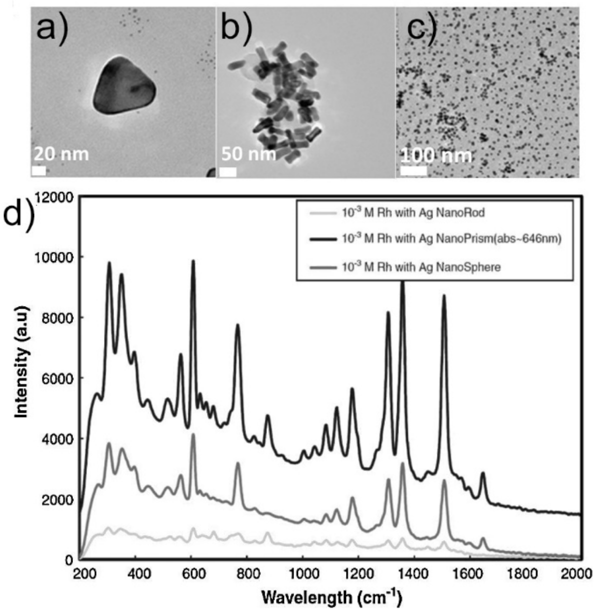

Figure 23. TEM images of a) AgNPRs, b) Ag nanorods, c) Ag nanospheres. SERS spectra of d) rhodamine 6G with various types of AgNPs excited at 785 nm [214].

The silver NPRs are also promising material for SERS enhancement because of formation of high electromagnetic field hot spots at the sharp tips. Despite advantages provided by particle shape, there are no significant amount of studies reported related to AgNPRs application in SERS. Nevertheless, in their study *Tiwari* and co-workers displayed preeminent impact of AgNPRs in SERS enhancement compared to spherical and rod shape AgNPs [214] (figure 23). Another study also reported AgNPRs advantage over spherical particles [215] – the enhancement was 20 times larger for AgNPRs compared to spherical nanoparticles. The AgNPRs impact to SERS enhancement was attributed to better adsorption of the analyte molecule adsorption to nanoparticle surface and matching of LSPR and laser excitation wavelengths.

Fabrication of nanostructured plasmonic surfaces via self-assembly of colloidal metal nanoparticles is one of the major bottom-up approaches. This provides a low cost and time consuming way to create large area SERS substrates having precisely engineered nanoparticles. To date numerous scientific papers have been published relying on the self-assembly of metal nanoparticles on glass surfaces [216-223]. Typically, the glass surface is functionalized with amine or thiol groups using alkoxysilanes, followed by immersion of the functionalized glass into colloidal solution of metal nanoparticles (figure 24). Due to strong interaction between functional groups and metal surface, particles can be successfully immobilized on the surface. The deposition process is controlled by selecting appropriate fabrication parameters such as the type of functional group, immersion time, metal nanoparticle concentration [24].

Figure 24. Assembly strategy for Au and Ag NPs monolayers. X = CN, NH_2, 2-pyridyl, $P(C_6H_5)_2$, or SH; R = CH_3 or CH_2CH_3 [224].

A number of reports has demonstrated a production of the gold and silver nanoparticle monolayers on a glass or agarose films functionalized with 3-aminopropyltriethoxysilane (APTES) or 3-mercaptopropyltriethoxysilane (MPTMS) [216, 222, 223]. Moreover, successful nanoparticle self-assembly was realized to other surfaces such as polydimethylsiloxane (PDMS), or even silver or gold substrates [217-220, 225]. More importantly, this strategy can also be applied to non-flat surfaces such as poly(vinyl alcohol) (PVA) nanofibers [226]. Even though the latter method is well used in deposition of nanoparticle monolayers the deposition mechanism and dynamics are not fully studied so far. *Scarpettini et al.* studied the dynamics of the coverage and aggregation of gold nanoparticles over silanized glass substrates for different sizes of nanoparticles. The presented paper revealed the importance of electrostatic repulsion between particles during assembly process. There was shown that assembled particles are not tightly bounded to substrate and have random mobility across the surface. Indeed, NPs attached electrostatically to the amino groups have mobility and can migrate randomly over the APTES molecules. Initially, the electrostatic repulsion between NPs keeps them away, ending up in a homogeneous and almost equispaced distribution on the surface. However, the hydrophobic nature of gold tends to aggregate the NPs. The occasional collisions between NPs which are continuously moving induce the formation of small aggregates at the beginning and higher order aggregates at a further time [227].

The deposition of AgNPRs on glass surface was also reported in several studies. The earliest experiments reported by *Calderón Moreno* involved direct spin-coating of prepared AgNPRs colloidal solution containing PVP on to glass substrate. However, this way does not provide precise control of particle arrangement, and existing polymer matrix limits application in SERS [228]. Another study published by *Mirkin* group showed successful preparation of high population density AgNPRs monolayers on glass surface via Langmuir-Blodgett method. The latter method requires AgNPRs hydrophobization, which was realized in three steps including AgNPRs functionalization by 16-mercaptohexadecanoic acid (MHA), silanization by tetraethoxysilane (TEOS) via Stöber process and further functionalization octadecyltrimethoxysilane (OTMS). Even though the prepared monolayers are dense and uniform, the multistep process decreases attractiveness of the approach. Moreover, due to large shell thickness it is very unlikely that in such way prepared the prepared particle layers will show some SERS enhancement.

To date, very limited number of studies are reported which rely on AgNPRs self-assembly on functionalized surface. First report was published by the same *Mirkin group* in 2005 [26] where authors prepared large-scale self-assembled AgNPRs monolayers on APTES functionalized glass surface. The study demonstrated high sensitivity to the refractive index of surrounding environment. However, performance in SERS of prepared substrates was not investigated in this study. Another report used the same method to AgNPRs monolayers and studied their performance in SERS [229]. Obtained results showed significantly low SERS enhancement compared to deposited spherical AgNP. Nevertheless, in paper presented TEM images and extinction spectra reveal high particle size and shape deviations, which might be the major reason for low SERS enhancement values.

Chapter 4. Experimental

4.1. Materials

In this work tetramethoxysilane (TMOS, ≥98%, Sigma-Aldrich), tetraethoxysilane (TEOS, 98%, Acros), (3-aminopropyl)triethoxysilane (APTES, 99%, Acros), N-[3-(trimethoxysilyl)propyl] ethylenediamine (AEAPTMS, 98%, Acros), (3-mercaptopropyl)triethoxysilane (MPTMS 99%, Acros) were used as silica precursors and silanizing agents. Aqueous ammonia solution (NH_3, 33%, Carl-Roth), hydrogen chloride (HCl, 33%, Carl-Roth) were used for changing pH of the colloidal silica sol. Sulfuric acid (H_2SO_4, 96%, Chempur), hydrogen peroxide (H_2O_2, 35% Chempur) were used for making the "piranha" solution. Aqueous colloidal solution of unsorted (PureTubes, 99%, 0.25 mg/mL, Nanointegris) and semiconductive SWCNTs (IsoNanoTubes, 99 %, 0.01 mg/ml, NanoIntegris) were used for preparation of SWCNT dispersions. Absolute ethanol (99.9 %) prepared by keeping rectified ethanol on 3Å molecular sieves (30% w/v) overnight and then distilling. Triton X-100 (98 %, Acros), Triton X-305 (98 %, Acros), poly-4-vinylpiridine (P4VP, 99%, 60000 M, Sigma-Aldrich), polyvinylpirrolidone (PVP, 99%, 360000 M, Sigma-Aldrich) were used for solubilization of SWCNTs in ethanol. Silver nitrate ($AgNO_3$, 99%, Sigma-Aldrich), poly(sodium 4-styrenesulfonate) (PSSS, 99%, 1 000 000 Mw, Sigma-Aldrich), sodium borohydride ($NaBH_4$, 99%, Sigma-Aldrich), L-ascorbic acid ($C_6H_8O_6$, 99%, Acros) were used for synthesis of AgNPRs.

BK7 glass substrates (round, 25 x 3 mm, UAB Altechna) were used for preparation of SWCNT, and SWCNT-Silica coatings. Soda Lime glass microscope slides 76 x 26 mm (DG) were used as substrates in all other cases.

4.2. Synthesis and coating preparation methods

4.2.1. Preparation of SWCNTs dispersions in ethanol

Highly diluted SWCNT dispersions in ethanol were prepared by adding 100 μL of aqueous SWCNT dispersion into 10 ml of 1% (v/w) surfactant solution in ethanol, followed by ultrasonic treatment for 15 minutes in ultrasonic bath (Bandelin Sonorex 240W 35kHz).

For preparation of concentrated SWCNT dispersions, freeze-dried SWCNTs were used. 0.25 mg (PureTubes) or 0.01 mg (IsoNanoTubes) of freeze-dried SWCNTs were added into 1 ml of 1% (v/w) surfactant solution in ethanol, followed by ultrasonic treatment for 60 minutes in ultrasonic bath.

4.2.2. Preparation of colloidal silica-SWCNT dispersions

At the first, 3% colloidal silica sol were prepared via Stöber process. Thus, TMOS, NH_3, H_2O and EtOH were mixed by following molar ratio 1:0.2:2.37:38 respectively. Prepared sol was incubated in thermostat at 25 °C for 1 hour. 0.25 mg (PureTubes) or 0.01 mg (IsoNanoTubes) of freeze-dried SWCNTs were added into 1 ml of prepared 3% colloidal silica sol having 1% (w/v) of P4VP followed by ultrasonic treatment for 60 minutes in ultrasonic bath

4.2.3. Base catalysed synthesis of colloidal silica sols

Colloidal silica sols in ethanol were made by base catalyzed TEOS hydrolysis and condensation. For this purpose, TEOS, ammonia, H_2O, and ethanol were mixed with molar ratio 1:0.2:2.3:38 respectively. Sols were left at room temperature for 10 days. Particle size was determined by Dynamic Light Scattering (DLS, Malvern Instruments Zetasizer Nano ZS) method.

4.2.4. Acid catalysed synthesis of colloidal silica sols.

Colloidal silica sols in ethanol were made by acid catalyzed TEOS hydrolysis and condensation. For this purpose, TEOS, HCl, H_2O and ethanol were mixed by molar ratio 1:0.04:4:38 respectively. Sols were left at room temperature for 5 hours.

4.2.5. Acid-base catalysed synthesis of hybrid silica-APTES sols.

Hybrid APTES-silica sols in ethanol were prepared by acid catalyzed TEOS and APTES hydrolysis and condensation. To obtain different amount of amino groups on the coating various TEOS/APTES ratios were used in sol preparation step. For this purpose TEOS, APTES, HCl, and ethanol were mixed at molar ratios a:b:0.04:38, respectively (where a and b indicates different molar fractions of TEOS and APTES). Sols were aged at room temperature for 24 hours.

4.2.6. Preparation of substrates before coating.

All substrates were cleaned by placing them into piranha solution (mixture of concentrated H_2O_2 and H_2SO_4, molar ratio 1:4 respectively) for 15 minutes, followed by washing several times with deionized H_2O and drying in laminar flow cabinet for 24 hours.

4.2.7. Preparation of colloidal silica coatings by dip-coating method.

Before coating procedure sols were filtered through 0.2 µm Nylon filter to remove dusts and agglomerates. Coatings were made by dip-coating technique. All samples were prepared using the constant 40 mm/min withdrawal speed. Coatings were dried for a few hours at room temperature in air atmosphere.

4.2.8. Silanization of silica coatings.

Coatings were silanized by two methods – thermal silanization in dry toluene and in acidic 2-propanol solution.

Silanization in 2-propanol. Prepared silica coatings were immersed in 2-propanol solution of selected silane in presence of 0.1 % acetic acid for 5 h. The modified substrates were rinsed with pure 2-propanol, acetone and deionized water. Silanized coatings were dried 15 minutes in oven, at 120 °C temperature.

Silanization in toluene. Before silanization procedure toluene was dried by keeping under 3Å molecular sieves (10 % v/w) and distilled after. Solution of appropriate concentration of trialkoxysilane (APTES, AEAPTMS or MPTMS) in toluene were prepared. Then silica coatings were immersed in solution and refluxed for 12 h under argon atmosphere. After silanization, substrates were washed several times with pure toluene and acetone. Coatings were dried for 30 minutes at room temperature in air atmosphere. Silanized coatings were characterized by atomic force microscopy, FTIR spectroscopy (Perkin Elmer FTIR Frontier) and contact angle (CA) measurements (KSV Instruments CAM200).

4.2.9. Preparation of hybrid silica-APTES coatings

Hybrid APTES-silica sols in ethanol were prepared by acid catalyzed TEOS and APTES hydrolysis and condensation. In order to obtain different amount of amino groups on coating, various TEOS/APTES ratios were used in sol preparation step. For this purpose TEOS, APTES, HCl, and ethanol were mixed by molar ratio a:b:0.04:38 respectively (a and b indicating different molar fractions of TEOS and APTES). Sols were left at room temperature for 24 hours. Silica coatings without APTES were prepared by mixing TEOS, HCl, H_2O and ethanol in molar ratio 1:0.04:4:38 respectively. In order to remove dusts and agglomerates, prepared sols were filtered through 0.2 μm Nylon membrane filter before coating procedure

Hybrid silica-APTES coatings were prepared by Dip-Coating technique by placing substrate into prepared silica-APTES sol followed by withdrawal in constant 40 mm/min speed. Coatings were dried for 24 h at room temperature in laminar flow cabinet. Prepared coatings were cut to 15x25 mm size rectangles.

4.2.10. Preparation of SWCNT containing coatings by spin-coating

Prior coating procedure, non-solubilized SWCNTs were removed by centrifuging previously prepared SWCNT dispersions at 3000 rpm for 10 minutes.

Coatings were formed by placing 100 μL of SWCNT dispersion onto pre-cleaned substrate followed by spin-coating (SCS SpinCoater P5700) at 2000 rpm for 30 seconds.

4.2.11. Synthesis of silver nanoprisms

AgNPRs were fabricated by the seed-mediated method [192] which includes two steps – producing silver nanoseeds and then growing nanoprisms.

Synthesis of silver seeds. Silver seeds obtained by mixing aqueous trisodium citrate (20 mL, 25 mM), PSSS (1 ml, 0.5 g/L) and freshly prepared $NaBH_4$ (1.2 mL, 10 mM) solutions followed by addition of aqueous $AgNO_3$ (20 mL, 0.5 mM). The addition rate of $AgNO_3$ was 2 mL/min. Addition rate was maintained using syringe pump.

Growing AgNPRs. AgNPRs are produced by mixing 35 ml of distilled water, aqueous ascorbic acid (1.050 mL, 10 mM) solution, silver seeds solution described above, followed by addition of aqueous $AgNO_3$ (21 mL, 0.5 mM) at the rate of 5 mL/min.

4.2.12. AgNPRs self-assembly on silanized silica coatings.

For deposition of AgNPRs, functionalized substrates were immersed in previously prepared AgNPRs colloidal solution and kept for 7 days. The AgNPR-silica coatings were gently washed with distilled water and left to dry in room temperature.

4.2.13. AgNPRs self-assembly on hybrid silica-APTES silica coatings.

For deposition of AgNPRs layers, silica-APTES coatings were placed in plastic containers and 5 ml of AgNPR colloidal solution were added to each container and left to stand at room temperature for specified time. Coatings with deposited AgNPRs layers were gently washed with distilled water and left to dry in air at room temperature. In order to obtain reliable results, each deposition experiment was repeated at least 4 times.

4.3. Characterization of coatings

AFM images were recorded by using Atomic force microscope (Veeco Bioscope 2) in *tapping* mode in 10x10μm magnification and 512x512 pixel resolution. Silica-SWCNT coating thickness were evaluated by scratching the prepared coating and measuring the profile of scratched zone. Coatings micrographs were taken by Optical microscope Leitz Wetzlar 307 combined with Nikon Coolpix 4500 camera.

Water contact angle was measured by KSV Instruments CAM200 optical goniometer. Solution spreading rate measurements were performed by placing a droplet of SWCNTs dispersion onto clean glass substrate and measuring contact angle variation in time. Photographs of the droplets were taken in 33 millisecond intervals and contact angle were calculated by KSV CAM software.

Raman scattering spectra of SWCNTs were recorded with confocal microscope/Raman spectrometer LabRam HR 800 (Horiba JobinYvon Inc.) combined with 632.8 nm excitation laser of 2 μm diameter of the beam at its focal point.

For surface free energy SFE measurements, we selected Harmonic Mean (Wu) method which gives more accurate results when surface have high SFE values. This method utilizes uses a harmonic mean equation to sum the dispersive and polar contributions. Contact angles against two liquids with known values of γ^d and γ^p (dispersive and polar surface tension) are measured. The values for each experiment are put into the following equation:

$$(1+cos\theta)_{y_l} = 4\left(\frac{\gamma_l^d\gamma_s^d}{\gamma_l^d+\gamma_s^d}+\frac{\gamma_l^p\gamma_s^p}{\gamma_l^p+\gamma_s^p}\right)$$

Where γ refers to surface tension (surface free energy), the subscripts *l* and *s* refer to liquid and solid, and the superscripts *d* and *p* refer to dispersive and polar components. Then are two equations with two unknowns and its possible to solve for $\gamma_s{}^d$ and $\gamma_s{}^p$ which are surface dispersive and polar free energies respectively

[230]. In order to calculate surface free energy, in contact angle measurements we used four solvents – diiodomethane, water, glycerol and ethylene glycol.

Hybrid silica-APTES coatings on a silicon substrate were prepared and the layer thickness of was analyzed with rotating analyzer Spectral ellipsometer J.A. Woollam M2000X equipped with Complete EASE software.

CaF_2 monocrystal plate was used as a substrate for registering FT-IR spectra of coatings by using Perkin Elmer Frontier FT-IR spectrometer equipped with ATR module.

Transmittance, absorption and excitation spectra were registered by UV-Vis spectrometer Perkin Elmer Lambda 35.

Various magnification SEM images were obtained by scanning electron microscope (SEM) Hitachi FE-SEM SU-70. For non-conductive samples deacceleration mode was used.

AgNPRs lateral dimensions was determined using SEM. Samples for SEM were prepared by drop-coating of AgNPRs solution onto silicon substrate and drying in air. Average particle size (tip-edge length) was calculated from at least 150 particles. For SEM characterization of self-assembled AgNPRs layers Si was used as substrate.

4.4. Characterization of nonlinear properties

4.4.1 Characterization of saturable absorption of SWCNTs

Saturable absorption experiments on SWCNTs were performed by using femtosecond laser „Pharos“ (UAB "Šviesos konversija") centered at 1030 nm wavelength with 500 kHz pulse repetition rate. At the beginning collimated light beam was transferred through λ/2 plate and polarizing cube *P*. The plate was rotated by polarization of beam output, thus decreasing radiation passing through the cube (in such way is adjusted output power of the laser). Next, laser beam was focused by 10 cm focusing lenses. Specimen was placed at the focal length (obtained 20 μm spot at the confocal parameter) where its position along the beam axis is adjusted by translator. Laser power is measured by two power meters GM1 and GM2 (figure 25). The power of the radiation transmitted through the specimen was adjusted by λ/2 plate and power ratio was measured by power meters.

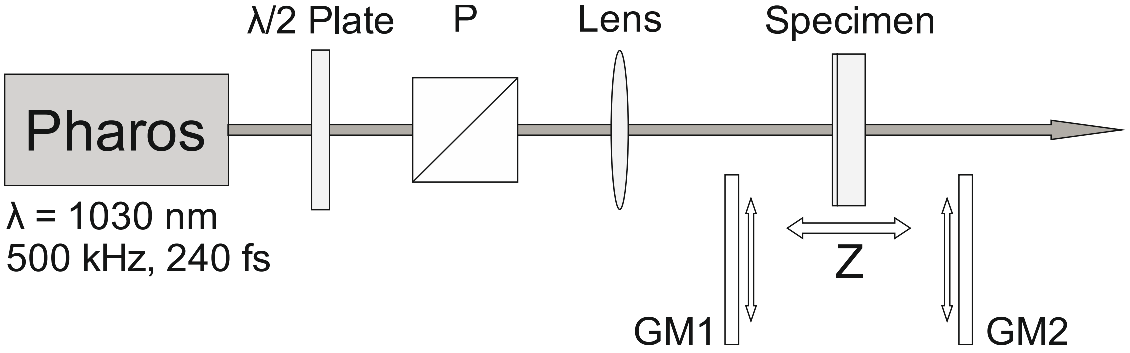

Figure 25. Scheme of the setup for saturable absorption experiments.

4.4.2. Characterization of the nonlinear optical properties of AgNPRs

Nonlinear properties of silver nanoprisms were analyzed by means of femtosecond degenerate Z-scan technique [231, 232] taking into account many considerations proposed in [233]. Measurements were made at several wavelengths in the NIR spectral region. In this technique one measures nonlinear phase front distortion induced in a sample by a focused beam passing through it. Phase front distortion is represented as optical transmittance variation through an aperture placed in transmitted beam path which is a function of the sample distance from the beam waist. All measurements were performed using femtosecond pulses from the optical parametric generator/amplifier (OPG/OPA Light Conversion Ltd., model TOPAS), providing ~100 fs pulses tunable in the wavelengths range from 300 to 2400 nm. Ti:sapphire femtosecond laser ("Vitara" oscillator and "Libra" regenerative amplifier, Coherent) served as a pump source for the OPG/OPA. Pump pulse duration was 98 fs with a bandwidth of 16 nm centered at 798 nm. The repetition rate was set to 1 kHz, which excluded any thermal contribution to the measured nonlinear absorption/refraction signal. So, it was not expected any thermal lensing or other thermal effects in the sample. The used for experiments signal pulse beam from OPG/OPA tunable in the spectral range 1100 – 1580 nm after parametric conversion was spectrally cleaned from idler radiation (1600 – 2600 nm) by a pair of dichroic mirrors and spatially cleaned to follow a Gaussian distribution by focusing into a pinhole. Quality factor of the used femtosecond beam measured after parametric conversion, wavelength separation and spatial cleaning was quite low ($M^2 = 1.25$), which is sufficient to make an assumption, that the beam is ideally Gaussian. Then the beam was recollimated and translated to the experimental area, where it was focused by a 300 mm focal length lens to produce the spot size of approximately $w_0 = 40$ μm at the focal plane. For the pulse energy of $E = 1$ μJ, this results in an on-axis light intensity of up to $I_0 = 330$ GW/cm^2. Liquid samples were contained in the quartz cuvette (SUPRASIL, UVFS from Fisher Scientific). During the measurements, cuvette with the suspension inside was translated along the beam focal region and the whole or diaphragmed transmitted beam far-field intensity pattern was monitored by large area germanium photodetectors. The signal from diaphragmed detector is related with nonlinear refraction whereas the undiaphragmed signal is related with nonlinear absorption. Each sample linear absorption spectra were routinely checked after the irradiation with high intensity (above 10 GW/cm^2) laser field and compared with the spectrum before laser irradiation. This was done to ensure nanoparticle integrity and suspension stability.

Each sample nonlinear refraction was measured using the closed aperture Z-scan method. Normalized transmittance of closed aperture Z-scan for sample was fitted to numerical model, which assumes, that distorted Gaussian beam passed through nonlinear media can be presented as a sum of Gaussian beams with certain related parameters [231, 232, 234, 235]. From the fit model the wave front phase distortion related to nonlinear refraction is derived, which is proportional to nonlinear refraction index:

$$n_2 = \sqrt{2}\frac{\Delta\Psi}{I \cdot k \cdot L_{\mathrm{eff}}}\,[\mathrm{m}^2/\mathrm{W}]$$

where $\Delta\Psi$ is maximal on axis wave front phase distortion on the sample exit plane, I is on axis intensity of electromagnetic wave at focal plane, k – is the wave number and L_{eff} is sample effective thickness.

4.5. Surface enhanced Raman scattering (SERS) measurements

Aqueous uric acid solutions of various concentrations were prepared by diluting a 1 mM stock solution with DI water. 2 ml of 2 % NaOH (Thermo Scientific) solution was added to aid dissolve the uric acid completely. Samples were prepared by immersing the substrates into uric acid solution for 1 h then rinsing with DI water and drying at ambient conditions.

SERS spectra in 4000 – 70 cm^{-1} spectral range were recorded on FT-Raman spectrometer MultiRAM (Bruker Optik GmbH, Ettlingen, Germany) equipped with Nd:YAG (1064 nm) excitation laser of 100 μm diameter of the beam at its focal point. Liquid-nitrogen-cooled Ge diode and Si diode detectors were used to record the SERS signal. Gold plated mirror objective (focal length – 33 mm) was employed. For each spectrum 128 interferograms were acquired and averaged, followed by Fourier transformation. The data was further processed by applying Blackman-Harris 3-Term apodization function and zero filling factor of 2. The spectral resolution of 4 cm^{-1} was used. Laser power was set to 100 mW. Five to seven random spots in every sample were analysed.

Chapter 5. Synthesis of Carbon Nanotube Composite Coatings and Investigation of Their Nonlinear Optical Properties

As mentioned in chapter 1 saturable absorbers are widely used in modern lasers in generating femto-second laser pulses. Due to fast recovery time and low non-saturable loses, SWCNTs are promising material for saturable absorbers in passive mode locking [236]. SWCNT-based saturable absorbers can be fabricated by simple and economical methods, such as spray, spin coating [237] or horizontal evaporation methods [238]. However, application of those techniques requires dissolution of SWCNTs. Unfortunately, SWCNTs are insoluble in any solvents and prone to bundling which decrease the overall yield of usable material and interfere with most of the desired properties of the SWCNTs [79]. SWCNT solubility can be promoted via chemical covalent or non-covalent modification of tube surface. Introduction of surfactants and polymers in a solvent can highly increase the solubility of SWCNT in polar and non-polar media.

First approach to make SWCNT composites as saturable absorbers included application of various polymer matrixes [239]. Unfortunately, polymer matrix tends to degrade at higher energies [239, 240]. Therefore, the introduction SWCNTs into silica matrix can be promising solution in production of high stability saturable absorbers [241]. This chapter describes a study in making SWCNT-silica composite coatings via sol-gel method, investigation their chemical stability and optical nonlinearity.

5.1. Preparation of SWCNTs stable dispersions in ethanol

Stable solution of colloidal silica can be prepared by straightforward and robust Stöber method [242]. However, the latter method requires polar non-aqueous solvents, typically ethanol. In order to obtain homogeneous silica-SWCNT composites, SWCNTs must be introduced in colloidal silica sol. Therefore, the

SWCNTs solubility in ethanol was investigated. All carbon nanostructures, excluding fullerene, are not soluble in any solvents and solubilization of SWCNTs must be performed by using surfactants combined with ultrasonic agitation. Firstly, the solubility of SWCNTs were evaluated at low surfactant concentrations. By this approach, was attempted to eliminate concentration effects and evaluate exclusively a surfactant affinity with SWCNTs surface. Therefore, the final concentration of unsorted SWCNTs exceeded only 0.0025 mg/mL in 1% ethanolic solution of surfactant. Moreover, the low concentration provides the ability to visually monitor the flocculation and aggregation process. Thus, in this experiment for solubilization of SWCNTs different surfactants were used – PVP, P4VP, Triton X-100 and Triton X-305.

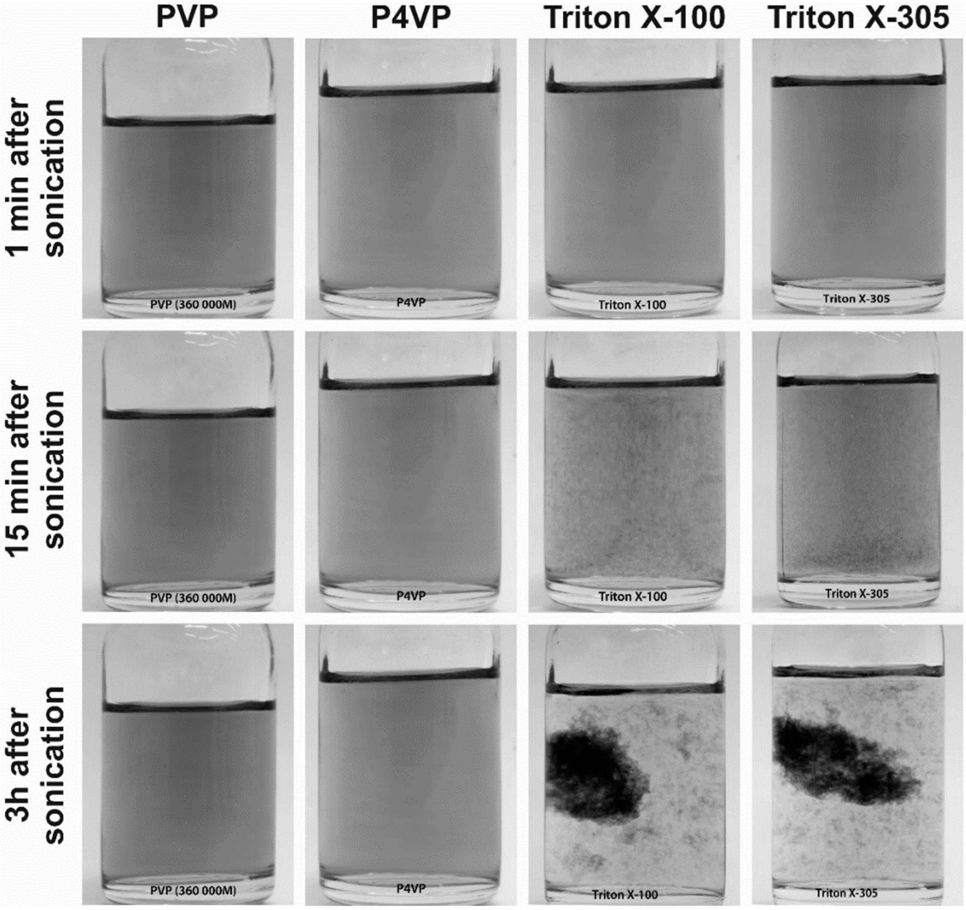

Figure 26. Photographs of prepared SWCNTs dispersions by using various surfactants and after different aging time.

As can be seen from Figure 26, homogenous colloidal solutions were obtained in all cases. Colloids which was stable more than 2 hours were obtained solutions containing PVP and P4VP. SWCNTs flocculation and bundling was observed in solutions containing Triton X-100 and Triton X-305 surfactants 15 min after sonication. This suggests, that all surfactants are able to debundle SWCNTs by disrupting π-π interactions between tubes. However, only nitrogen atom containing molecules show high stability of the prepared dispersions. Indeed, solutions containing P4VP and PVP were stable up to six weeks. The good stability of latter colloids can be explained by existing donor-acceptor interactions between nitrogen atom and sp^2 hybridized carbon in nanotube lattice [243].

PVP and P4VP containing SWCNT dispersions were probed only at low SWCNT concentrations, which is not sufficient to produce desirable SWCNT composite coatings. Therefore, solutions containing PVP and P4VP were evaluated by using higher SWCNT concentrations. In this case, a 1 ml of aqueous unsorted SWCNT solution (0.25 mg/ml) was freeze-dried followed by addition of 1 ml 1% ethanolic solution of PVP or P4VP and sonication for 60 min. At high concentrations typical bundling of SWCNTs results in flocculation, followed by increased viscosity of the colloid rather than dissolution. Therefore, the visual evaluation as performed in previous experiment is not suitable approach in this case. Monitoring the viscosity by common rotational viscometer usually requires a relatively large volume of solution and due to the high cost of materials was decided to evaluate fluctuation in indirect way. At the first, the stability was evaluated by examining the uniformity of the spin-coated SWCNTs thin film after different aging time of a colloid. Prepared thin films were investigated by atomic force microscopy (AFM) (figure 27).

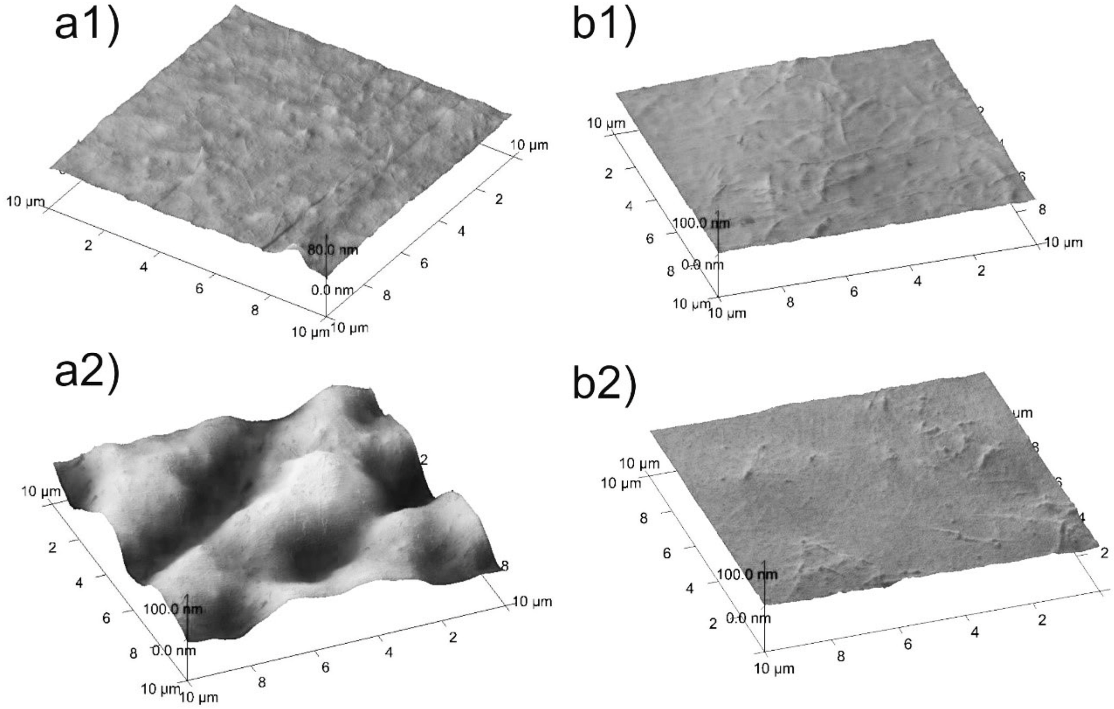

Figure 27. AFM images of prepared SWCNT films with different surfactants and varying the aging time: a1) SWCNT-PVP 1 min after sonication and a2) after 3 days, b1) SWCNT-P4VP 1 min after sonication and b2) after 3 days.

Presented AFM images show, that right after sonication both solutions containing PVP and P4VP forms a uniform film. After aging PVP containing dispersion for 3 days, prepared film is no longer uniform and contains SWCNTs aggregates. Nevertheless, the films prepared from solution containing P4VP were homogenous and uniform in both cases.

It was assumed, that the flocculation of SWCNTs may induce the viscosity of dispersion which will result in the decrement of dispersion spreading rate on the flat surface. Therefore, the flocculation of SWCNT colloidal solutions were investigated by monitoring a spreading rate. This was realized by measuring the droplet contact angle of a SWCNTs dispersion. For this purpose, a 10 µl droplet was placed on the clean glass surface and variation of contact angle in time was measured.

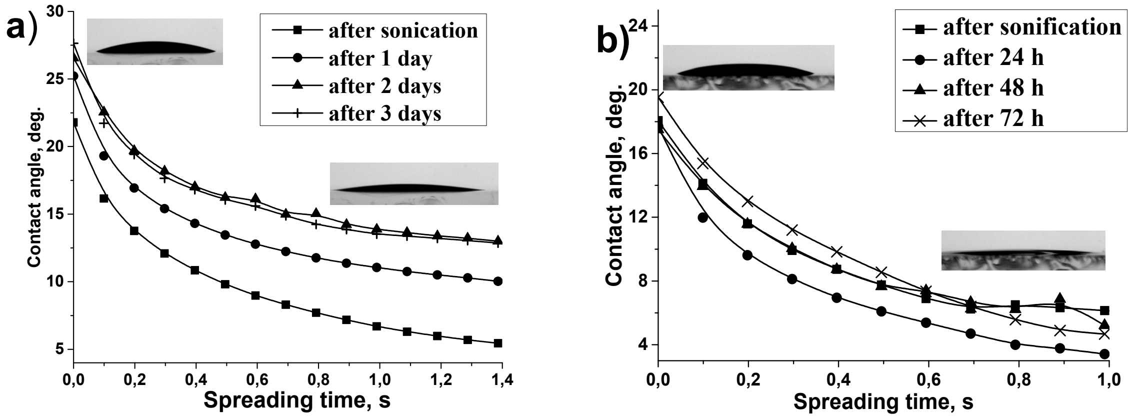

Figure 28. Spreading speed on glass surface dependence on solution aging time of colloidal solutions with different surfactant: a) PVP, b) P4VP.

Obtained data (figure 28) show, that SWCNT-PVP dispersion results in flocculation after 1-day aging – contact angle fully spreads on the surface only right after sonication of the dispersion. After aging for 1 day, the dispersion spreading rate significantly slows down. After two days spreading time stabilizes, but contact angle no longer reaching 5 degrees. Contrary to PVP, a SWCNTs dispersion containing P4VP demonstrates better spreading rate values – the contact angle exceeds 5 degrees in all cases and change in a spreading rate is hardly noticeable. Thus, SWCNT-P4VP solutions may form uniform films right after sonication and after 3-day aging. In addition, the flocculation is significantly lower compared to SWCNT-PVP dispersions. Therefore, P4VP could be a promising polymer for solubilization SWCNTs in ethanol and making silica-SWCNTs composite coatings.

5.2. Saturable absorption of SWCNTs

In this work, we used two types of SWCNTs – unsorted and semiconductive type. Before making SWCNT-silica composites, the nonlinear absorption of different type SWCNT must be evaluated. It is worth to mention, that different type SWCNTs have different solubility – semiconductive SWCNTs are significantly less soluble compared to unsorted SWCNTs. Therefore, colloidal solutions containing 0.25 mg/mL of unsorted SWCNT and 0.01 mg/mL of semiconductive SWCNT were prepared. In both cases, solutions contained 1% of P4VP. Solutions were used for spin-coating on BK7 glass substrates up to 8 layers and saturable absorption experiments were performed.

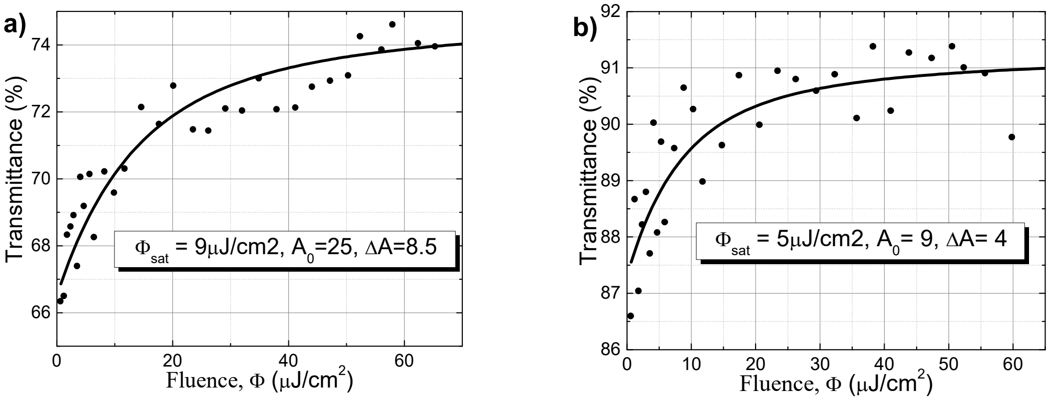

Figure 29. Saturation fluence measurements of different type SWCNT:
a) Unsorted SWCNTs; b) Semiconductive SWCNTs.

In figure 29 presented curves show, that both semiconductive and unsorted SWCNTs exhibit the saturable absorption. Due to small amount of semiconductive SWCNT in a thin film, the absorption of latter SWCNTs is significantly lower compared to unsorted SWCNTs. In another hand, unsorted SWCNTs has higher saturation energy (Φ_{sat}= 9 µJ/cm^2) and higher saturation losses ($A_0 = 25$) compared to semiconductive type (Φ_{sat}= 5 µJ/cm^2, $A_0 = 4$). This reveals, that semiconductive has better nonlinear absorption values than unsorted. On in other hand, due to better solubility of unsorted SWCNTs prepared composite coating has higher SWCNTs content which results in greater saturable absorption (ΔA). Nevertheless, measured saturation energy, and saturation loss values are in in acceptable range for both type SWCNTs to be used as saturable absorbers.

5.3. Thermal stability of SWCNT-silica composite coatings

As mentioned previously, due to reaction with oxygen, SWCNTs are not stable in high-intensity light exposure. Due to the very narrow localized area and fast pulses of laser beam, direct investigation of photo-degradation is difficult to realize and may require complex setup. In fact, direct "burning" of the specimen does not provide much chemical information about degradation processes inside the specimen. Therefore, we assumed that photo-degradation process can be associated mainly with oxidation of SWCNTs, which is similar to thermal oxidation when the specimen is treated at a higher temperature. Due to more precise structure and more definite transition bands, semiconductive SWCNTs were selected in this case. Silica matrix exhibits very good thermal stability, and, therefore, latter media may help to preserve carbon nanotubes structure.

Semiconductive SWCNT-silica composite coatings were prepared via sol-gel process. For this purpose, 0.01 mg/ml of semiconductive SWCNT and 0.1 mg/ml of P4VP were added in ethanol and suspended by ultrasonic agitation for 30 min, followed by introduction of TMOS and NH_3 in a prepared SWCNT dispersion. The solution was aged for 1 hour and then spin-coated on pre-cleaned BK7 glass substrate. Semiconductive SWCNT-P4VP coatings without silica were made for comparison. Samples were heated at 200, 300, 400, 450 °C and Raman spectra were recorded (figure 30).

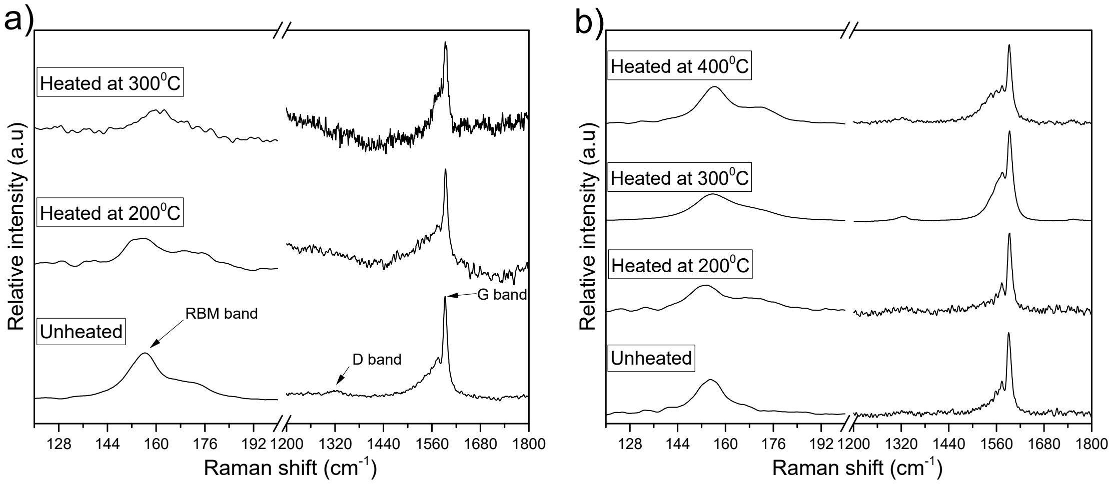

Figure 30. Raman scattering spectra of semiconductive a) SWCNT-P4VP and b) SWCNT-silica films heated in different temperatures.

Obtained Raman spectra clearly show that SWCNT-P4VP coatings start to degrade already at 200 ^{0}C – Raman signal intensity considerably decreased. In addition, the shape of RBM band was significantly deformed and reduced after thermal treatment at 200 ^{0}C. This suggests, that relatively low thermal treatment may damage the tubular structure of SWCNT. In case of the G band observed in latter sample, deformation of latter peak shape is also visible. In addition, no characteristic SWCNT peaks were detected in sample heated at 400 ^{0}C, which suggests that SWCNTs completely degraded.

In the case of SWCNT-silica composite coatings, the heat treatment at 200 ^{0}C, does not deform RBM or G bands. The slight deformations of latter peaks and increment of D band were observed only on samples heated above 300 ^{0}C. However, no distinctive SWCNT peaks were detected in sample heated at 450 ^{0}C, which indicates a complete degradation of SWCNTs. This suggests, that amorphous silica matrix, may isolate carbon nanotubes from an oxygen containing environment and thereby prevent oxidation of SWCNTs. Obtained results show, that integration of SWCNTs into silica matrix has a positive impact to the thermal stability of SWCNTs – thermal stability of SWCNT-silica composite has been increased.

5.4. Production of thicker SWCNT-silica composite coatings

In this part it was attempted to produce silica composite coatings containing a different type of SWCNTs. As mentioned in previous section, SWCNTs, specially semiconductive type, have low solubility, therefore due to natural rigid bonds of silica and strong capillary forces, spin-coating of thick film usually results in micro-cracks in a coating, which limit total layer thickness approximately to 200 nm. Therefore, in order to obtain thicker coating and avoid micro-cracking, coatings were made in layer-by-layer approach.

The colloidal silica sol was prepared via base hydrolysis of TMOS in ethanol. After 1-hour aging, an adequate amount of P4VP were added to get a 1% solution. 0.01 mg/ml of freeze-dried semiconductive type SWCNTs of and 0.25 mg/ml unsorted SWCNTs were introduced into prepared silica sol, followed by ultrasonic agitation. However, some precipitation of unsorted SWCNTs were noticed 10 minutes after sonication. It suggests, that colloidal silica interacts with P4VP and/or SWCNT and thereby decreases the solubility of SWCNTs. Consequently, after sonication, the solution containing unsorted SWCNTs was centrifuged for 10 min at 4000 rpm in order to remove unsolubilized SWCNTs. Prepared colloidal silica-SWCNT sols were spin-coated at 1000 rpm, coating procedure and characteristics of prepared coatings are presented in Table 1.

Table 1 *Characteristics of SWCNT-silica coatings*

Sample no.	**Composition of solution**	**Number of layers**	**Average coating thickness, nm**
JPCM50	3% silica sol, 1% P4VP, 0.01 mg/ml semiconductive SWCNT	1	132 ± 15
JPCM51		2	366 ± 23
JPCM52		3	533 ± 31
JPCM53	3% silica sol, 1% P4VP, ~0.25 mg/ml unsorted SWCNT	1	130- ± 16
JPCM54		2	285- ± 19
JPCM55		3	485- ± 29
JPCM56		5	611 ± 41

Data presented in Table 1 show, that total coating thickness increases with a number of spin-coated layers. In the case of semiconductive SWCNTs, a maximum number of layers was reached at third layer - the fourth layer of coating contained visually observed cracks and aggregates. However, with the use of unsorted SWCNTs solution was possible to obtain up to 5 layers. Thus, obtained visually uniform coatings were up to ~500 nm thickness with both type SWCNTs.

Micrographs of obtained coatings (figure 31) reveal non-uniformities of prepared coatings. Semiconducting SWCNTs containing coatings have minor surface defects already after the second layer and after third layer cracks and aggregates were observed over the large surface area. In the case of unsorted SWCNTs, minor surface cracking was noticed in the third layer and high number of cracks were observed after the fourth layer. Apparently, latter cracking might be induced by increased internal tension in thicker colloidal silica coatings and/or aggregation of SWCNTs.

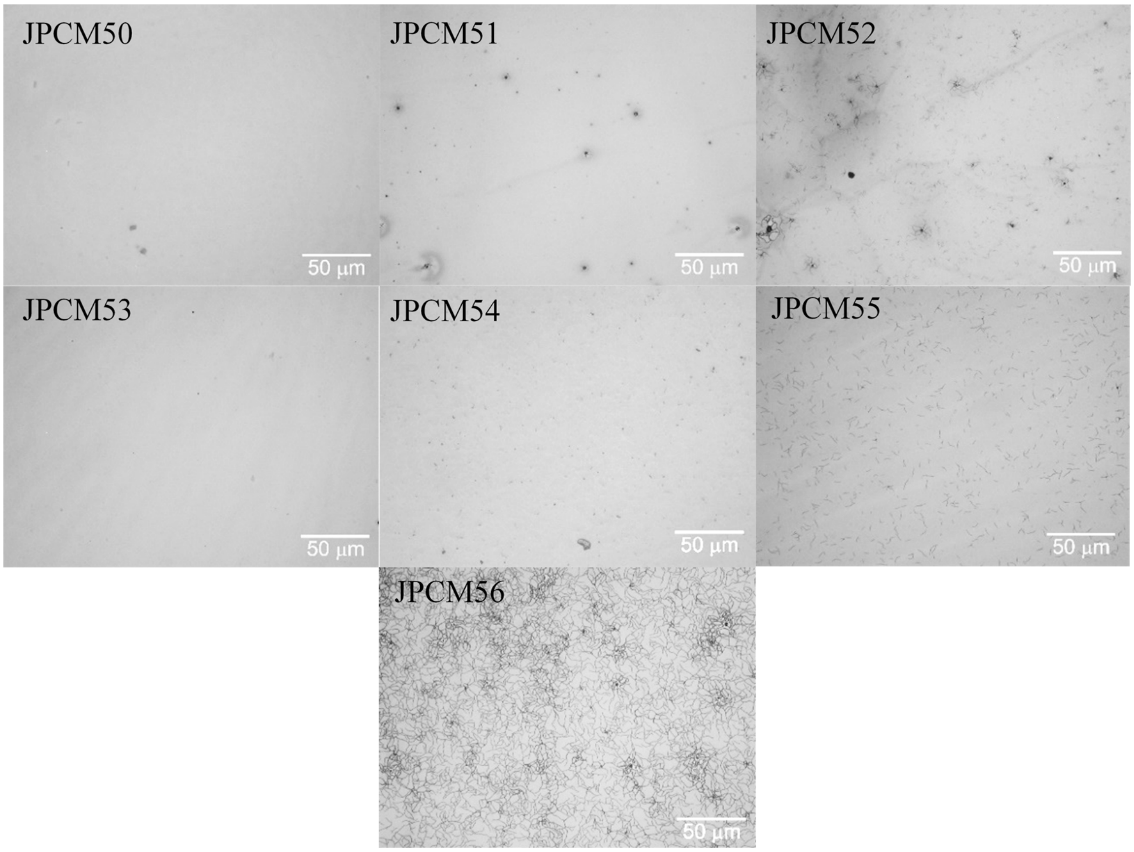

Figure 31. Optical micrographs of prepared SWCNT-silica composite coatings.

In order to investigate coatings morphology for all prepared coatings AFM images were registered (figure 32). The surface morphology of different thickness coatings is similar. However, no SWCNTs were observed in all samples. This can be related with low concentration of SWCNT and/or “masking” of SWCNT pattern by silica matrix. It is worth mentioning, that no SWCNT aggregates are visible in obtained AFM images. Therefore, can be concluded, that coating cracking is influenced only by silica internal tension effects.

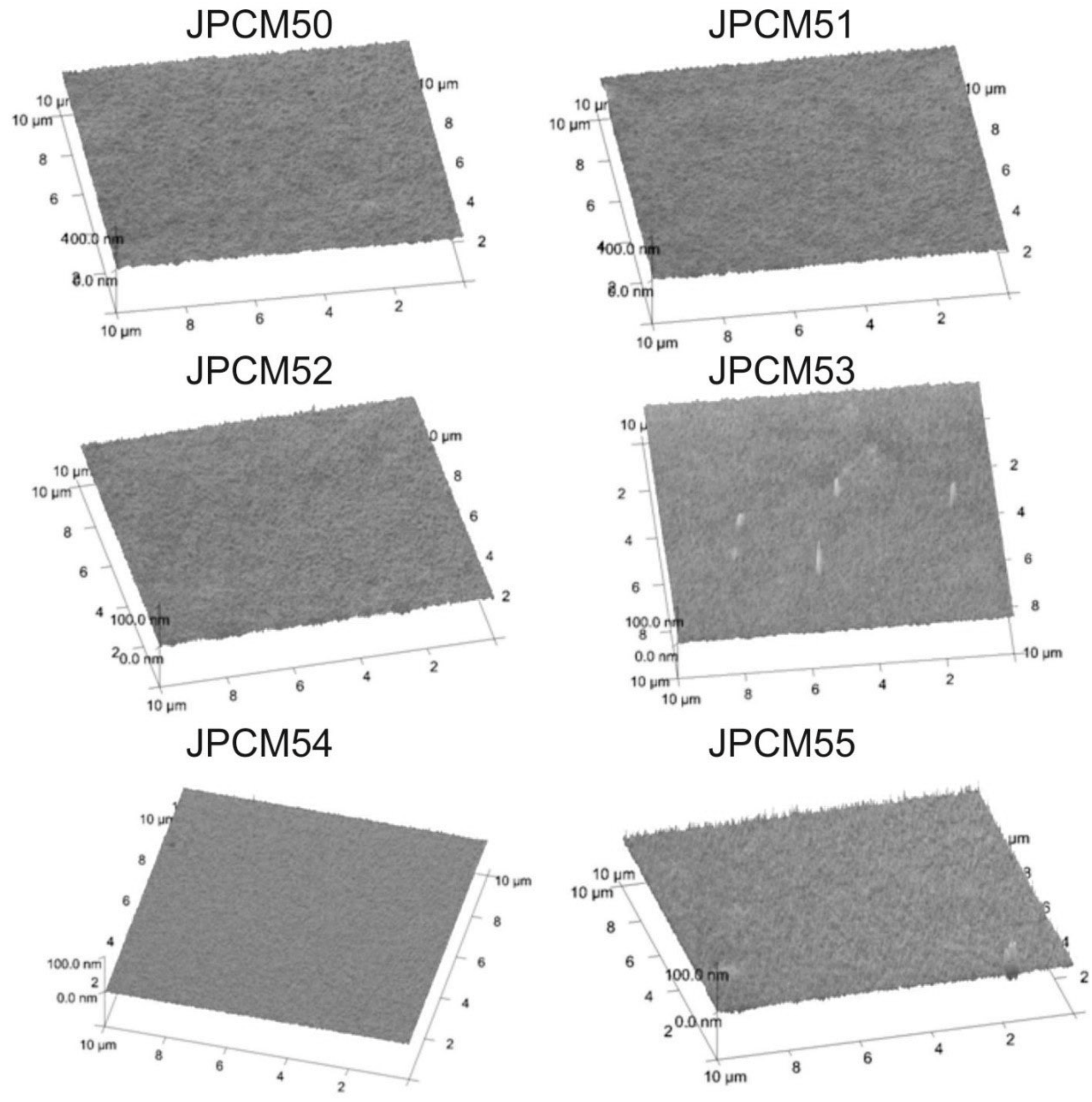

Figure 32. AFM images of prepared various thickness SWCNT-silica coatings.

Measured UV-VIS spectra (figure 33) clearly shows interference pattern caused by low refractive index of porous silica coating. This interference decreasing the amount of reflected light, thus increasing total transmitted light. This could be an advantage when such composite is integrated in a laser device – it will decrease amount of reflected light thus increase device efficiency. However, the interference hinders the absorption of SWCNTs. Therefore, evaluation of nanotubes concentration in the composite coatings becomes more complicated. Nevertheless, decrement of transmittance is visible with increased thickness of the coating.

However, this can be associated with both, absorption caused by SWCNTs and light scattering effects.

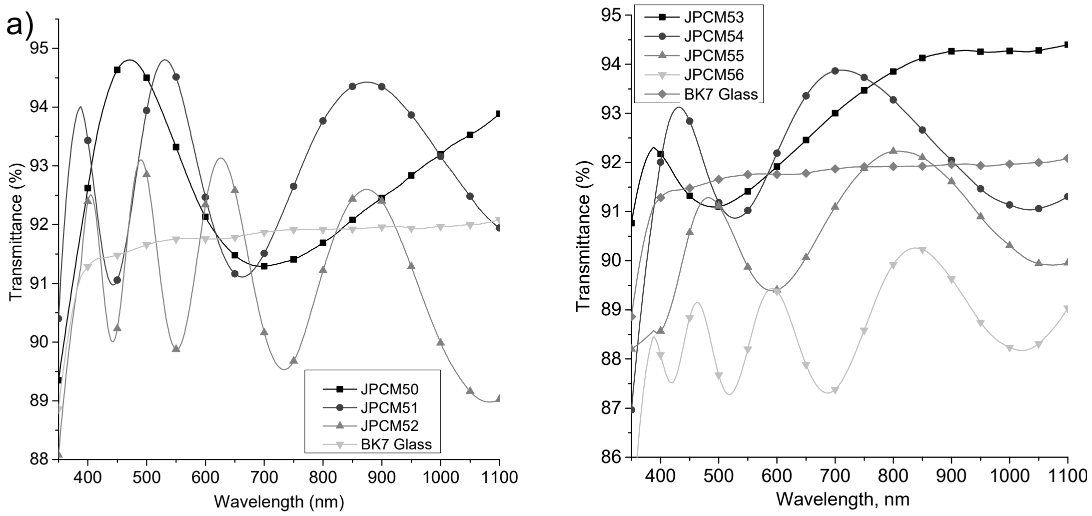

Figure 33. Transmittance spectra of prepared multiple layer SWCNT-silica coatings containing a) semiconductive and b) unsorted SWCNTs

Poor solubility of SWCNT in colloidal silica sol complicates the production of composite coating containing sufficient amount of SWCNTs. Obtained uniform coatings which composed only of 2 or 3 layers had a too small amount of SWCNTs. In addition, prepared composite coatings having good uniformity are relatively thin. Thus, the prepared SWCNT-silica composite coatings had insufficient absorbance for investigation of their nonlinear properties.

5.5. Summary of the results

It was shown, the nitrogen atom containing polymers including P4VP and PVP can successfully solubilize and produce stable dispersions at low SWCNT concentrations (0.0025 mg/mL). At higher SWCNT concentrations (0.25 mg/mL), dispersions containing P4VP as solubilizing agent showed good stability up to 6 weeks, while in PVP containing dispersions noticeable flocculation was observed after 72 hours. The saturable absorption experiment revealed, that semiconductive SWCNTs have lower non-saturable losses and saturation energy compared to unsorted SWCNTs. Thermal stability experiments showed, that SWCNT-silica composite coatings have higher thermal stability compared to SWCNT-P4VP coatings. This suggests, that silica might be ideal matrix in fabricating SWCNT-based saturable absorber. However, the introduction of colloidal silica decreases the solubility of SWCNTs even more. Up to 5 layers containing SWCNT-silica coatings with final thickness of ~600 nm were prepared by layer-by-layer deposition. Microscopically uniform coatings obtained only up to ~300 nm of final coating thickness. However, SWCNT-silica coatings had too small amount of SWCNTs for conducting saturable absorption experiments.

Chapter 6. Synthesis of Silver nanoprisms via Seed Mediated Method and Investigation of Their Nonlinear Optical Properties

Our previous experiments presented in chapter 5 showed, that semiconductive SWCNTs can be good saturable absorbers and silica matrix have a positive impact to thermal stability of SWCNTs. However, the study revealed SWCNTs poor solubility in ethanol. Moreover, the SWCNT solubility in even lower when they combined with colloidal silica. Therefore, obtained results encouraged us to search other materials which might show good nonlinear optical properties and have better chemical compatibility with various media including inorganic silica matrix. One of the promising materials is plasmonic noble metal nanostructures, such as colloidal silver nanoparticles, which can have considerably high intensity localized surface plasmon resonance (LSPR) in 400 – 1100 nm range.

As in the previous study, we focused on the materials, which may show a nonlinear optical response in NIR spectral region. Anisotropic, high aspect ratio AgNPs, like nanoplates and nanoprisms, have LSPR in the NIR range, which can be tuned by varying particle lateral dimensions. Therefore, this study is focused on silver nanoprisms, which LSPR can occur in 600 – 1100 nm range. This chapter summarizes synthesis aspects of AgNPRs via seed-mediated method and influence of the particle shape and size to their optical properties.

6.1. Synthesis of AgNPRs by seed-mediated method

As mentioned in chapter 2, today exist many synthesis ways for preparation of AgNPRs. Due to method simplicity and ability to control AgNPRs size, seed-mediated method was selected, which was firstly suggested by *Athene et al. [192]*. This method allows to synthesize different size AgNPRs by simply varying Ag seeds amount in initial synthesis step. However, on our first trials to synthesis of AgNPRs by seed-mediated method we encountered some difficulties in reproducibility of synthesis. Repeating the synthesis several times in same conditions resulted in a variation of LSPR position in 100 nm interval. The LSPR peak position, intensity and shape are very sensitive to plasmonic particle size and shape factor – i.e. 5 nm deviation of a tip length of 100 nm edge length AgNPR may yield shift of LSPR band up to 80 nm. Therefore, the variation of LSPR in our case represents irreproducibility of AgNPRs size and shape factors. The strict control of synthesis temperature and atmospheric conditions resulted in only minor impact on reproducibility. Therefore, investigation of other synthesis parameters, such as seeds aging time, the timing of added materials were performed in a first place. At the first, we assumed that condition of Ag-seeds solution can be primary factor inducing variations in the final product. In fact, one of the final particle shape determining factors in seed-mediated synthesis method is twinned crystal defects in seed particles. Thus, if the seed particle has different defects and size in the initial seed solution, it will result in a different particle size and/or shape. Indeed, as-prepared Ag-seed solution distinguishes their bright yellow color and as was later noticed, the color of this solution is changing in time – it becomes brownish in a week, and green after a month. This implies, that initial seed solution is not very stable and could be the main reason of variation of the final product. Therefore, we investigated the influence of aging time of Ag-seed solution to the LSPR position of AgNPRs. Ag-seed solution was prepared by $AgNO_3$ reduction with $NaBH_4$ in a presence of PSSS and sodium citrate. Slow addition of $AgNO_3$, ensured gradual reduction and uniform Ag-seed growth process. Prepared Ag-seed solution was spectrophotometrically monitored for 7 days (figure 34).

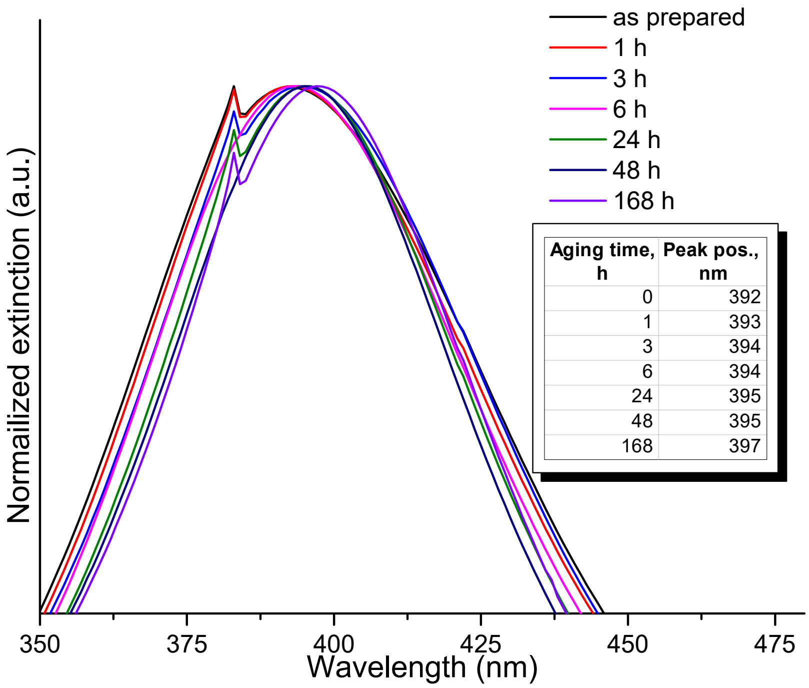

Aging time, h	Peak pos., nm
0	392
1	393
3	394
6	394
24	395
48	395
168	397

Figure 34. Extinction spectra of prepared Ag-seed solution.

Obtained extinction spectra of aged Ag-seed solution clearly show a slight red-shift of LSPR band, which suggests, that further growth of Ag nanoparticles persists after stopping $AgNO_3$ addition. It should be noted, that an excess of $NaBH_4$ was used in Ag-seed preparation step, so it is possible, that some part of unreacted $NaBH_4$ was remained. $NaBH_4$ acts as reducing agent and may have also stabilizing effect for AgNPs. However, Ag-seed solution has to be incubated for a particular period, in order to avoid interference between $NaBH_4$ and ascorbic acid, which is used as reducing agent in AgNPRs growth step.

Different size AgNPRs were synthesized by using Ag-seed solution incubated for different time periods. All other parameters, such as temperature, stirring speed, $AgNO_3$ addition speed was kept the same in all experiments. Large AgNPRs were synthesized by adding a small amount (200 μl) of Ag-seed solution into a mixture of deionized water and ascorbic acid and followed by gradual addition of $AgNO_3$. The ascorbic acid acts as a mild reducing agent, which ensures uniform growth of AgNPRs. The prepared AgNPRs solution was stabilized by addition of sodium citrate solution. For prepared AgNPRs solutions extinction spectra and SEM images were registered (figure 35).

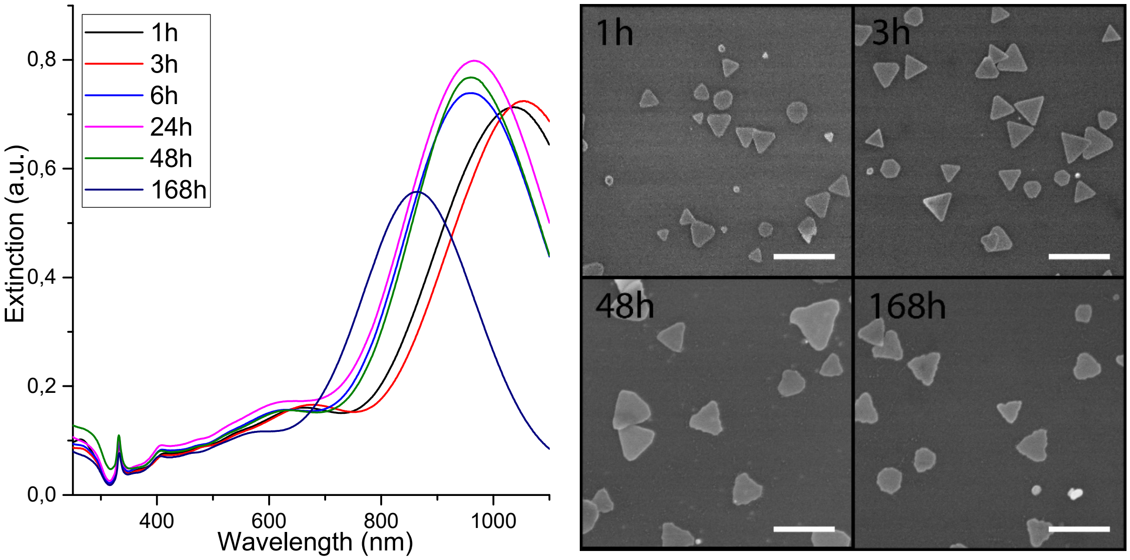

Figure 35. Extinction spectra (left) and SEM images (right, scale bar 200nm) of AgNPRs prepared by using (200 µl) Ag-seeds aged in different time period.

Presented spectra show that AgNPRs synthesized right after Ag-seed preparation has dipole LSPR band at 1040 nm, while 3-hour aging of Ag-seed solution results in an only slight deviation in 30 nm region. AgNPRs prepared with more than 6 hours aged Ag-seed solution spectra shows obvious blue-shift of LSPR dipole band. Nevertheless, the position of LSPR dipole band remains stable on AgNPRs prepared with 6-48 h aged Ag-seed solution. However, aging of Ag-seed solution for 7 days, results in strong blue-shift and decrement in the intensity of AgNPRs LSPR band. SEM images reveal, that aging of Ag-seed affects not only size but also the shape of the particle. AgNPRs synthesized in few hours after preparation of Ag-seeds, distinguish symmetric shape sharp tips and in the case of aged Ag-seeds, AgNPRs edges are less uniform and particle less symmetric. In addition, 7-day aging of Ag-seeds resulted in more polydisperse AgNPRs. Results show, that aging of Ag-seed solution may induce size and shape deviations and subsequent LSPR dipole mode band shift.

As mentioned previously, aging of Ag-seeds induces the red-shift of their LSPR band. Due to the small size of the seed particle, this red-shift more likely will be induced by their growth in size, rather than a change in shape. Moreover, no additional Ag^+ ions were introduced in the solution during aging process. This suggests, that Ag-seed growth works through Ostwald ripening mechanism, where larger particles grow in the expense of small particles. In the case of large AgNPRs, only very small amount of Ag-seeds solution is introduced in the reaction mixture. This implies, that observed size and shape deviations can be also associated with seed concentration change. Therefore, this experiment was repeated by using higher amounts of Ag-seed (560 µl) solution.

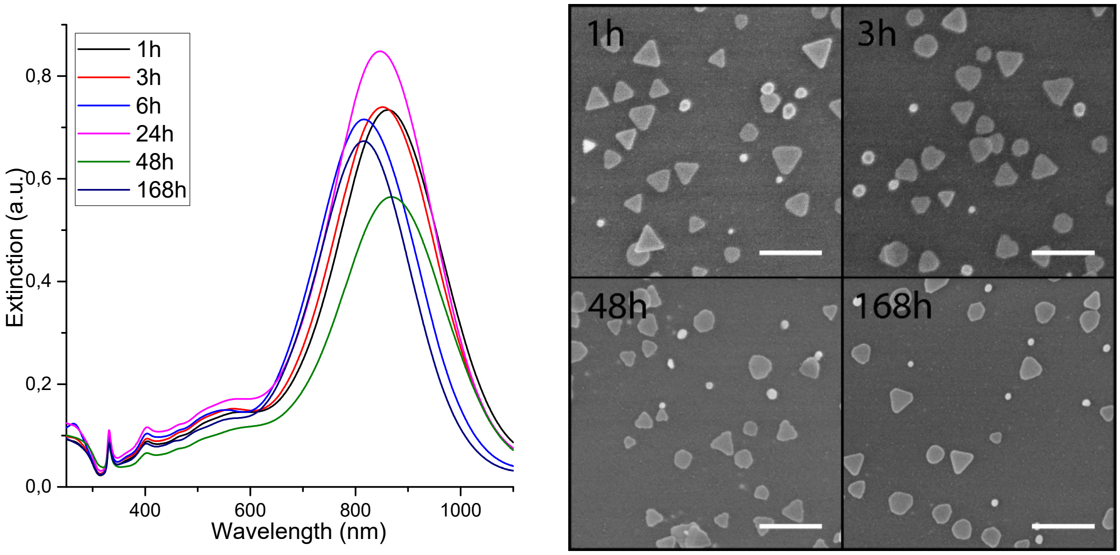

Figure 36. Extinction spectra (left) and SEM images (right, scale bar 200nm) of AgNPRs prepared by using (560 µl) Ag-seeds aged in different time period.

Obtained extinction spectra (figure 36) shows, that in this case LSPR bands are distributed narrower. However, the variations in LSPR intensity of prepared AgNPRs solutions are still evident. LSPR bands of AgNPRs produced with 1-hour and 3-hour aged Ag-seeds have almost the same position and intensity. AgNPRs produced with 6 – 168 hours aged Ag-seeds show no correlation in position or intensities of LSPR – some are blue-shifted while others red-shifted. SEM images show, that obtained AgNPRs have less uniform shape compared to results from previous experiment. Therefore, the evaluation of the influence of Ag-seed aging time to final particle shape and size is more complicated, and observed only slight variations in size and shape. However, longer time aged Ag-seeds produce more round shape particles. In order to have more reliable results, this experiment was repeated on even higher amount of Ag-seeds (2.24 ml).

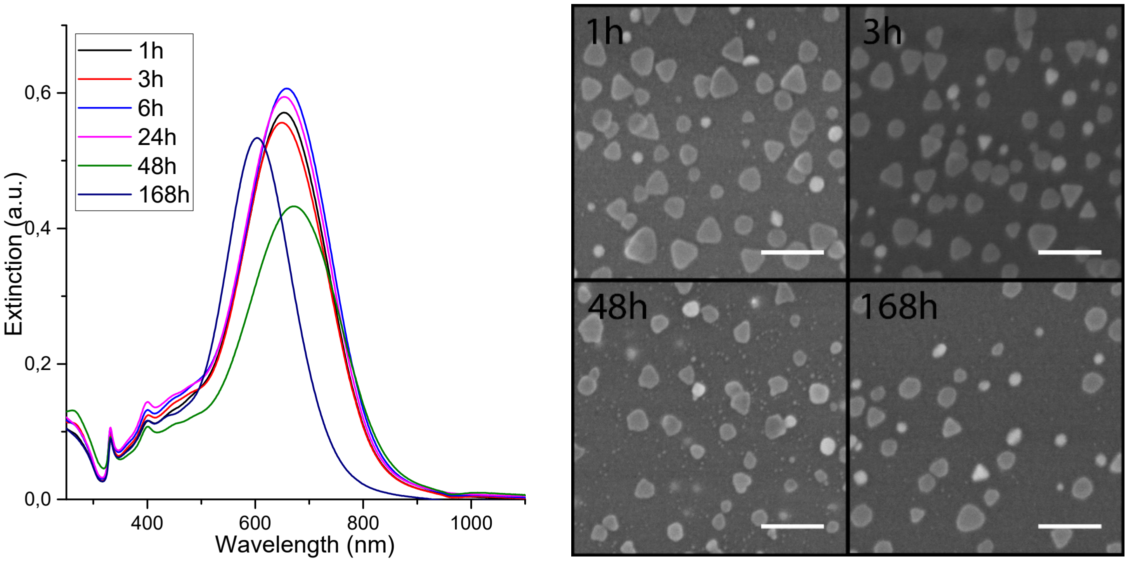

Figure 37. Extinction spectra (left) and SEM images (right, scale bar 100 nm) of AgNPRs prepared by using (2.24 ml) Ag-seeds aged in different period.

In this case, LSPR dipole mode of particle shifts are observed only on AgNPRs produced with more than 48h aged Ag-seeds (figure 37). However, as in previous experiment, LSPR shifts do not show any correlations. SEM images of prepared AgNPRs show only slight deviations in particle size and more distinct deviations in particle shape. AgNPRs produced with 24 – 168 hours aged Ag-seeds appear in more round, disc-like shape rather than prism.

These experiments show that Ag-seed aging time has an apparent impact to AgNPRs size and shape. Moreover, larger AgNPRs showed higher sensitivity to the Ag-seed aging time, than smaller particles. However, particle “rounding” was observed in all experiments. This suggests, that aging of Ag-seed solution leads to less uniform seed particle, which results in more polydisperse and irregular shape AgNPRs. In another hand, significant size and shape deviations were observed only after 3 – 6 hours aging. Therefore, this leads to the conclusion that in order to obtain more monodisperse and defined shape particles aging must not exceed 3 hours.

Optimized synthesis conditions allowed us to prepare stable colloidal AgNPRs. Different tip-edge length particles were obtained by adding a different amount of Ag-seed solution.

Table 2. *Characteristics of prepared AgNPRs*

Sample name	Vol. of Ag-seed solution, µl	Avg. particle size (tip-edge distance), nm	LSPR dipole mode band, nm	FWHM of dipole mode plasmon band, a.u.
Ag-seed	-	6-8*	394	29
S1	4480	~20*	516	83
S2	2240	30 ±7	570	101
S3	1120	38 ±9	636	117
S4	560	49 ±13	717	149
S5	280	90 ±23	820	204
S6	140	149 ±37	1052	-
S7	70	280 ±64	1040	-

* Data obtained from a reference [192]

The main parameters of prepared colloidal AgNPRs are presented in Table 2: volume of Ag-seed solution used, the average particle size (tip-edge distance), position and FWHM of dipole mode LSPR band. The size of the particles and standard deviations from SEM micrographs by measuring at least 150 particles were calculated. As can be seen, synthesized particles vary from 20 nm to 280 nm in size, depending on the used amount of Ag-seed. LSPR bands of prepared particles vary from 516 to 1040 nm. The position of these peaks is sensitive to particle geometrical dimensions, such as the AgNPR tip-edge length and height, metal anisotropy and the dielectric constant of metal as well as surrounding media. It should be noted, that due to very small size of the particles on S1 and Ag-seed sample, was not possible to measure particle size by SEM. Nevertheless, obtained particle size and LSPR band position agrees well with the results published by *Aherne D.* and co-workers [192].

Spectra of obtained AgNPRs (figure 38) and calculated FWHM show, that LSPR band of dipole mode broadens when particle size increases. However, due to the limitation of the spectrophotometer, we were unable to calculate FWHM of the last S6 and S7 samples. The absorption peak width is determined by dispersion of particle, geometrical dimensions as well as by nanoparticle tip sharpness. When a particle becomes large enough, its LSPR band eventually is eliminated by scattering effects. Extinction spectrum of sample S7 perfectly represents this effect. However, weak LSPR resonance is still visible in latter sample.

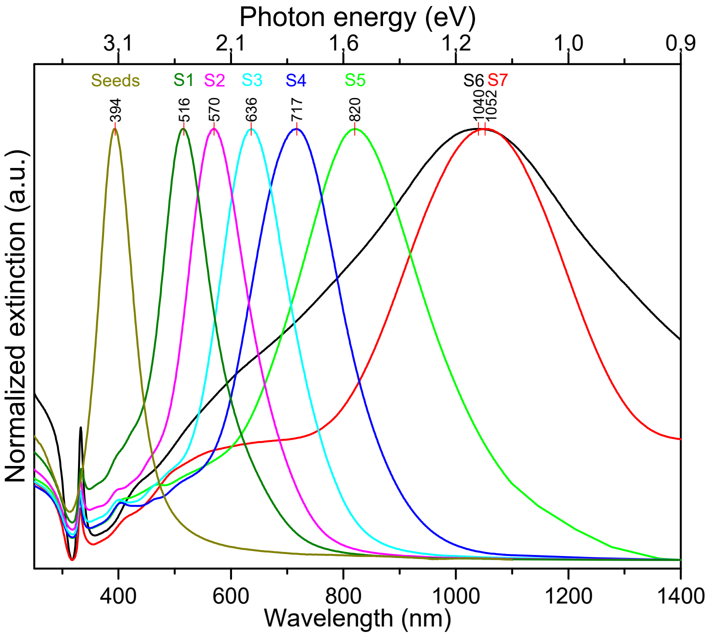

Figure 38. Extinction spectra of prepared AgNPRs solutions

More detailed extinction spectra analysis also shows the existence of much weaker in-plane quadrupole resonances visible as the shoulder of the main resonance (peak wavelength of 423 and 395 nm for sample S1, 453 and 423 nm for sample S2, 489 and 458 nm for sample S3, 509 and 463 nm for sample S4). They arise due to phase retardation effects in the collective surface electron oscillations in light–matter interaction in response to the electrical field. The shortest wavelength resonance at 334 nm is invariant for all samples, which indicates the out-of-plane quadrupole resonance. The absorption appearing below 320 nm indicates the onset of interband transition for silver crystal lattice. The spectral positions of LSPR band positions were not changing over the time (several measurements during a week), which confirmed the stability of the suspensions.

6.2. Investigation of nonlinear optical properties of AgNPRs

This part describes an exploration of different size AgNPRs nonlinear properties by degenerate Z-scan technique [232, 244] taking into account many considerations proposed in [233]. The experiments of nonlinear transmission are displayed in figure 39. The open circles indicate experimental data and the solid line is a theoretical fit of the above-mentioned model. Was observed, that the AgNPRs with LSPR bands in NIR region (S6 and S7 samples) under 1200 nm excitation experienced the significant increase in optical transmission at high excitation intensity compared to low-intensity excitation, where the optical transmission was lower.

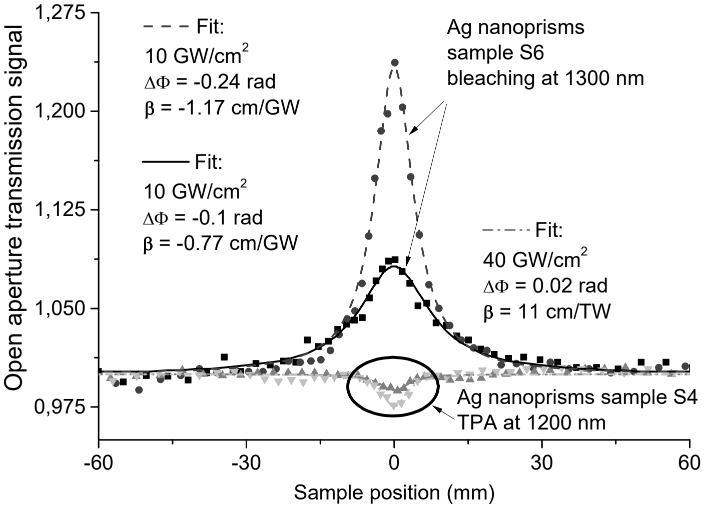

Figure 39. Experimental normalized open aperture transmission data (dots) and theoretical fits (lines) of AgNP sample S4 and S6 at different beam intensities showing negative and positive nonlinear absorption respectively. Beam characteristics: pulse duration 98 fs, wavelength 1200 nm and 1300 nm, beam width at focal plane 41 and 54 µm at 1/e^2.

The open aperture (OA) transmission shows a peak, symmetric around the beam focus position, where the laser pulse has the largest on-axis fluence. The peak results in the negative nonlinear absorption coefficient β, which can be associated with saturated absorption (SA). This can be induced by ground-state-bleaching and interband transitions in silver nanoparticles. Similar OA transmission behavior was already observed in other studies of another plasmonic particles [245-247]. Silver nanoparticles in sample S6 had the nonlinear absorption coefficient of -0.3 cm/GW at 1200 nm and this value decreased more than twice (-0.88 cm/GW) when the excitation wavelength was switched to the telecommunication wavelength of 1300 nm. The water absorption peak at 1450 nm did not allowed to properly evaluate the nonlinear absorption of AgNPRs at longer wavelength (1400–1600 nm) as the weak beam depletion assumption was no longer valid at these experimental conditions. However, the order of measured nonlinearities is consistent with the results obtained by *Wang et. al.* [248] (β from 0 to -3.2 cm/ GW), although they used different wavelength (735 nm), pulse width (2.5 ps), repetition rate (76 MHz) and aimed to study the nonlinear optical response near the SPR peak of silver nanoplates.

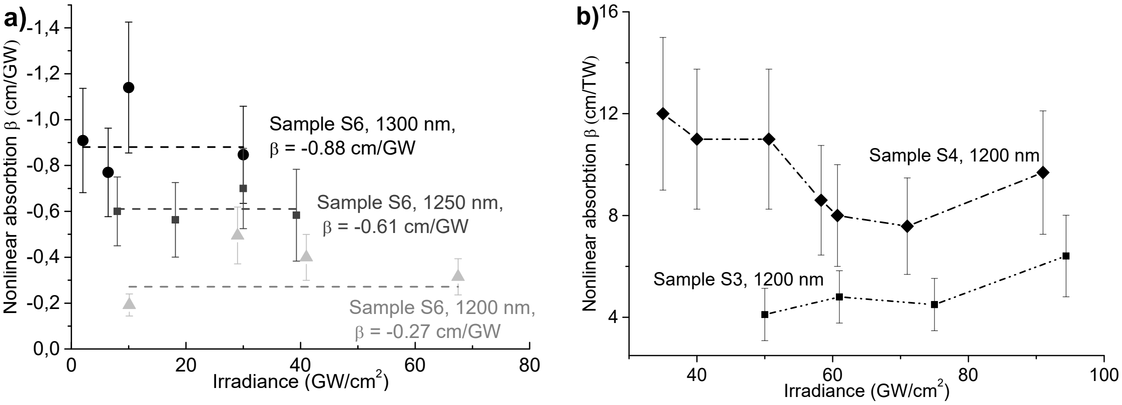

Figure 40. Nonlinear absorption coefficient β associated with $\chi^{(3)}$ susceptibility Ag nanoprisms under different excitation regimes for S6 sample (a) and S3 and S4 samples (b). Error bar represent experimental uncertainty and lines are linear fits with zero slope for a) and curve as eye guidance for b).

Samples S3 and S4 showed different absorptive behavior (Figure 40). Thus, the open aperture Z-scan traces for these samples showed a dip in an optical transmission curve at the beam focal plane, where the beam intensity is highest. The peak is symmetric and it indicates the increased absorption for the high beam intensities. The third-order absorption model accounting for two-photon absorption fits the curve almost perfectly and the absorption coefficient does not depend on the excitation field. This signifies that in these samples the two-photon absorption (TPA) process is dominant. The degenerate nonlinear absorption coefficient is calculated to be 5 cm/TW for sample S3, whereas it was almost doubled (9.7 cm/TW) for sample S4 when the beam wavelength was 1200 nm. Similar (positive) nonlinear absorption was observed by anti-resonant ring interferometric nonlinear spectroscopic techniques in silver colloids with spherical nanoparticles with the femtosecond laser excitation (100 fs, 730 – 800 nm) in the spectral range corresponding to the doubled wave- length of quadrupole plasmonic resonance. In this study, positive nonlinear absorption was accounted for TPA by the quadrupole surface plasmon.

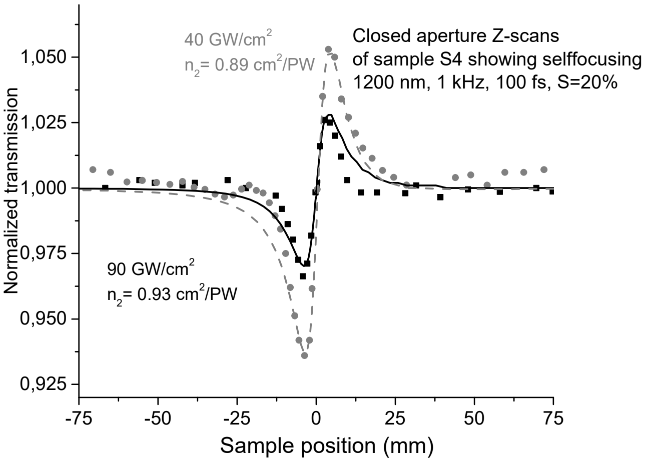

Figure 41. Typical experimental close aperture transmission curves (dots) and theoretical fits (lines) of AgNP sample S4 at different beam intensities. The samples exhibit positive nonlinear absorption (two-photon absorption) as well as positive non- linear refraction (self-focusing). Beam characteristics: 100 fs, 1200 nm, 41 µm at 1/e2.

Nonlinear refraction reflects typical closed aperture transmission curves are shown in the figure 41. Dots denote experimental data and the solid line is a theoretical fit. In our experiment, close aperture Z-scan transmission curve in samples S3-S5 show a typical asymmetric “valley followed by the peak” curve, known to be a signature of positive nonlinear refraction. This type of refraction is also called self-focusing.

Generally, the nonlinear refraction arises from the electronic effect or thermal mechanisms [249]. In solution thermal effect is a slow accumulative process which is associated with the non-radiative relaxation of the excitation energy gathered via linear or nonlinear absorption by the metal NPs. For the aqueous solution the buildup time of such thermal effect is about 30 ns [250], which is much longer than the duration of the laser pulse at 100 fs. In addition, the repetition rate of our laser and optical parametric amplifier tandem is 1 kHz, which is too low to accumulate heat. Therefore, the cause for the nonlinear refraction must be a pure electronic effect.

6.3. Summary of the results

AgNPRs having different lateral dimensions were successfully prepared by seed-mediated method, where particle edge-length varied from 36 to 190 nm. In this chapter presented results showed that aging time of Ag-seed solution is important for the method reproducibility. The most reproducible AgNPRs were obtained when Ag-seed solution was aged 3 – 6 hours. Keeping the same synthesis conditions and varying amount of Ag-seeds LSPR band of AgNPRs can be tuned in an exceptionally wide spectral range. However, the distribution in size tends to increase with increased particle size. Nanoprisms with dimensions of 49 nm (S4) are found to show positive nonlinear absorption, which was identified as two photon absorption and positive nonlinear refraction (self-focusing) in the NIR spectral region (1200 nm) under 30 – 100 GW/cm^2 femtosecond laser excitation. Nanoparticles, which LSPR peak was nearer to the LSPR excitation wavelength (samples S5-S7) have negative nonlinear absorption and behave as saturable absorbers.

Chapter 7. Silver Nanoprisms Self-Assembly on Differently Functionalized Silica Surface

Previous study has demonstrated successful preparation of various size AgNPRs having dipole mode LSPR in 600 – 1060 nm wavelength range. Moreover, prepared particles showed third order optical nonlinearities associated with saturable absorption and two-photon absorption. Though prepared particles have promising application in optics, AgNPRs in liquid form are not suitable for most application and therefore requires some integration into optical component. This can be achieved by embedding AgNPRs into polymer matrix, which can be molded, or coated by various techniques such as spin- or dip-coating. As an alternative, silver nanoparticles as well as AgNPRs can be deposited on functionalized surface via self-assembly. As mentioned in chapter 3, several studies demonstrated self-assembled AgNPRs monolayers on amino group functionalized surface in a large-scale. Due to natural strong interaction between metal surface and amino or thiol group, this process does not require any capping or functionalization of the particle. The bare, chemically active surface of self-assembled AgNPRs and extremely high LSPR intensity provides new applications in areas such as SERS or biosensors. The growing interest in plasmonic nanostructured SERS surfaces, encouraged us to conduct our study on the development of synthesis methods of self-assembled AgNPRs layers. However, latter approach is still lacking deeper understanding about process mechanism and its influencing factors such as degree of functionalization, surface roughness, type of functional group and functionalization method.

This chapter presents a study on AgNPRs self-assembly on differently functionalized silica surface. Such surfaces were prepared by silanization of silica coatings with APTES, AEAPTMS and MPTMS which provide amino, etilendiamino, thiol functionalities respectively. Prepared silanized surfaces and self-assembled AgNPRs layers were studied by FTIR, SEM, UV-Vis spectroscopy and evaluated visually.

7.1. Synthesis of colloidal silica, fabrication of coatings and surface silanization

In this part, base catalyzed silica sol was used. During base catalyzed hydrolysis and condensation reactions, silica spheres are usually formed whose diameter can be varied from nanometer to submicrometer scale. The exact size of the spheres is controlled by the initial ratio of starting materials. At low pH levels (acidic catalysis) silica tends to form linear chains, and no particles are formed [251]. Thus, silica coatings formed from small, 20-40 nanometer scale silica particles, due to the high surface area have more hydroxyl groups than coatings made from acid catalyzed silica sol. Thus, this was the main reason why base catalyzed sol was selected. Accordingly, 3% (w/w) monodisperse colloidal silica in ethanol, with 30 ±11 nm average sphere (figure 42) diameter were made by selecting the appropriate ratio of starting materials [252].

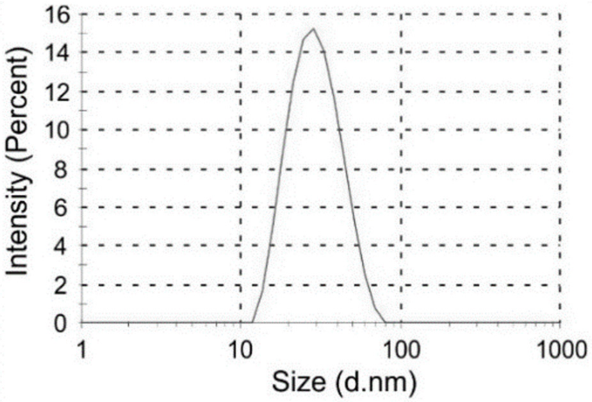

Figure 42. Colloidal silica size distribution diagram measured by DLS

Colloidal silica coatings were prepared by the dip-coating method on precleaned glass substrates. By this method film thickness is controlled by changing withdrawal speed and viscosity of the sol. However, in our case film thickness does not plays a significant role, so we have chosen medium, 40 mm/min withdrawal speed for all samples. These coating parameters resulted in approximately 70 nm thickness coatings. After the coating process, samples were kept for the next step – surface silanization.

Most popular silanization methods involve thermal or room temperature silanization. In thermal silanization dry, commonly non-polar solvents are refluxed in inert atmosphere together with alkoxysilane. By this approach ideally only one layer of silane is formed on the coating surface. However, due to method toxicity it is hardly applicable in large scale. The other method is performed at room temperature and it does not require toxic solvents. By this technique, substrates are kept in a mixture of alcohol, acid or base, water and desired alkoxysilane for few days. This method is more straightforward, but the control of thickness and uniformity of the silane layer is more complicated [253]. Thus, we selected thermal silanization in order to evaluate AgNPRs self-assembly of differently silanized surface. Coated substrates functionalized by – APTES, AEAPTMS, and MPDMS. 3% solution of silane in dry toluene were used in all silanization procedures.

Table 3. Measured water contact angle and SFE values of silanized coatings

Modifying silane	**Water Contact angle, deg.**	**Dispersive Surface free energy, mN/m**	**Polar Surface free energy, mN/m**	**Total Surface free energy, mN/m**
None	40 ±2	36.80	24.27	61.07 ±4.45
APTES	70 ±3	31.16	9.82	40.98 ±5.09
AEAPTMS	67 ±3	25.94	13.55	39.48 ±4.60
MPTMS	55 ±2	37.55	14.94	52.49 ±5.31

To make sure that silanization process was successful, water contact angles (CA) and surface free energy (SFE) were measured in a first place. As shown in Table 3, all silanized coatings have higher CA and smaller total SFE values compared to the non-silanized coating. As a result of high amount of polar hydroxyl groups on the surface, highest wetting exhibit non-functionalized silica coatings. Due to polar amine groups, APTES and AEAPTMS silanised coatings should result in better wetting properties, but grafted carbon chain may cause higher water contact angle value and smaller surface free energy values. MPTMS modified coatings have slightly better wetting properties and higher surface free energy comparing with APTES and AEAPTMS functionalized coatings.

Additionally, silanized coatings were evaluated by UV-Vis spectroscopy. It should be mentioned, that by dip-coating, coatings are formed on both sides of the substrate. Thus, presented transmittance spectra represent absorbance from both sides of substrate. Transmittance spectra shows, that non-silanized silica coatings have anti-reflective properties – transmittance is higher than uncoated glass. This property helps us to observe and evaluate variation of thickness and refractive index in the silanization process. For example, if coating becomes denser refractive index become higher resulting in decrement of the transmittance [254].

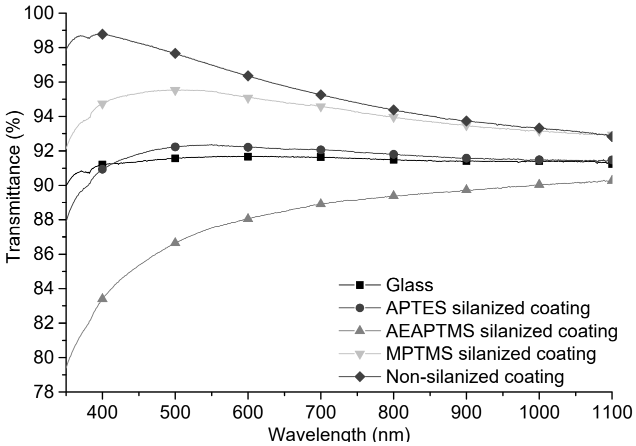

Figure 43. Transmittance spectra of differently silanized coatings.

Obtained spectra (figure 43) clearly shows that APTES and MPTMS silanized coatings have less transmittance than non-silanized coating and transmittance maximums become red-shifted. This indicates an increment in density and/or thickness of the coating. Nevertheless, the transmittance spectra, CA and SFE results clearly demonstrate, that this silanization process was successful.

7.2. Synthesis of AgNPRs

AgNPRs having average edge length of 94 ±15 nm and 921 nm spectral position of LSPR band were prepared by using 560 μL Ag-seed solution. Average particle sizes were calculated from SEM micrographs (figure 44a), obtained particles are plate-like structure and almost all have trigonal or hexagonal shape, but varies in size. Prepared colloidal AgNPRs solution was relatively stable and no significant changes were observed in few months.

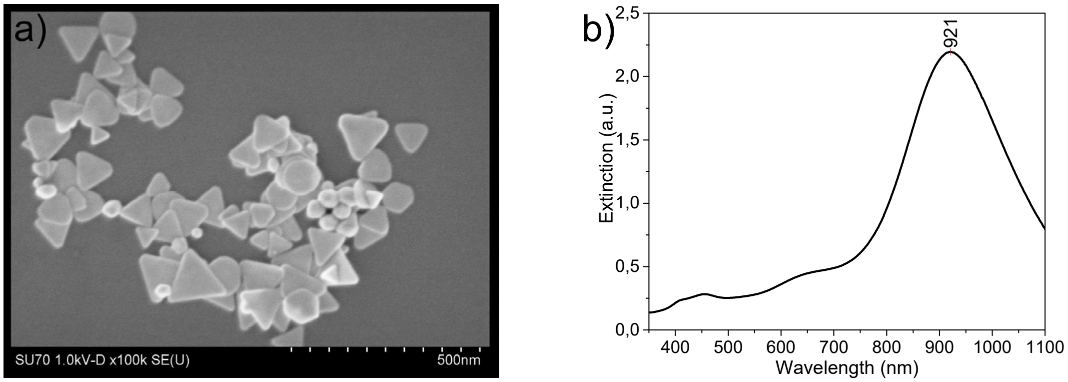

Figure 44. a) SEM image and b) extinction spectrum of prepared AgNPRs solution.

Single SPR band (figure 44b) shows high-intensity absorption at 921 nm, which gives a blue color of AgNPRs colloidal solution. Red shifted SPR peak indicates the presence of high aspect ratio anisotropic triangular AgNPRs or hexagonal particles in the solution. It can also be seen that SPR peak is slightly broadened, but it is common for all the plasmonic particles that have absorption in near-infrared spectral region [255].

7.3. AgNPRs self-assembly on differently silanized surfaces

In this section, we investigated silver NPRs self-assembly on differently silanized silica coatings. We have investigated, which silanized surface is more suitable for assembly of NPRs. Thus, in order to obtain self-assembled silver NPRs layer, functionalized coatings were vertically immersed in plastic vials containing AgNPRs solution and kept for 1 week at room temperature. After this procedure, samples were ready for UV-Vis measurements.

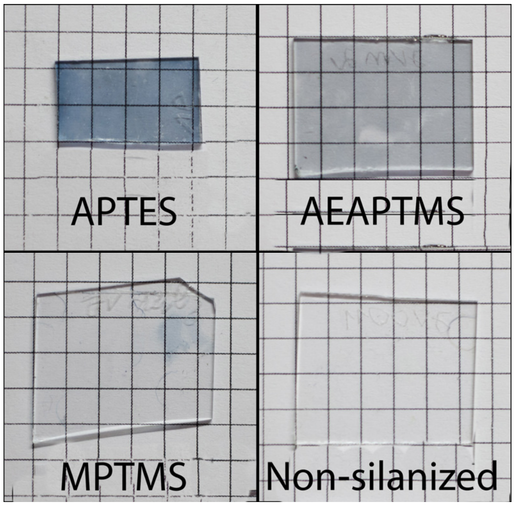

Figure 45. Photographs of prepared AgNPR-silica coatings.

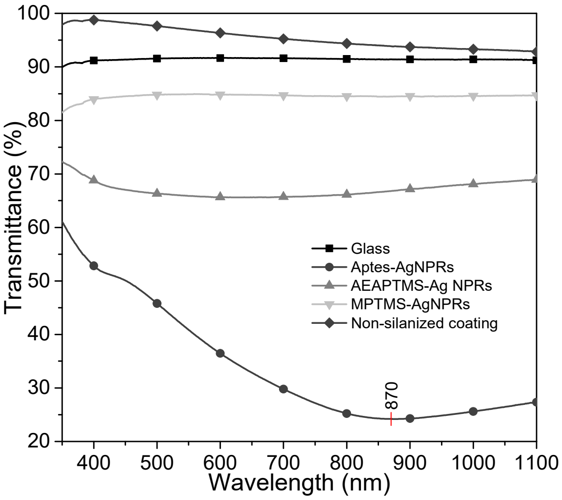

Figure 46. Transmittance spectra of AgNPR-silica coatings.

Firstly, we took pictures of samples (figure 45) to visually evaluate how AgNPRs is assembled on silanized silica coatings. The layer of assembled AgNPRs on APTES silanized coating can be observed visually. The AgNPRs layer results in intensive blue color. Strong absorbance around 870 nm in the case of APTES functionalized coating is observed in presented transmittance spectra (figure 46). Moreover, compared to AgNPRs in solution phase, the LSPR peak of assembled particles becomes broadened and blue shifted. This might be caused by the change of surrounding media of the particle – dielectric environment and the refractive index of surrounding affects position of LSPR [256]. In the case of AEAPTMS functionalized coatings, self-assembly of Ag nanoparticles results in blue-greyish color of deposited layer. This suggests, that large amount of primary and secondary amine groups may induce stronger attraction which results in aggregation of AgNPRs. In fact, no LSPR peak, only broad absorbance is visible in transmittance spectrum of latter sample. Ag NPRs layer is barely visible on MPTMS modified and unmodified coatings.

SEM images of differently silanized AgNPRs self-assembled coatings are presented in figure 47. Most even arrangement of AgNPRs is visible on APTES functionalized coating – particles are arranged mostly as monolayer and noticeable aggregation is minimal. The image of AEAPTMS functionalized surface confirm aggregation of particles and uniform monolayer no longer forms. Consequently, this layer of AgNPRs visually looks grayish and no LSPR mode is observed in transmittance spectrum. Only separate, wide spread particles are observed on MPTMS functionalized coating. The UV-Vis spectra data show weak absorbance of unmodified coating, and no AgNPRs are observed on SEM image.

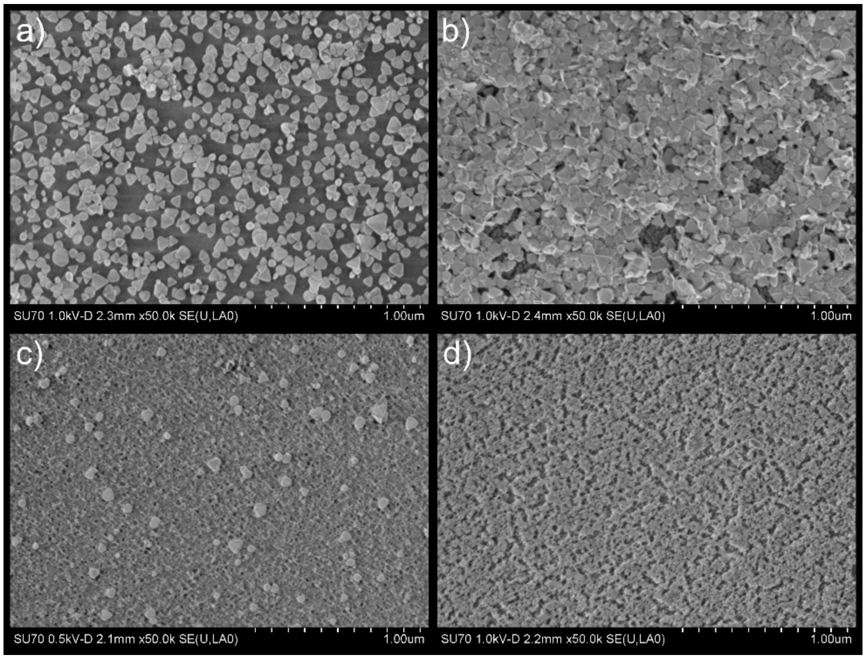

Figure 47. SEM images of AgNPRs-silica coatings: a) silanized by APTES, b) AEAPTMS, c) MPTMS and d) non-silanized.

These results show that surface functionalization is necessary for self-assembly of AgNPRs on silica coating. Non-functionalized surface, which have many hydroxyl groups does not induce AgNPRs assembly. It is also observed, that amino functionalized surfaces have very good binding properties with AgNPRs. However, in the case of AEAPTMS functionalized coatings, a higher amount of amino groups results in aggregation of nanoparticles. APTES modified surface have fewer amino groups, but enough to attract AgNPRs and form a uniform monolayer. Unfortunately, MPTMS functionalized coatings have weaker interaction with AgNPRs than expected. Other researchers have already investigated plasmonic particles interaction with thiol functional groups in solution phase and found strong binding between them [257].

However, it should be emphasized, that there are plenty of factors which have strong influence on self-assembly process. One of them is the outer shell of the particle. In colloidal solution particles are covered by surfactants, so it is hard to measure whether particle or surfactant gives stronger interaction with the silanized surface. In this work high molecular mass PSSS, ionic polymer and sodium citrate were used. Thus, it is possible, that interaction takes place between the surfactant and silanized surface instead of the AgNPR surface. Similar considerations are published by other researchers [26]. On the other hand, the uniformity and chemical properties of functionalized surface have a high influence to self-assembly process. For example, the reactivity of APTES and MPTMS silanes are different, so the quantity of attached functional groups in silanization process also may vary. Moreover, this self-assembly process is a solid-liquid system, where solid is a silanized layer and liquid is water. As known, the amino group is more polar compared to a thiol group. Thus, due to heterogeneous conditions, the activity of thiol group in water can be weaken by hydrophobic effects. Nevertheless, this work showed that APTES functionalized coatings can efficiently attract Silver NPRs and form a uniform monolayer on the surface.

7.4. Summary of the results

Results presented in this chapter showed, that most homogeneous AgNPRs-silica coatings are obtained on surfaces silanized with APTES. AEAPTMS silanized coatings results in aggregation of AgNPRs, while MPTMS functionalized coatings shows low affinity to AgNPRs. Nevertheless, we successfully made functionalized silica coatings by sol-gel method and formed AgNPRs layer on them via self-assembly process. On the other hand, the influence of other surface parameters to AgNPRs self-assembly such as surface roughness, silanization method and others should be further investigated.

Chapter 8. Preparation Self-Assembled Silver Nanoprisms on Amino Group Grafted Silica Coatings

Results presented in chapter 6 showed that most uniform self-assembled AgNPRs layers were obtained when APTES was used for surface silanization. On in other hand, observed unusual aggregation of AgNPRs on AEAPTMS silanized and barely noticeable particle assembly on MPTMS silanized surfaces suggest, that synthesis parameters of proposed method should be optimized. Therefore, in study presented in this chapter we investigated AgNPRs self-assembly on silica coatings silanized by APTES through different methods including thermal silanization in toluene and room temperature silanization in 2-propanol.

Both techniques are widely used for surface functionalization. In thermal silanization, dry non-polar solvents are refluxed in inert atmosphere together with alkoxysilane. Ideally, by this technique, only one layer of silane is formed on the coating surface. However, this method is complex and due to toxicity is hardly applicable in large-scale. The other method is performed at room temperature and it does not require toxic and extra dry solvents. In this technique substrates are kept in a mixture of alcohol, acid, water and desired alkoxysilane for few days. This method is simpler, but control of the thickness and homogeneity of silane layer is more complicated [253]. There we evaluated how differently silanized layer acts with AgNPRs. The process was investigated by atomic force microscopy (AFM), water contact angle measurements (CA), FTIR analysis, and scanning electron microscopy (SEM).

8.1. Synthesis of colloidal silica, fabrication of coatings and surface silanization

Two types of silica sols can be used for the amorphous silica coatings preparation – produced via acid and base catalyzed hydrolysis. As mentioned in experimental section, acid catalyzed silica sol was used in this work. Silica tends to form linear chains at low pH levels (acidic catalysis), and no particles are formed [251]. As mentioned in previous chapter, silica coatings formed from silica nanoparticles have higher porosity and due to the high surface area have more hydroxyl groups than coatings that are made from acid catalyzed silica sol. Therefore, during silanization process, silane molecules can be attached to the porous silica surface more efficiently. However, the reproducibility of surface roughness and porosity, especially at the nanoscale, is questionable. Thus, it is more appropriate to use coatings with similar surface properties for the evaluation of two different silanization methods. Therefore, we selected acid catalyzed hydrolysis method for the preparation of sols.

After the substrates cleaning procedure, coatings were formed using the dip-coating method by using 40 mm/min withdrawal speed for all samples. After the coating process, samples were kept for the next step – surface silanization.

In this study, two silanization techniques were selected – silanization in dry toluene and in acidic 2-propanol solution. In first method silica coatings were silanized by using 0.5%, 1%, 1.5%, 2%, 3% APTES in 2-propanol in presence of 0.1% acetic acid. In the second method, coatings were silanized with 3% APTES in dry toluene.

After silanization, the obtained samples were investigated by AFM to evaluate the uniformity of obtained APTES layer (figure 48). Presented AFM images show, that coatings silanized in 2-propanol form uniform surface when APTES concentration is below 1.5%. Coatings silanized with 2 % and 3 % APTES solutions no longer form the even surface, and micrometer size aggregates are visible. Coatings silanized with 3% APTES in toluene are less uniform – submicrometer size agglomerates are observed.

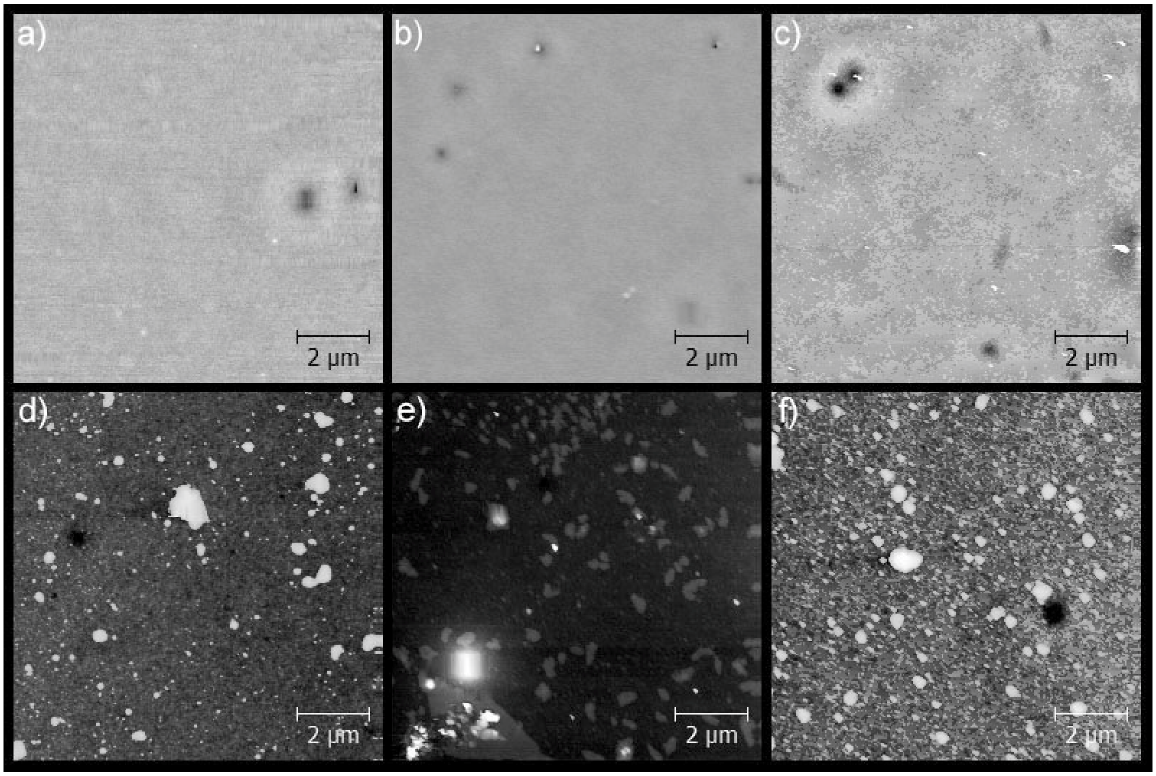

Figure 48. AFM images of differently silanized silica coatings: a) 0.5%, b) 1%, c) 1.5%, d) 2%, e) 3% APTES in 2-propanol and f) 3% APTES in toluene.

Additionally, for these samples water contact angles (CA) were measured. The calculated mean surface roughness (Rq) and CA are presented in Table 4. As one can see from Table 4, calculated mean surface roughness correlates with CA values – increased surface roughness raises CA values.

Table 4. Contact angle and surface roughness of silanized silica coatings

Solvent	**APTES, % (v/v)**	**Contact angle, deg.**	**Surface roughness (Rq), nm**
2-Propanol	0.5%	51 ±2	0.2 ±0.2
	1.0%	56 ±2	0.5 ±0.3
	1.5%	60 ±3	0.4 ±0.3
	2.0%	65 ±4	3.4 ±0.8
	3.0%	59 ±4	3.3 ±0.7
Toluene	3.0%	75 ±6	5.5 ±1.1

Obtained results demonstrate, that coatings silanized in toluene have the lowest uniformity and highest surface roughness. It is necessary to mention, that latter silanization technique is very sensitive to the purity of APTES and water content during silanization procedure [27]. Traces of water and/or presence of APTES oligomers can result in self-polymerization of silane followed by formation of micrometer-sized aggregates. In the case of silanization in 2-propanol, higher content of APTES can also lead to rapid self-polymerization and formation of aggregates. Nevertheless, uniform coatings silanized in 2-propanol can be obtained if optimal amount of APTES is added.

Though this surface silanization method is straightforward and well-studied, silanized surface still must be characterized to make sure, that surface functionalization took place. The presence of amine groups or attached hydrocarbon chains can be determined with FTIR spectroscopy. Unfortunately, when mono- or bilayer of desirable functional groups forms on the surface, conventional FTIR spectrometer equipped with ATR (Attenuated Total Reflectance) module hardly detects vibrations of these functional groups. Therefore, silanized silica coatings were formed on a CaF substrate to increase signal intensity.

FTIR spectra of differently APTES silanized coatings can be seen in figure 49. Due to the negligible difference of FTIR spectra of coatings silanized in 2-propanol solution with various APTES concentration, only one (silanized by 1 % APTES in 2-propanol) spectrum is presented.

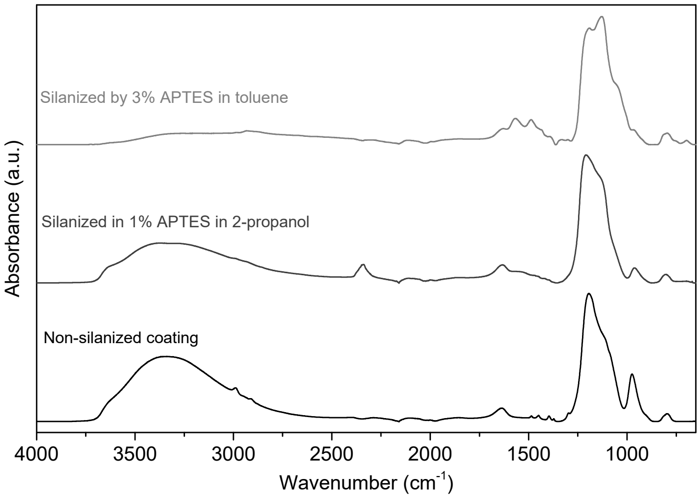

Figure 49. Measured FTIR spectra of silanized silica coatings.

Vibrations at 1293 cm^{-1} are typical for the three-dimensional -Si-O-Si- framework and the strong absorbance at 3338 cm^{-1} is from silica hydroxyl groups and absorbed water molecules. It is necessary to mention that the overlap of this peak with characteristic amine group vibrations in 3500-3300 cm^{-1} range make FTIR analysis more complicated. Nevertheless, it is clear that the intensity of Si-OH peak is considerably lower in both silanized coatings. Another two characteristic medium intensity amine group peaks are observed at 1487 and 1567 cm^{-1}, which are clearly visible in toluene silanized coating and small shoulder observable in 2-propanol silanized coating. The shoulder at 1128 cm^{-1} is slightly higher in both silanized samples, which also indicates primary amine group vibrations [258]. It can be concluded that coating modification performed in toluene leads to the higher amount of the attached amine groups on the surface than silanized in 2-propanol.

8.2. AgNPRs self-assembly on silanized surfaces

Further, we investigated AgNPRs self-assembly on differently silanized silica coatings. We tried to find out which silanized surface is more suitable for assembly of AgNPRs. Considering obtained surface uniformity of coatings, we selected coatings silanized by 0.5 %, 1.0 % 1.5 % APTES solution in 2-propanol and 3.0 % APTES in toluene. As in previous chapter, in order to obtain the self-assembled AgNPRs layer, functionalized coatings were vertically immersed in the plastic vials containing AgNPRs solution and kept for 1 week at room temperature. After this procedure, samples were ready for SEM analysis. In this experiment the same AgNPRs solution was used, which was characterized in chapter 7.

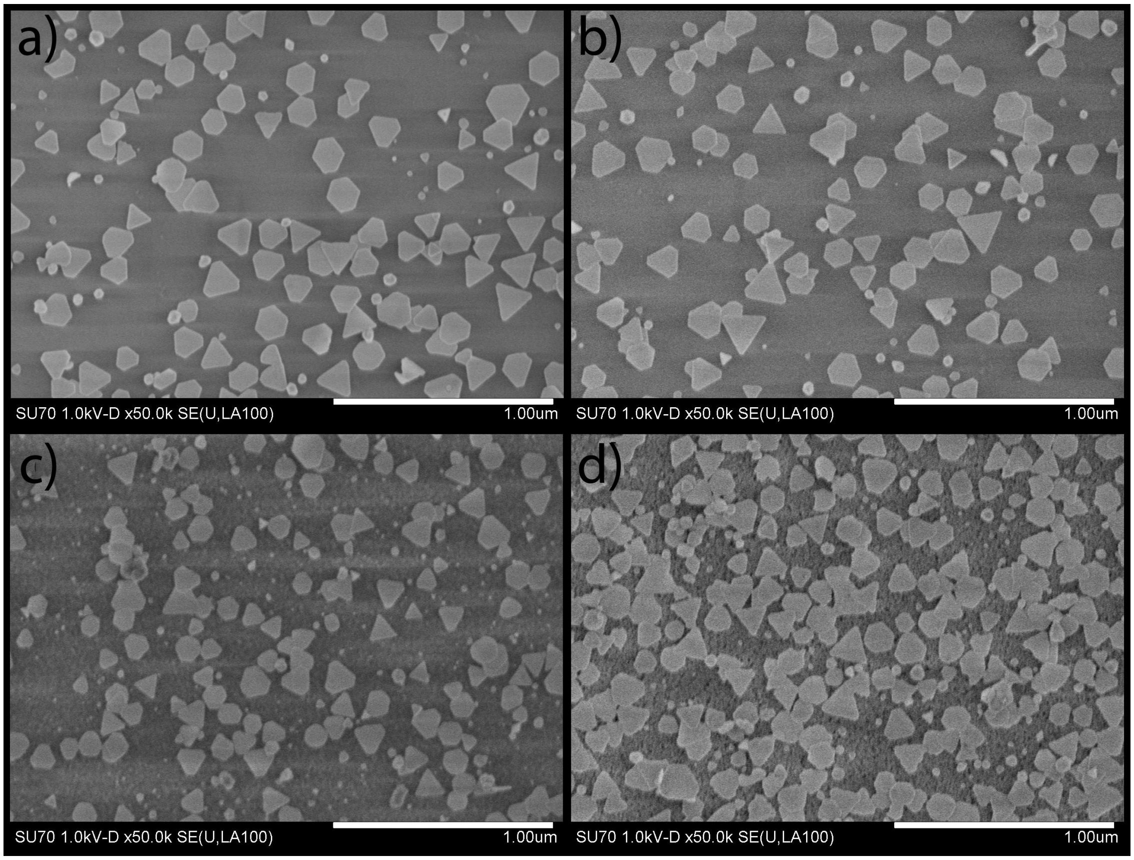

Figure 50. SEM images of silanized and AgNPRs deposited silica coatings: a) 0.5 %, b) 1 %, c) 1.5 % APTES in 2-propanol and d) 3 % APTES in toluene.

As one can see from obtained SEM images (figure 50) the deposited layer of AgNPRs is visible on all silanized coatings. The density of arranged AgNPRs layer is very similar on all coatings silanized in 2-propanol. Coatings silanized in toluene have a denser distribution of AgNPRs. FTIR analysis showed that coatings silanized in toluene have higher amount of amino groups than in 2-propanol silanized samples. We believe that silver nanoparticles have denser arrangement in coatings silanized in toluene due to higher amount of grafted APTES groups on the surface. However, silica coatings silanized in toluene are considerably less uniform than coatings silanized in 2-propanol. Contrary to our expectations, surface non-uniformity does not reduce the amount of deposited AgNPRs. The non-uniformity of coatings modified in toluene increases light scattering which makes them less attractive for some applications such as optical devices. Thus, coatings silanized in 2-propanol are more uniform, silanization procedure is simple and does not require hazardous solvents. Moreover, AgNPRs layer can be deposited via self-assembly insufficient surface coverage. These advantages make them promising candidates for straightforward production of SERS substrates or optical components.

8.3. Summary of the results

In this brief study we successfully synthesized silica coatings by sol-gel method, functionalized with amino groups and deposited layer of AgNPRs. Most uniform silanized coatings were obtained by silanization in 2-pronanol, when amount of APTES is below 2%. The greater amount of amino groups was obtained by silanization in toluene. However, AFM analysis shows non-uniform layer of silica when silanization in toluene is carried out. Nevertheless, the highest surface coverage with AgNPRs was obtained on coatings silanized in toluene. Though silanization in 2-propanol results in widespread AgNPRs layer, the good uniformity and simpler silanization process make them more attractive for application as SERS substrates.

Chapter 9. Controllable Formation of High Density SERS-Active Silver Nanoprism Layers on Hybrid Silica-APTES Coatings

Results presented in chapter 7 and 8 already showed, that typical silanization results in sparsely distributed AgNPRs or coating non-uniformities. The self-assembly of AgNPRs directly depends on the uniformity of silanized surface and amount of attached amino groups. Moreover, amount of attached amino groups and their distribution are hardly controllable due to short lived active hydroxyl groups, non-perfect silanization process and purity of used reagents.

In this chapter influence of various parameters to the AgNPRs self-assembly process was investigated. The new proposed approach is based on fabricating hybrid silica-APTES coatings on glass substrates via the sol-gel process, followed by assembly of AgNPRs. In this way uniform aminized surfaces are accessible in a more reproducible manner as compared to direct surface aminization. The main advantage of the proposed method is the possibility to control AgNPRs deposition through the number of amine groups introduced to the surface. Uniformity, density and deposition rate of the assembled AgNPRs layers are important parameters, which will be affected by amino group distribution. We investigated AgNPRs deposition process on coatings containing different amounts of APTES. The obtained AgNPRs aggregation level and size effects to their performance in SERS is also reported.

9.1. Preparation of hybrid silica-APTES coatings

Hybrid silica coatings containing various amounts of APTES were prepared by increasing APTES molar fraction from 0.02 to 0.30 while decreasing TEOS molar fraction from 0.98 to 0.70 respectively. In order to obtain uniform coatings precise control of hydrolysis and condensation processes of the sol is neccessery. Due to natural APTES ability to induce hydrolysis-condensation reaction absolute ethanol was used and no additional water was added to the initial sol. When APTES molar fraction was kept above 0.06 visually uniform coatings were obtained. However, low magnification SEM images (figure 51) revealed the surface being coated with micron-sized droplets rather than forming a homogenous layer.

Coatings prepared with the molar fraction of APTES above 0.06 are homogenous with a few minor defects caused by dust and glass substrates imperfections. It highly suggests that at low concentration of APTES, hydrolysis and condensation processes are not sufficient and may result in a non-uniform coating with segregated domains.

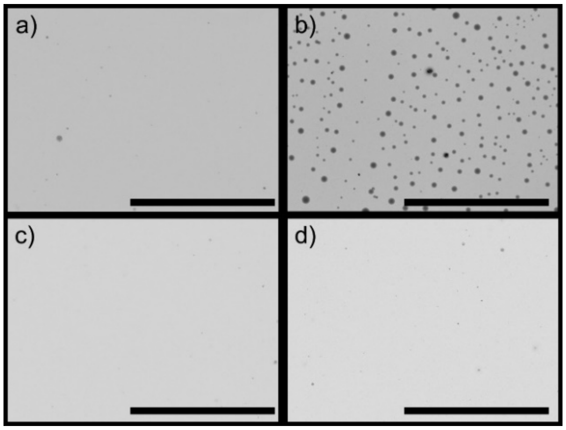

Figure 51. SEM images of prepared silica-APTES coatings by varying APTES mole fraction: a) 0; b) 0.04; c)0.10 d)0.30; (scale bar 100 µm).

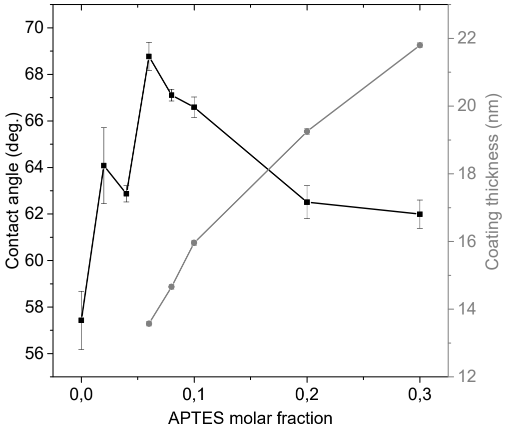

Figure 52. Water contact angle (black line) and thickness (gray line) of the prepared coatings versus APTES molar fraction.

Layer thickness and water contact angle measurements of the prepared hybrid coatings as a function of TEOS/APTES molar ratio are presented in Figure 52. The obtained coatings are relatively thin and tend to thicken gradually from 13 to 22 nm as APTES molar fraction raises. The highest water contact angle was obtained of the coating with 0.06 molar fraction of APTES and it starts to decrease gradually by adding more APTES. Water contact angle is highly sensitive to the surface properties as polarity, porosity, and roughness. Normally, silica surface modification with APTES, due to less polar amine groups and increased roughness, results in increased surface hydrophobicity. Therefore, gradual decrease of contact angle might be related to the reduced surface roughness and/or decreased amount of amine groups. To clarify coatings were further studied by FTIR.

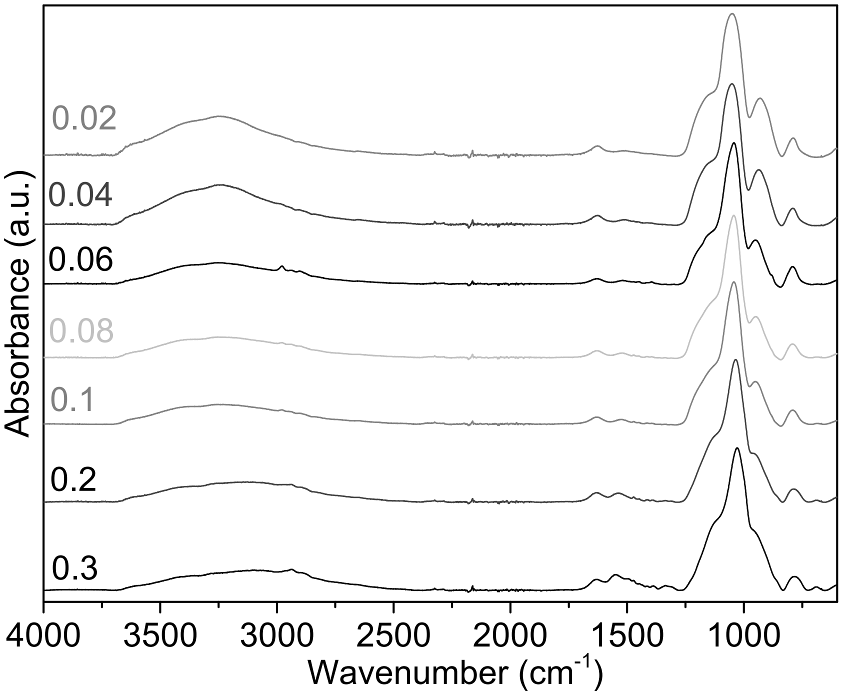

Figure 53. FTIR spectra of the prepared coatings by varying APTES molar fraction.

FTIR spectra (figure 53) of the prepared coatings show high intensity of the corresponding of Si-O-Si vibrations at 1050 cm^{-1} and medium intensity of Si-OH stretches at 789 cm^{-1}. The characteristic primary amine vibrations in the region 3400 – 3300 cm^{-1} are hidden under absorbed H_2O vibrations. Other weak NH_2 group vibrations at 1549 cm $^{-1}$ became more intense with increasing amounts of APTES. Moreover, the intensity of the broad signal in the range 3500 – 3000 cm^{-1} resulting from adsorbed H_2O and well as Si-OH stretch at 789 cm^{-1} are reduced with increasing APTES molar fraction, which indicates decreased amount of free Si-OH groups. The weak intensity of N-H stretch at 689 cm^{-1} becomes visible at quite high APTES molar ratios, i.e. 0.1 and higher. The observation of increased characteristic N-H vibrations and reduced intensity of Si-OH bands by adding more APTES, let us to conclude, that increasing APTES amounts indeed results in increased amino group content on the glass surfaces and hence successful surface silanization procedure.

9.2. Synthesis and characterization of AgNPRs colloids

For the synthesis of AgNPRs seed-mediated method was selected, which allows easy control of AgNPRs size by changing seed concentration in the initial particle synthesis step. Three colloidal solutions of different size AgNPRs were prepared as described in the experimental section. Particles lateral dimensions were calculated from SEM micrographs. In Table 5 presented data shows, that lower amount of seed solution results in larger particle size and thus subsequent red-shifted LSPR peak. But narrower particle size distribution was obtained with higher amount of seed solution used. Prepared colloids were stable at ambient conditions and no dissolution or colour change was noticed within several weeks.

Table 5. Experimental details of the prepared AgNPRs colloids

Sample name	Added amount of seed solution, µL	LSPR peak position, nm	Average tip-edge length, nm (SEM)
AgNPR01	2000	664	34 ±8
AgNPR02	1000	756	50 ±11
AgNPR03	200	1000	120 ±25

Prismatic shape particles dominate in all prepared AgNPRs solutions although trace amounts of disc or hexagon shaped particles could be detected. Larger particles distinguish by more prismatic shape and higher size deviations while smaller particles have somewhat more irregular shape, but fewer size deviations. High reproducibility of the seed-mediated methodology allows access to larger quantities of AgNPRs colloids necessary for deposition studies and weights out the wider size and shape distribution.

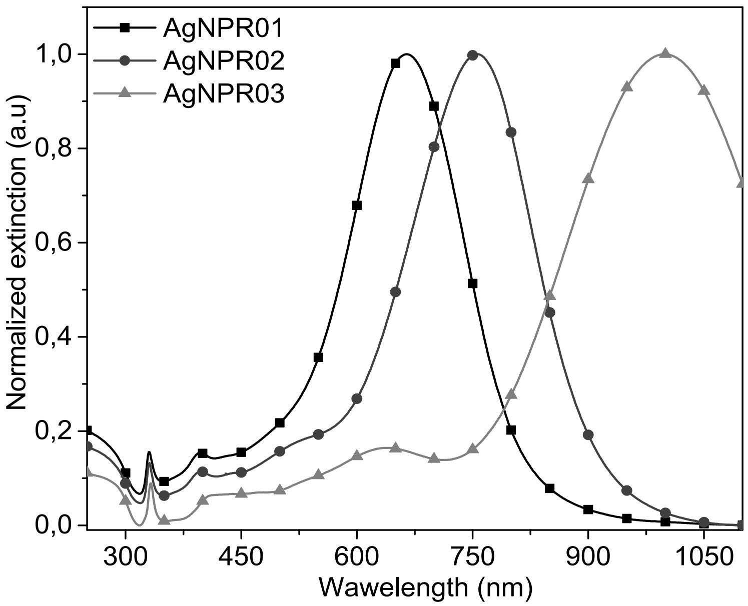

Figure 54. Extinction spectra of synthesized AgNPRs colloids.

The excitation spectra of the synthesized AgNPRs (Figure 54) show characteristic high absorbance LSPR peaks of AgNPRs. An additional peak at 400 nm, observed in first two samples with smallest particles (AgNPR01 and AgNPR02), may be assigned to the residue of small spherical shape particles which did not grow into AgNPRs. Moreover, broadening of dipole mode peak is observed in the case of larger particles, which is attributed to higher polydispersity and scattering effects. Nevertheless, high-intensity dipole mode LSPR peaks of the prepared colloidal sols confirms high yield of the synthesized AgNPRs.

9.3. Deposition of AgNPRs layers on silica-APTES coatings

Medium size AgNPR particles sample (AgNPR002) was selected to investigate the influence of APTES amount to the deposition rate, uniformity and surface pattern of deposited nanoparticle layers.

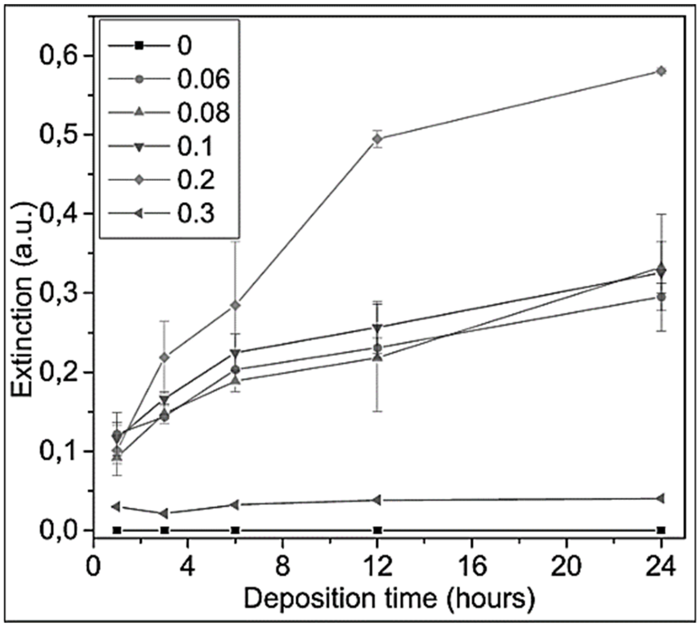

Figure 55. AgNPRs deposition rate curves of silica-APTES coatings prepared by using various APTES molar fractions.

Figure 55 represents dipole mode LSPR absorbance peak intensity as a function of AgNPRs deposition time. The deposition process was monitored for 24 hours. No deposition of AgNPRs onto glass substrate without APTES was observed. The deposition rates on coatings with APTES of molar fraction in the series of 0.06-0.1 are very similar and show consistent growth of particle layer over 24 hours monitored. Deposition rate highly increases when 0.2 molar fraction of APTES was used, but process slows down after 12 hours. With APTES molar fraction of 0.3 strong aggregation of AgNPRs took place throughout whole volume of the sample causing greyish precipitates on the substrate surface as well as container walls. Excessive aggregation could be seen already after 3 hours since the initial stage. AgNPRs layers on coatings with 0.06-0.1 molar fraction of APTES are visually uniform in all surface area and due to strong LSPR in longer wavelengths have solid blue colour.

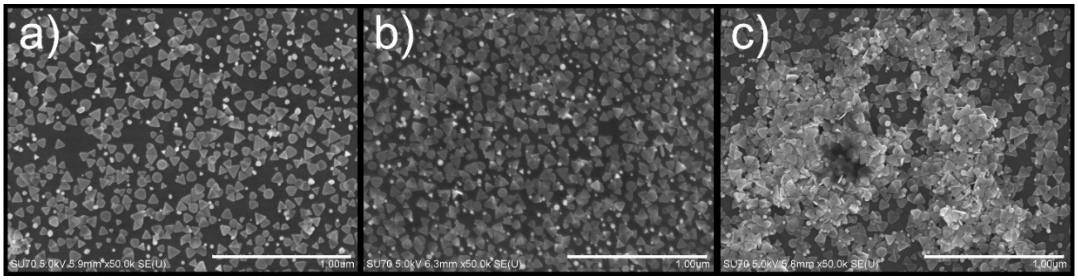

Figure 56. SEM images of deposited AgNPRs layers on silica-APTES coatings prepared by using various APTES molar fractions: a) 0.06; b) 0.10; c) 0.30 (scale bar 1µm).

A constant slight increase in colour intensity is also noticeable with increasing amount of APTES in this series. AgNPRs layer on coating with the highest amount of APTES (0.30) have greyish blue colour and contain both uncovered areas and islands of AgNPRs aggregates (figure 56). With higher APTES content, AgNPRs tend to form micron-sized aggregates with high loss of LSPR. These observations clearly show that amount of APTES plays crucial role not only on the deposition rate of AgNPRs layer but also on the stability of colloidal AgNPRs solution.

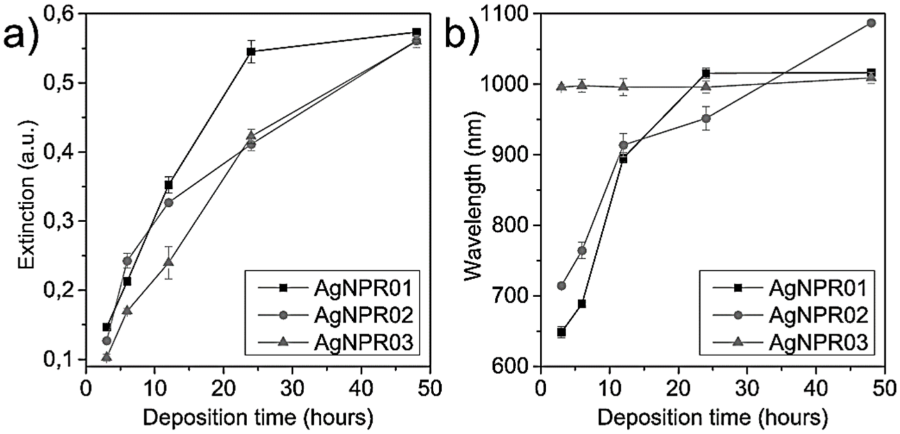

Figure 57. AgNPRs deposition rate curves, displaying: a) deposition rate b) LSPR peak position shift against deposition time.

Since the best coatings with evenly aggregated AgNPRs were obtained with APTES molar ratio of 0.10 these conditions were chosen for further study on the effect of particle size for their deposition. In this case, deposition process was monitored for a longer period of time – up to 48 hours. Extinction curves of the obtained AgNPRs layers as a function of deposition time are presented in Figure 57a. At the beginning smaller AgNPRs tend to deposit on the surface more rapidly while larger particles show more constant growth of AgNPR layer. However, the overall deposition rates of all size particles are similar, resulting in just a slight difference in absorbance after 48 hours. It can be explained by different mobility of smaller particles compared with larger particles. Small AgNPRs are more mobile, therefore the probability them to be attached to the surface is higher. On the other hand, eventually deposition slows down as surface gets more covered by AgNPRs. As a result, the surface covering after 48 hours is similar in both cases despite small particle aggregation starts off faster. LSPR peak position of all AgNPRs deposited glass slides fall into 900 – 1100 nm range. Red-shift of LSPR peak was observed over time as amount of deposited AgNPRs increased (Figure 57b). Surprisingly, the largest shift was detected when a colloid of the smallest particles (AgNPR01) was used, while using large particles resulted in less significant shift. These shifts can be associated with the coupling of LSPR dipole mode peak arising from AgNPRs aggregation when two or more plasmonic particles are in close distance - phenomena already described in detail by *Kotkowiak M.* [259].

SEM images of the obtained AgNPRs layers (Figure 58) correlate well with deposition rate graphs. As compared to larger particles (AgNPR02 and AgNPR03), small particles (AgNPR01) deposit quicker resulting in high surface covering in just 3 hours since the start of the experiment. After 24 hours, surface was highly covered by small particles while uncovered areas were still visible in the case of large particles. Full surface covering with large particles was achieved after 48 hours. After the same deposition duration small and medium (AgNPR01 and AgNPR02) particles started to form large irregular shape particles on top of uniform AgNPRs layer. Note, that these conglomerates were not detected in the stock solutions of AgNPRs which means that they were formed during the deposition process.

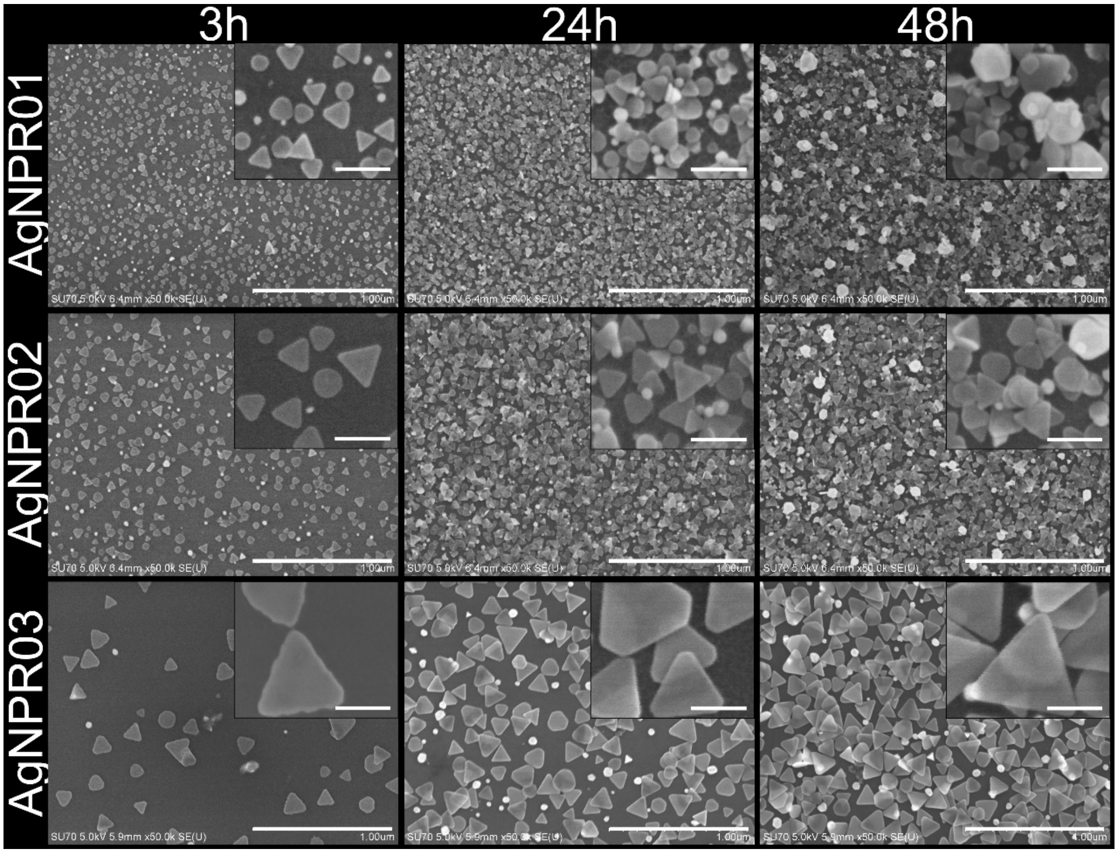

Figure 58. SEM images of deposited various size AgNPRs against different deposition time (scale bar 1 µm, inset scale bar 100 nm)

The exact mechanism of formation of the irregularly shaped particles remains unclear and requires more detailed study. Deposition process does not stop after full surface covering – AgNPRs assembly continues and forms additional layer. It strongly implies, that electrostatic interaction between substrate decorated with amino groups and free AgNPRs is very strong. Particle adsorption and aggregation mechanism has already been studied in the case of spherical gold nanoparticles [33]. It was suggested that adsorbed particles have random mobility over the aminized surface and that hydrophobic nature of metal nanoparticle are main driving forces leading to their aggregation. Our results shares analogy to the proposed mechanism.

9.4. SERS study of deposited AgNPRs layers

With new AgNPRs coatings in hand their performance in SERS was investigated. As the sample of analytical object we selected uric acid. Owning to 4 nitrogen atoms in its molecular structure uric acid absorbs easily on silver nanoparticle surface. Uric acid is non-resonant molecule and does not enhance Raman signal itself. Thus, it is suitable analyte for evaluation of SERS enhancement of deposited AgNPRs layers. Furthermore, determination of uric acid by SERS has already been presented in other research works which results can be used for reference [260, 261]. Development of sensitive methods for uric acid sensing is extremely important, since its concentration deviations in the blood stream (>0.4 mM) might indicate serious medical conditions such as preeclampsia.

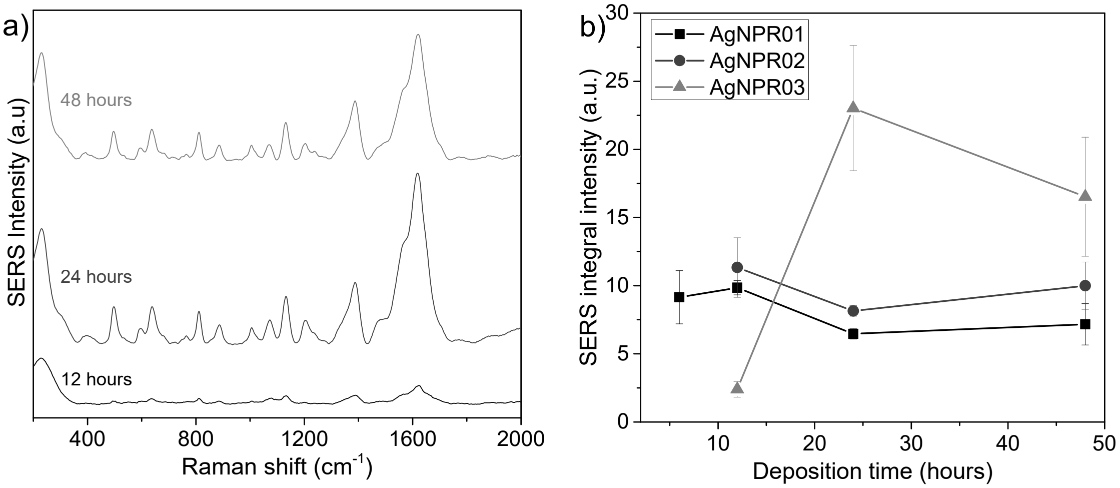

Figure 59. SERS spectra of AgNPR03 deposited layer (a) and SERS integral intensity at 500 cm^{-1} (CN bending/in-plane ring deformation) against deposition time of all AgNPR layers (b).

The series of glass substrates with different AgNPRs layers was subjected to SERS enhancement studies. Uric acid concentration was kept very low (0.1 mM) and no Raman signal could be detected of the plain sample. Figure 59 represents SERS intensity versus deposition time of layers consisting different size AgNPRs. No signal was observed with the coatings deposited only for 3 hours. Only a weak signal was detected on coatings deposited for 6 hours with the smallest particles in the series (AgNPR01). In the case of AgNPR02 and AgNPR03, SERS signal was observed only with coatings which were deposited for 12 hours. Coatings assembled from small AgNPRs (AgNPR01) show rather low SERS enhancement, which decreases even more with increasing AgNPRs deposition time. Very similar behaviour can be seen in the case of medium size particles. Highest SERS enhancement was observed on coatings with large particles (AgNPR03) deposited for 24 hours. Though the layer of small and medium AgNPRs have LSPR peak approximately at 1000 nm, which is near to the wavelength of the laser used, the SERS signal intensity remains low. High SERS enhancement is indeed associated with LSPR of individual particle and not to collective LSPR of aggregated particles. On the other hand, solutions of small particles have a lower fraction of well-defined shape AgNPRs, which might also be responsible for their lower SERS sensitivity. It suggests that small aggregated particles offer smaller surface area for interaction with analyte molecule than individual particles, which in turn results in lower intensity of SERS signal. Analytical enhancement factors (AEF) were calculated using the reported method [262]. In the most successful case in the series i.e. the sample AGNPR003 with 24 hours deposition AEF was found to be 2.7 x 10^4. As to compare to other reports the AEF value obtained is rather low, however, present study reveals the influence of amine group content, deposition time and particle size on AgNPRs behaviour when particles are in contact to aminized surface.

9.5. Summary of the results

In this chapter the uniform hybrid silica coatings containing different APTES amounts were prepared via sol-gel process and utilized for the assembly of AgNPRs. It was found, that amount of APTES is crucial for deposition rate and behaviour of AgNPRs - high APTES concentration leads to rapid aggregation and particle dissolution. Nevertheless, deposition and aggregation rates can be slightly adjusted when moderate amount of APTES is used (0.06 – 0.20 molar ratio of APTES). Excitation spectra and SEM images of deposited AgNPRs layers showed that in comparison with large particles (120 nm), small AgNPRs (34 nm) have higher deposition and subsequent aggregation rates which result in broadening as well as strong red-shift of LSPR dipole mode band. The deposition rate of large particles is lower which gives less aggregated AgNPRs layer and only slight shift of LSPR band. SERS study revealed, the highest enhancement occurs on coatings containing large particles where LSPR band is near laser excitation wavelength (1064 nm). Due to the coupling of LSPR dipole mode of aggregated particles, final LSPR position of coatings deposited from small particles was near laser excitation wavelength. Thus, the registered SERS signal was much weaker comparing with large particles as excessive aggregation reduce the SERS performance. It lets to conclude that SERS enhancement depends more on individual particle LSPR and not collective LSPR of aggregated particles. Although comparing to other reports [222, 263, 264] AEF achieved in this study is considerably lower, it provided a deeper insight into AgNPRs assembly events on aminized surfaces and its importance to SERS enhancement.

Chapter 10. Conclusions

1. Research results showed, that the highest colloidal stability of SWCNTs in ethanol is obtained with surfactant P4VP, while PVP works only at low nanotube concentrations. The use of Triton X-100 and Triton X-305 surfactants resulted only short time stability of SWCNTs dispersions at low nanotube concentrations.
2. Saturable absorption experiments showed better performance of semiconductive SWCNT compared to unsorted ones – they have lower non-saturable loses and lower saturation power.
3. SWCNT-silica composite coatings show higher thermal stability compared to polymeric SWCNT-P4VP coatings. Only negligible degradation was observed on SWCNT-silica samples heated at 400 ^{o}C,
4. Smaller AgNPRs (~50 nm) are found to show positive nonlinear absorption, which was identified as two photon absorption and positive nonlinear refraction (self-focusing) in the NIR spectral region (1200 nm) under 30 – 100 GW/cm^2 femtosecond laser excitation. Nanoparticles (~150 nm), which LSPR peak was nearer to the excitation wavelength have negative nonlinear absorption and behave as saturable absorbers.
5. The uniform AgNPRs self-assembly was observed on surfaces silanized with APTES. AEAPTMS silanized coatings induced an aggregation of AgNPRs, while MPTMS silanized coatings resulted in very sparsely distributed AgNPRs.
6. Most uniform silanized coatings were obtained by silanization in 2-pronanol, when used amount of APTES is below 2%, but highest surface coverage with AgNPRs was obtained on coatings silanized in toluene.
7. It was found, that in prepared hybrid silica-APTES coatings amount of used APTES is crucial for deposition rate and behaviour of AgNPRs on

surface - high APTES concentration leads to rapid aggregation and particle precipitation. Nevertheless, deposition and aggregation rates can be slightly adjusted when moderate amount of APTES is used (0.06-0.20 molar ratio of APTES).

8. The deposition rate of large particles (~120 nm) is lower which gives less aggregated AgNPRs layer and only slight shift of LSPR band. Small AgNPRs (~34 nm) have higher deposition and subsequent aggregation rates which result in broadening as well as strong red-shift of LSPR dipole mode band.
9. SERS study revealed, the highest enhancement occurs on coatings containing large particles (~120 nm) where LSPR band is near laser excitation wavelength (1064 nm) and excessive aggregation of AgNPRs reduces the SERS performance.

Chapter 11. List of Publications and Conference Participation

11.1. List of publications

1. Pilipavicius, J., Sakalauskas, D., Beganskiene, A., Kareiva, A., "Synthesis of Silica-Carbon Nanotube Composite Materials and Their Application for Laser Systems", *IOP Conference Series: Materials Science and Engineering*, **2012**. 38, p. 012052.
2. Alesenkov, A., Pilipavicius, J., Beganskiene, A., Sirutkaitis, R.,Sirutkaitis, V., "Nonlinear Properties of Silver Nanoparticles Explored by A Femtosecond Z-Scan Technique", *Lithuanian Journal of Physics*, **2015**. 55, p. 100-109.
3. Pilipavicius, J., Chodosovskaja, A., Beganskiene, A., Kareiva, A., "Silver nanoprisms self-assembly on differently functionalized silica surface", *IOP Conference Series: Materials Science and Engineering*, **2015**. 77, p. 012006.
4. Pilipavicius, J., Chodosovskaja, A., Beganskiene, A., Kareiva, A., "Formation of Silver Nanoplates Layer on Amino Group Grafted Silica Coatings", *Materials Science-Medziagotyra*, **2016**. 22, -In Press.
5. Pilipavicius, J., Kaleinikaite, R., Pucetaite, M., Velicka, M., Kareiva, A., Beganskiene, A., "Controllable formation of high density SERS-active silver nanoprism layers on hybrid silica-APTES coatings", *Applied Surface Science*, **2016**. 377, p. 134-140.

11.2. Published contributions to academic conferences

1. Pilipavičius, J., Sakalauskas, D., A., Beganskienė, A., Kareiva, A. “Synthesis of silica-carbon nanotube composite materials and their applications on laser systems”, *Functional materials and nanotechnologies (FM&NT-2012)*, Riga, Latvia, April 17-20, **2012**, p. 256

2. Pilipavičius, J., Rusteika, N., Kaušas, A., Beganskienė, A., Kareiva, A. “Silica-carbon Nanotubes Composite Coatings as Saturable Absorbers”, *2012 IEEE 12th International Conference on Nanotechnology (IEEE-NANO)*, Birmingham, United Kingdom, August 20-23, **2012**, p. 1-4
3. Pilipavičius, J., Rusteika, N., Kaušas, A., Beganskienė, A., Kareiva, A. “Making Silica-Carbon Nanotube Composite Materials for non-linear Optics” *2nd International Conference on Competitive Materials and Technology Processes*, Miskolc-Lillafüred, Hungary October 8-12, **2012**, p. 96.
4. Pilipavičius, J., Rusteika, N., Kaušas, A., Beganskienė, A., Kareiva, A**.** “Synthesis of silica-carbon nanotube composites by sol-gel method” *Золь-гель 2012: 2-я конференция стран СНГ*, Sevastopol, Ukraine, September 18-20, **2012**, p. 33
5. Pilipavičius, J., Sakalauskas D., Rusteika, N., Kaušas, A., Beganskienė, A., Kareiva, “Synthesis of carbon nanotube composite coatings for ultrafast mode-locking”, *Chemistry and chemical technology of inorganic materials*, Kaunas, Lithuania, **2012**, p. 120-126
6. Alesenkov, A., Adomaitis, M., Pilipavičius, J., Beganskienė, A., Sirutkaitis, V., “Nanokompozitinių medžiagų netiesinių optinių savybių tyrimas plačiame spektro ruože z-skenavimo metodu su femtosekundiniais lazerio impulsais”, *40-oji Lietuvos nacionalinė fizikos konferencija*, Vilnius, Lithuania, **2013**, June 10-12, p. 287.
7. Pilipavicius, J., Chodosovskaja, A., Beganskiene, A., Kareiva, A., “Silver nanoprisms self-assembly on differently functionalized silica surface”, *Joint 12th Russia/CIS/Baltic/Japan symposium on ferroelectricity and 9th international conference functional materials and nanotechnologies*, Riga, Latvia, **2014**, September 29-October 2, p. 287.
8. Pučetaitė, M., Velička, M., Pilipavičius, J., Šablinskas, V., “Application of SERS spectroscopy for detection of uric acid in biological fluids”, 4*1-oji*

Lietuvos nacionalinė fizikos konferencija, Vilnius, Lithuania, **2015**. June 17-16, p. 76.

9. Pilipavicius, J., Chodosovskaja, A., Beganskiene, A., Kareiva, A., “Silver nanoplates - silica composite coatings via sol-gel route”, *Chemistry and chemical technology 2015*, Vilnius, Lithuania, **2015**, January 23, p. 125-128

11.3. Publications not included in the thesis

1. Pilipavicius, J., Kazadojev, I., Beganskiene, A., Melninkaitis, A., Sirutkaitis, V.,Kareiva, A., "Hydrophobic Antireflective Silica Coatings via Sol-gel Process", *Materials Science-Medziagotyra*, **2008**. *14,* p. 283-287.
2. Aleknavicius, A.A., Smilingis, R., Grishin, M., Michailovas, A., Michailovas, K., Pilipavicius, J., Girdauskas, V.,Gabalis, M., "Multi-disk: concept and realisation of a collinearly pumped multiple thin disk active medium", *Quantum Electronics*, **2011**. *41,* p. 590-594.
3. Abakeviciene, B., Zalga, A., Tautkus, S., Pilipavicius, J., Navickas, E., Kareiva, A.,Tamulevicius, S., "Synthesis of YSZ thin films by the novel aqueous sol-gel citrate-precursor method", *Solid State Ionics*, **2012**. *225,* p. 73-76.
4. Pucetaite, M., Velicka, M., Pilipavicius, J., Beganskiene, A., Ceponkus, J.,Sablinskas, V., "Uric acid detection by means of SERS spectroscopy on dried Ag colloidal drops", *Journal of Raman Spectroscopy*, **2016** –In Press.

Chapter 12. References

1. Scardaci, V., Sun, Z.P., Wang, F., Rozhin, A.G., Hasan, T., Hennrich, F., White, I.H., Milne, W.I.,Ferrari, A.C., *Adv Mater*, **2008**. *20,* p. 4040-4043.
2. Sun, Z., Rozhin, A.G., Wang, F., Scardaci, V., Milne, W.I., White, I.H., Hennrich, F.,Ferrari, A.C., *Appl Phys Lett*, **2008**. *93,* p. 061114.
3. Tatsuura, S., Furuki, M., Sato, Y., Iwasa, I., Tian, M.,Mitsu, H., *Adv Mater*, **2003**. *15,* p. 534-537.
4. Hasan, T., Sun, Z., Wang, F., Bonaccorso, F., Tan, P.H., Rozhin, A.G.,Ferrari, A.C., *Adv Mater*, **2009**. *21,* p. 3874-3899.
5. Gavalas, V.G., Andrews, R., Bhattacharyya, D.,Bachas, L.G., *Nano Lett*, **2001**. *1,* p. 719-721.
6. Shiohara, A., Wang, Y.S.,Liz-Marzan, L.M., *J Photoch Photobio C*, **2014**. *21,* p. 2-25.
7. Marquestaut, N., Petit, Y., Royon, A., Mounaix, P., Cardinal, T.,Canioni, L., *Adv Funct Mater*, **2014**. *24,* p. 5824-5832.
8. Forcherio, G.T.,Roper, D.K., *Proc Spie Nanophot Mat*, **2014**. *9161,* p. 916115-916115-6.
9. Kim, J., Wang, Z.,Kim, W.S., *Ieee Sens J*, **2014**. *14,* p. 4395-4401.
10. Park, H.I., Lee, S., Lee, J.M., Nam, S.A., Jeon, T., Han, S.W.,Kim, S.O., *Acs Nano*, **2014**. *8,* p. 10305-10312.
11. Youn, H., Lee, T.,Guo, L.J., *Energ Environ Sci*, **2014**. *7,* p. 2764-2770.
12. Bastys, V., Pastoriza-Santos, I., Rodríguez-González, B., Vaisnoras, R.,Liz-Marzán, L.M., *Adv Funct Mater*, **2006**. *16,* p. 766-773.
13. Bhalla, N., Formisano, N., Miodek, A., Jain, A., Di Lorenzo, M., Pula, G.,Estrela, P., *Biosens Bioelectron*, **2015**. *71,* p. 121-128.
14. Kumar, C.S., Raja, M.D., Sundar, D.S., Antoniraj, M.G.,Ruckmani, K., *Carbohyd Polym*, **2015**. *128,* p. 63-74.
15. Savarimuthu, W.P., Gananathan, P., Rao, A.P., Manickam, E.,Singaravelu, G., *J Nanosci Nanotechnol*, **2015**. *15,* p. 5577-5584.
16. Zhao, J.H., Lin, J., Li, X.H., Zhao, G.N.,Zhang, W.J., *Appl Surf Sci*, **2015**. *347,* p. 514-519.
17. Tang, L.J., Li, S., Han, F., Liu, L.Q., Xu, L.G., Ma, W., Kuang, H., Li, A.K., Wang, L.B.,Xu, C.L., *Biosens Bioelectron*, **2015**. *71,* p. 7-12.
18. Olea-Mejia, O., Fernandez-Mondragon, M., Rodriguez-de la Concha, G.,Camacho-Lopez, M., *Appl Surf Sci*, **2015**. *348,* p. 66-70.
19. Li, M.H., Guo, X.Y., Wang, H., Wen, Y.,Yang, H.F., *Sensor Actuat B-Chem*, **2015**. *216,* p. 535-541.
20. Emamian, S., Eshkeiti, A., Narakathu, B.B., Avuthu, S.G.R.,Atashbar, M.Z., *Sensor Actuat B-Chem*, **2015**. *217,* p. 129-135.

21. Ruan, W., Zhou, T., Cui, Y., Dong, Y., Liu, Z., Dong, F., Wang, H., Luan, X., Wang, X., Song, W.,Zhao, B., *Appl Surf Sci*, **2014**. *309,* p. 295-299.
22. Sharma, B., Frontiera, R.R., Henry, A.-I., Ringe, E.,Van Duyne, R.P., *Mater Today*, **2012**. *15,* p. 16-25.
23. Kleinman, S.L., Ringe, E., Valley, N., Wustholz, K.L., Phillips, E., Scheidt, K.A., Schatz, G.C.,Van Duyne, R.P., *J Am Chem Soc*, **2011**. *133,* p. 4115-4122.
24. Fan, M., Andrade, G.F.S.,Brolo, A.G., *Anal Chim Acta*, **2011**. *693,* p. 7-25.
25. Lim, D.-K., Jeon, K.-S., Hwang, J.-H., Kim, H., Kwon, S., Suh, Y.D.,Nam, J.-M., *Nat Nanotechnol*, **2011**. *6,* p. 452-460.
26. Xue, C., Li, Z.,Mirkin, C.A., *Small*, **2005**. *1,* p. 513-516.
27. Georgakilas, V., Perman, J.A., Tucek, J.,Zboril, R., *Chem Rev*, **2015**. *115,* p. 4744-4822.
28. Iijima, S., *Nature*, **1991**. *354,* p. 56-58.
29. Terrones, M., *Annu Rev Mater Res*, **2003**. *33,* p. 419-501.
30. Saito, R., Fujita, M., Dresselhaus, G.,Dresselhaus, M.S., *Appl Phys Lett*, **1992**. *60,* p. 2204-2206.
31. Wildoer, J.W.G., Venema, L.C., Rinzler, A.G., Smalley, R.E.,Dekker, C., *Nature*, **1998**. *391,* p. 59-62.
32. Bockrath, M., Cobden, D.H., McEuen, P.L., Chopra, N.G., Zettl, A., Thess, A.,Smalley, R.E., *Science*, **1997**. *275,* p. 1922-1925.
33. Tans, S.J., Devoret, M.H., Dai, H.J., Thess, A., Smalley, R.E., Geerligs, L.J.,Dekker, C., *Nature*, **1997**. *386,* p. 474-477.
34. Bockrath, M., Cobden, D.H., Lu, J., Rinzler, A.G., Smalley, R.E., Balents, L.,McEuen, P.L., *Nature*, **1999**. *397,* p. 598-601.
35. Ishii, H., Kataura, H., Shiozawa, H., Yoshioka, H., Otsubo, H., Takayama, Y., Miyahara, T., Suzuki, S., Achiba, Y., Nakatake, M., Narimura, T., Higashiguchi, M., Shimada, K., Namatame, H.,Taniguchi, M., *Nature*, **2003**. *426,* p. 540-544.
36. Yao, Z., Postma, H.W.C., Balents, L.,Dekker, C., *Nature*, **1999**. *402,* p. 273-276.
37. Purewal, M.S., Hong, B.H., Ravi, A., Chandra, B., Hone, J.,Kim, P., *Phys Rev Lett*, **2007**. *98,* p. 186808.
38. Bernholc, J., Brenner, D., Nardelli, M.B., Meunier, V.,Roland, C., *Annu Rev Mater Res*, **2002**. *32,* p. 347-375.
39. Itkis, M.E., Perea, D.E., Jung, R., Niyogi, S.,Haddon, R.C., *J Am Chem Soc*, **2005**. *127,* p. 3439-3448.
40. Kataura, H., Kumazawa, Y., Maniwa, Y., Umezu, I., Suzuki, S., Ohtsuka, Y.,Achiba, Y., *Synt Met*, **1999**. *103,* p. 2555-2558.
41. Hartschuh, A., Pedrosa, H.N., Peterson, J., Huang, L., Anger, P., Qian, H., Meixner, A.J., Steiner, M., Novotny, L.,Krauss, T.D., *ChemPhysChem*, **2005**. *6,* p. 577-582.

42. Iakoubovskii, K., Minami, N., Ueno, T., Kazaoui, S.,Kataura, H., *J Phys Chem C*, **2008**. *112,* p. 11194-11198.
43. Iakoubovskii, K., Minami, N., Kazaoui, S., Ueno, T., Miyata, Y., Yanagi, K., Kataura, H., Ohshima, S.,Saito, T., *J Phys Chem B*, **2006**. *110,* p. 17420-17424.
44. Zhao, B., Itkis, M.E., Niyogi, S., Hu, H., Zhang, J.,Haddon, R.C., *J Phys Chem B*, **2004**. *108,* p. 8136-8141.
45. Kurti, J., Zolyomi, V., Gruneis, A.,Kuzmany, H., *Phys Rev B*, **2002**. *65*.
46. Müller, A.,Jansen, M., *Z Anorg Allg Chem*, **2010**. *636,* p. 677-680.
47. Jorio, A., Dresselhaus, G.,Dresselhaus, M.S., *Carbon Nanotubes: Advanced Topics in the Synthesis, Structure, Properties and Applications*. 2007: Springer Berlin Heidelberg.
48. Maser, W.K., Muñoz, E., Benito, A.M., Martínez, M.T., de la Fuente, G.F., Maniette, Y., Anglaret, E.,Sauvajol, J.L., *Chem Phys Lett*, **1998**. *292,* p. 587-593.
49. Shi, Z., Lian, Y., Zhou, X., Gu, Z., Zhang, Y., Iijima, S., Zhou, L., Yue, K.T.,Zhang, S., *Carbon*, **1999**. *37,* p. 1449-1453.
50. Cassell, A.M., Raymakers, J.A., Kong, J.,Dai, H., *J Phys Chem B*, **1999**. *103,* p. 6484-6492.
51. Sanchez-Valencia, J.R., Dienel, T., Groning, O., Shorubalko, I., Mueller, A., Jansen, M., Amsharov, K., Ruffieux, P.,Fasel, R., *Nature*, **2014**. *512,* p. 61-64.
52. Telg, H., Duque, J.G., Staiger, M., Tu, X., Hennrich, F., Kappes, M.M., Zheng, M., Maultzsch, J., Thomsen, C.,Doorn, S.K., *ACS Nano*, **2012**. *6,* p. 904-911.
53. Nicklaus, M., *Tip-Enhanced Raman Spectroscopy for Nanoelectronics*. 2014: Books on Demand.
54. Kalbac, M., Kavan, L.,Dunsch, L., *J Phys Chem C*, **2009**. *113,* p. 1340-1345.
55. Boyd, R.W., *Nonlinear optics*. 3rd ed. Vol. XIX. 2008, Amsterdam; Boston: Academic Press.
56. Chen, S., Zhao, C., Li, Y., Huang, H., Lu, S., Zhang, H.,Wen, S., *Opt Mater Express*, **2014**. *4,* p. 587-596.
57. Garmire, E., *Ieee J Sel Top Quant*, **2000**. *6,* p. 1094-1110.
58. Zitter, R.N., *Appl Phys Lett*, **1969**. *14,* p. 73-74.
59. Silfvast, W.T., *Laser fundamentals*. 2nd ed. 2004, Cambridge; New York: Cambridge University Press.
60. Steinmeyer, G., Sutter, D.H., Gallmann, L., Matuschek, N.,Keller, U., *Science*, **1999**. *286,* p. 1507-1512.
61. Adams, L.E., Ramaswamy, M., Keller, U., Asom, M.T., Fujimoto, J.G.,Kintzer, E.S., *Opt Lett*, **1993**. *18,* p. 1940-1942.
62. Ortaç, B., Schmidt, O., Schreiber, T., Limpert, J., Tünnermann, A.,Hideur, A., *Opt Express*, **2007**. *15,* p. 10725-10732.

63. Akiyama, T., Georgiev, N., Mozume, T., Yoshida, H., Gopal, A.V.,Wada, O., *Electron Lett*, **2001**. *37,* p. 129-130.
64. Okhotnikov, O., Grudinin, A.,Pessa, M., *New J Phys*, **2004**. *6,* p. 177.
65. Keller, U., *Nature*, **2003**. *424,* p. 831-838.
66. Chen, Y.-C., Raravikar, N.R., Schadler, L.S., Ajayan, P.M., Zhao, Y.-P., Lu, T.-M., Wang, G.-C.,Zhang, X.-C., *Appl Phys Lett*, **2002**. *81,* p. 975-977.
67. Elim, H.I., Ji, W., Ng, M.-T.,Vittal, J.J., *Appl Phys Lett*, **2007**. *90,* p. 033106.
68. Savitski, V.G., Malyarevich, A.M., Demchuk, M.I., Yumashev, K.V., Raaben, H.,Zhilin, A.A., *J Opt Soc Am B*, **2005**. *22,* p. 1660-1666.
69. Resasco, D.E., Alvarez, W.E., Pompeo, F., Balzano, L., Herrera, J.E., Kitiyanan, B.,Borgna, A., *J Nanopart Res*, **2002**. *4,* p. 131-136.
70. Lebedkin, S., Schweiss, P., Renker, B., Malik, S., Hennrich, F., Neumaier, M., Stoermer, C.,Kappes, M.M., *Carbon*, **2002**. *40,* p. 417-423.
71. Nikolaev, P., Bronikowski, M.J., Bradley, R.K., Rohmund, F., Colbert, D.T., Smith, K.A.,Smalley, R.E., *Chem Phys Lett*, **1999**. *313,* p. 91-97.
72. Wang, F., Rozhin, A.G., Sun, Z., Scardaci, V., White, I.H.,Ferrari, A.C., *Phys Status Solidi B*, **2008**. *245,* p. 2319-2322.
73. Yamashita, S., Inoue, Y., Maruyama, S., Murakami, Y., Yaguchi, H., Jablonski, M.,Set, S.Y., *Opt Lett*, **2004**. *29,* p. 1581-1583.
74. Il'ichev, N.N., Garnov, S.V.,Obraztsova, E.D., *Aip Conf Proc*, **2005**. *786,* p. 611-615.
75. Fong, K.H., Kikuchi, K., Goh, C.S., Set, S.Y., Grange, R., Haiml, M., Schlatter, A.,Keller, U., *Opt Lett*, **2007**. *32,* p. 38-40.
76. Scardaci, V., Rozhin, A.G., Tan, P.H., Wang, F., White, I.H., Milne, W.I.,Ferrari, A.C., *Phys Status Solidi B*, **2007**. *244,* p. 4303-4307.
77. Shohda, F., Shirato, T., Nakazawa, M., Mata, J.,Tsukamoto, J., *Opt Express*, **2008**. *16,* p. 20943-20948.
78. Shohda, F., Shirato, T., Nakazawa, M., Komatsu, K.,Kaino, T., *Opt Express*, **2008**. *16,* p. 21191-21198.
79. Karousis, N., Tagmatarchis, N.,Tasis, D., *Chem Rev*, **2010**. *110,* p. 5366-5397.
80. Wu, H.C., Chang, X.L., Liu, L., Zhao, F.,Zhao, Y.L., *J Mater Chem*, **2010**. *20,* p. 1036-1052.
81. Xia, W., Jin, C., Kundu, S.,Muhler, M., *Carbon*, **2009**. *47,* p. 919-922.
82. Yu, H., Jin, Y.G., Peng, F., Wang, H.J.,Yang, J., *J Phys Chem C*, **2008**. *112,* p. 6758-6763.
83. Pumera, M., Smid, B.,Veltruska, K., *J Nanosci Nanotechnol*, **2009**. *9,* p. 2671-2676.
84. Bergeret, C., Cousseau, J., Fernandez, V., Mevellec, J.Y.,Lefrant, S., *J Phys Chem C*, **2008**. *112,* p. 16411-16416.
85. Wang, Y.B., Iqbal, Z.,Mitra, S., *J Am Chem Soc*, **2006**. *128,* p. 95-99.

86. Chen, Y.H.,Mitra, S., *J Nanosci Nanotechnol*, **2008**. *8,* p. 5770-5775.
87. Ziegler, K.J., Gu, Z.N., Peng, H.Q., Flor, E.L., Hauge, R.H.,Smalley, R.E., *J Am Chem Soc*, **2005**. *127,* p. 1541-1547.
88. Fagnoni, M., Profumo, A., Merli, D., Dondi, D., Mustarelli, P.,Quartarone, E., *Adv Mater*, **2009**. *21,* p. 1761-1765.
89. Malarkey, E.B., Reyes, R.C., Zhao, B., Haddon, R.C.,Parpura, V., *Nano Lett*, **2008**. *8,* p. 3538-3542.
90. Deng, X., Jia, G., Wang, H., Sun, H., Wang, X., Yang, S., Wang, T.,Liu, Y., *Carbon*, **2007**. *45,* p. 1419-1424.
91. Wu, Z.G., Feng, W., Feng, Y.Y., Liu, Q., Xu, X.H., Sekino, T., Fujii, A.,Ozaki, M., *Carbon*, **2007**. *45,* p. 1212-1218.
92. He, P.,Urban, M.W., *Biomacromolecules*, **2005**. *6,* p. 2455-2457.
93. Sun, Y.-P., Fu, K., Lin, Y.,Huang, W., *Acc Chem Res*, **2002**. *35,* p. 1096-1104.
94. Sun, Y.P., Huang, W.J., Lin, Y., Fu, K.F., Kitaygorodskiy, A., Riddle, L.A., Yu, Y.J.,Carroll, D.L., *Chem Mater*, **2001**. *13,* p. 2864-2869.
95. Riggs, J.E., Guo, Z.X., Carroll, D.L.,Sun, Y.P., *J Am Chem Soc*, **2000**. *122,* p. 5879-5880.
96. Georoakilas, V., Bourlinos, A.B., Zboril, R.,Trapalis, C., *Chem Mater*, **2008**. *20,* p. 2884-2886.
97. Fabre, B., Hauquier, F., Herrier, C., Pastorin, G., Wu, W., Bianco, A., Prato, M., Hapiot, P., Zigah, D., Prasciolu, M.,Vaccari, L., *Langmuir*, **2008**. *24,* p. 6595-6602.
98. Campidelli, S., Sooambar, C., Diz, E.L., Ehli, C., Guldi, D.M.,Prato, M., *J Am Chem Soc*, **2006**. *128,* p. 12544-12552.
99. Bae, J.H., Shanmugharaj, A.M., Noh, W.H., Choi, W.S.,Ryu, S.H., *Appl Surf Sci*, **2007**. *253,* p. 4150-4155.
100. Chen, S.M., Shen, W.M., Wu, G.Z., Chen, D.Y.,Jiang, M., *Chem Phys Lett*, **2005**. *402,* p. 312-317.
101. Mylvaganam, K.,Zhang, L.C., *J Phys Chem B*, **2004**. *108,* p. 15009-15012.
102. Dyke, C.A., Stewart, M.P., Maya, F.,Tour, J.M., *Synlett*, **2004** p. 155-160.
103. Bahr, J.L.,Tour, J.M., *Chem Mater*, **2001**. *13,* p. 3823-3824.
104. Strano, M.S., Dyke, C.A., Usrey, M.L., Barone, P.W., Allen, M.J., Shan, H.W., Kittrell, C., Hauge, R.H., Tour, J.M.,Smalley, R.E., *Science*, **2003**. *301,* p. 1519-1522.
105. Dyke, C.A.,Tour, J.M., *Nano Lett*, **2003**. *3,* p. 1215-1218.
106. Mateo-Alonso, A., Ehli, C., Chen, K.H., Guldi, D.M.,Prato, M., *J Phys Chem A*, **2007**. *111,* p. 12669-12673.
107. Murakami, H., Nomura, T.,Nakashima, N., *Chem Phys Lett*, **2003**. *378,* p. 481-485.
108. Attal, S., Thiruvengadathan, R.,Regev, O., *Anal Chem*, **2006**. *78,* p. 8098-8104.
109. Zhong, W.H.,Claverie, J.P., *Carbon*, **2013**. *51,* p. 72-84.

110. Cambre, S.,Wenseleers, W., *Angew Chem Int Edit*, **2011**. *50,* p. 2764-2768.
111. Di Crescenzo, A., Ettorre, V.,Fontana, A., *Beilstein J Nanotechnol*, **2014**. *5,* p. 1675-1690.
112. Zhang, J., Lee, J.K., Wu, Y.,Murray, R.W., *Nano Lett*, **2003**. *3,* p. 403-407.
113. Gotovac, S., Honda, H., Hattori, Y., Takahashi, K., Kanoh, H.,Kaneko, K., *Nano Lett*, **2007**. *7,* p. 583-587.
114. Wang, X.L., Tao, S.,Xing, B.S., *Environ Sci Technol*, **2009**. *43,* p. 6214-6219.
115. Tromp, R.M., Afzali, A., Freitag, M., Mitzi, D.B.,Chen, Z., *Nano Lett*, **2008**. *8,* p. 469-472.
116. Bonard, J.M., Stora, T., Salvetat, J.P., Maier, F., Stockli, T., Duschl, C., Forro, L., deHeer, W.A.,Chatelain, A., *Adv Mater*, **1997**. *9,* p. 827-831.
117. Attal, S., Thiruvengadathan, R.,Regev, O., *Anal Chem*, **2006**. *78,* p. 8098-8104.
118. Oh, H., Sim, J.,Ju, S.Y., *Langmuir*, **2013**. *29,* p. 11154-11162.
119. Guldi, D.M., Rahman, G.M.A., Jux, N., Balbinot, D., Hartnagel, U., Tagmatarchis, N.,Prato, M., *J Am Chem Soc*, **2005**. *127,* p. 9830-9838.
120. Toma, F.M., Sartorel, A., Iurlo, M., Carraro, M., Rapino, S., Hoober-Burkhardt, L., Da Ros, T., Marcaccio, M., Scorrano, G., Paolucci, F., Bonchio, M.,Prato, M., *Chemsuschem*, **2011**. *4,* p. 1447-1451.
121. Ehli, C., Oelsner, C., Guldi, D.M., Mateo-Alonso, A., Prato, M., Schmidt, C., Backes, C., Hauke, F.,Hirsch, A., *Nat Chem*, **2009**. *1,* p. 243-249.
122. Li, L.C., Zhang, M., Mao, S., Yang, C.,Tian, A.M., *Acta Chim Sinica*, **2015**. *73,* p. 143-150.
123. Maruyama, Y., Motohashi, S., Tanaka, M., Ogata, H., Zhou, B.A., Kobayashi, A., Shoda, M., Bandow, S.,Iijima, S., *Solid State Commun*, **2010**. *150,* p. 1584-1586.
124. Park, J.J., Fagan, J.A., Huh, J.Y., Migler, K.B., Karim, A.,Raghavan, D., *Soft Matter*, **2010**. *6,* p. 5581-5588.
125. Wang, Y.X., *J Phys Chem C*, **2008**. *112,* p. 14297-14305.
126. Kam, N.W.S., O'Connell, M., Wisdom, J.A.,Dai, H.J., *P Natl Acad Sci USA*, **2005**. *102,* p. 11600-11605.
127. Vaisman, L., Marom, G.,Wagner, H.D., *Adv Funct Mater*, **2006**. *16,* p. 357-363.
128. Gong, X.Y., Liu, J., Baskaran, S., Voise, R.D.,Young, J.S., *Chem Mater*, **2000**. *12,* p. 1049-1052.
129. Rouse, J.H., *Langmuir*, **2004**. *21,* p. 1055-1061.
130. Barnes, W.L., Dereux, A.,Ebbesen, T.W., *Nature*, **2003**. *424,* p. 824-830.
131. Brongersma, M.L.,Shalaev, V.M., *Science*, **2010**. *328,* p. 440-441.
132. O'Connor, D.,Zayats, A.V., *Nat Nanotechnol*, **2010**. *5,* p. 482-483.
133. Joachim, C., Gimzewski, J.K.,Aviram, A., *Nature*, **2000**. *408,* p. 541-548.
134. Chang, D.E., Sorensen, A.S., Demler, E.A.,Lukin, M.D., *Nat Phys*, **2007**. *3,* p. 807-812.

135. Chang, D.E., Sorensen, A.S., Hemmer, P.R.,Lukin, M.D., *Phys Rev Lett*, **2006**. *97,* p. 053002.
136. Fang, N., Lee, H., Sun, C.,Zhang, X., *Science*, **2005**. *308,* p. 534-537.
137. Shalaev, V.M., *Nat Photonics*, **2007**. *1,* p. 41-48.
138. Li, M., Cushing, S.K.,Wu, N.Q., *Analyst*, **2015**. *140,* p. 386-406.
139. Dostalek, J.,Knoll, W., *Biointerphases*, **2008**. *3,* p. Fd12-Fd22.
140. Lakowicz, J.R., *Plasmonics*, **2006**. *1,* p. 5-33.
141. Shalaev, V.M., *Nanophotonics with surface plasmons*. 1st ed. ed. 2006, Amsterdam; Oxford: Elsevier.
142. Mayer, K.M.,Hafner, J.H., *Chem Rev*, **2011**. *111,* p. 3828-3857.
143. Willets, K.A.,Van Duyne, R.P., *Annu Rev Phys Chem*, **2007**. *58,* p. 267-297.
144. Li, M., Cushing, S.K., Zhang, J.M., Lankford, J., Aguilar, Z.P., Ma, D.L.,Wu, N.Q., *Nanotechnology*, **2012**. *23*.
145. Haes, A.J., Haynes, C.L., McFarland, A.D., Schatz, G.C., Van Duyne, R.R.,Zou, S.L., *Mrs Bull*, **2005**. *30,* p. 368-375.
146. Nallathamby, P.D., Huang, T.,Xu, X.H.N., *Nanoscale*, **2010**. *2,* p. 1715-1722.
147. Ghosh, S.K.,Pal, T., *Chem Rev*, **2007**. *107,* p. 4797-4862.
148. Li, Y., Zhao, K., Sobhani, H., Bao, K.,Nordlander, P., *J Phys Chem Lett*, **2013**. *4,* p. 1352-1357.
149. Lakowicz, J.R., *Anal Biochem*, **2005**. *337,* p. 171-194.
150. Gryczynski, I., Malicka, J., Gryczynski, Z.,Lakowicz, J.R., *Anal Biochem*, **2004**. *324,* p. 170-182.
151. Dijk, M.A., PhD Thesis *"Nonlinear optical studies of single gold nanoparticles"*, 2007, *Leiden University*
152. Rycenga, M., Cobley, C.M., Zeng, J., Li, W., Moran, C.H., Zhang, Q., Qin, D.,Xia, Y., *Chem Rev*, **2011**. *111,* p. 3669-3712.
153. Le Ru, E.C.,Etchegoin, P.G., *Principles of surface-enhanced Raman spectroscopy : and related plasmonic effects*. 1st ed. 2009, Amsterdam; Boston: Elsevier.
154. Perner, M., Bost, P., Lemmer, U., vonPlessen, G., Feldmann, J., Becker, U., Mennig, M., Schmitt, M.,Schmidt, H., *Phys Rev Lett*, **1997**. *78,* p. 2192-2195.
155. Cao, W.,Elsayed-Ali, H.E., *Mater Lett*, **2009**. *63,* p. 2263-2266.
156. Elechiguerra, J.L., Larios-Lopez, L., Liu, C., Garcia-Gutierrez, D., Camacho-Bragado, A.,Yacaman, M.J., *Chem Mater*, **2005**. *17,* p. 6042-6052.
157. Frederix, F., Friedt, J.M., Choi, K.H., Laureyn, W., Campitelli, A., Mondelaers, D., Maes, G.,Borghs, G., *Anal Chem*, **2003**. *75,* p. 6894-6900.
158. Pastoriza-Santos, I.,Liz-Marzan, L.M., *J Mater Chem*, **2008**. *18,* p. 1724-1737.

159. Kelly, K.L., Coronado, E., Zhao, L.L.,Schatz, G.C., *J Phys Chem B*, **2002**. *107,* p. 668-677.
160. Nelayah, J., Kociak, M., Stephan, O., Garcia de Abajo, F.J., Tence, M., Henrard, L., Taverna, D., Pastoriza-Santos, I., Liz-Marzan, L.M.,Colliex, C., *Nat Phys*, **2007**. *3,* p. 348-353.
161. Brioude, A.,Pileni, M.P., *J Phys Chem B*, **2005**. *109,* p. 23371-23377.
162. Hao, E., Schatz, G.C.,Hupp, J.T., *J Fluoresc*, **2004**. *14,* p. 331-341.
163. Pastoriza-Santos, I.,Liz-Marzán, L.M., *Nano Lett*, **2002**. *2,* p. 903-905.
164. Liz-Marzán, L.M.,Giersig, M., *Low-dimensional systems : theory, preparation, and some applications*. 2003, Dordrecht; London: Kluwer Academic.
165. Sherry, L.J., Jin, R.C., Mirkin, C.A., Schatz, G.C.,Van Duyne, R.P., *Nano Lett*, **2006**. *6,* p. 2060-2065.
166. Feldheim, D.L.,Foss, C.A., *Metal nanoparticles : synthesis, characterization, and applications*. 2002, New York: Marcel Dekker.
167. Yang, L., Osborne, D.H., Haglund, R.F., Magruder, R.H., White, C.W., Zuhr, R.A.,Hosono, H., *Appl Phys a-Mater*, **1996**. *62,* p. 403-415.
168. Balamurugan, B.,Maruyama, T., *J Appl Phys*, **2007**. *102*.
169. Sun, S.H., Murray, C.B., Weller, D., Folks, L.,Moser, A., *Science*, **2000**. *287,* p. 1989-1992.
170. Philip, R., Kumar, G.R., Sandhyarani, N.,Pradeep, T., *Phys Rev B*, **2000**. *62,* p. 13160-13166.
171. Porel, S., Venkatram, N., Rao, D.N.,Radhakrishnan, T.P., *J Appl Phys*, **2007**. *102*.
172. Wang, Q.Q., Han, J.B., Gong, H.M., Chen, D.J., Zhao, X.J., Feng, J.Y.,Ren, J.J., *Adv Funct Mater*, **2006**. *16,* p. 2405-2408.
173. Shi, H.F., Wang, C., Zhou, Y.L., Jin, K.J.,Yang, G.Z., *J Nanosci Nanotechnol*, **2012**. *12,* p. 7896-7902.
174. Whelan, A.M., Brennan, M.E., Blau, W.J.,Kelly, J.M., *J Nanosci Nanotechnol*, **2004**. *4,* p. 66-68.
175. Zheng, C., Du, Y.H., Feng, M.,Zhan, H.B., *Appl Phys Lett*, **2008**. *93*.
176. Ganeev, R.A., Ryasnyansky, A.I., Stepanov, A.L.,Usmanov, T., *Optical and Quantum Electronics*, **2004**. *36,* p. 949-960.
177. Gu, J., Li, Y., Li, W.,Shi, J., *Res Chem Intermediat*, **2009**. *35,* p. 807-816.
178. Bhushan, B., Kundu, T.,Singh, B.P., *Opt Commun*, **2012**. *285,* p. 5420-5424.
179. Luo, S., Chen, Y., Fan, G., Sun, F.,Qu, S., *Appl Phys A*, **2014** p. 1-4.
180. Polavarapu, L., Xu, Q.-H., Dhoni, M.S.,Ji, W., *Appl Phys Lett*, **2008**. *92,* p. 263110-263110-3.
181. Millstone, J.E., Hurst, S.J., Métraux, G.S., Cutler, J.I.,Mirkin, C.A., *Small*, **2009**. *5,* p. 646-664.
182. Shuford, K.L., Ratner, M.A.,Schatz, G.C., *J Chem Phys*, **2005**. *123,* p. 114713.

183. Luo, Y.L., *Mater Lett*, **2007**. *61,* p. 1346-1349.
184. Kelly, K.L., Coronado, E., Zhao, L.L.,Schatz, G.C., *J Phys Chem B*, **2003**. *107,* p. 668-677.
185. Jin, R.C., Cao, Y.W., Mirkin, C.A., Kelly, K.L., Schatz, G.C.,Zheng, J.G., *Science*, **2001**. *294,* p. 1901-1903.
186. Junior, A.M., de Oliveira, H.P.M.,Gehlen, M.H., *Photoch Photobio Sci*, **2003**. *2,* p. 921-925.
187. Jin, R.C., Cao, Y.C., Hao, E.C., Metraux, G.S., Schatz, G.C.,Mirkin, C.A., *Nature*, **2003**. *425,* p. 487-490.
188. Xue, B., Wang, D., Zuo, J., Kong, X.G., Zhang, Y.L., Liu, X.M., Tu, L.P., Chang, Y.L., Li, C.X., Wu, F., Zeng, Q.H., Zhao, H.F., Zhao, H.Y.,Zhang, H., *Nanoscale*, **2015**. *7,* p. 8048-8057.
189. Chen, S.H.,Carroll, D.L., *Nano Lett*, **2002**. *2,* p. 1003-1007.
190. Chen, S.H.,Carroll, D.L., *J Phys Chem B*, **2004**. *108,* p. 5500-5506.
191. Smith, D.K.,Korgel, B.A., *Langmuir*, **2008**. *24,* p. 644-649.
192. Aherne, D., Ledwith, D.M., Gara, M.,Kelly, J.M., *Adv Funct Mater*, **2008**. *18,* p. 2005-2016.
193. Knauer, A., Csaki, A., Fritzsche, W., Serra, C.A., Leclerc, N.,Kohler, J.M., *Chem Eng J*, **2013**. *227,* p. 191-197.
194. Knauer, A., Csaki, A., Moller, F., Huhn, C., Fritzsche, W.,Kohler, J.M., *J Phys Chem C*, **2012**. *116,* p. 9251-9258.
195. Carboni, M., Capretto, L., Carugo, D., Stulz, E.,Zhang, X.L., *J Mater Chem C*, **2013**. *1,* p. 7540-7546.
196. Raman, C.V., *Indian Journal of Physics*, **1928**. *2,* p. 387-398.
197. Fleischmann, M., Hendra, P.J.,McQuillan, A.J., *Chem Phys Lett*, **1974**. *26,* p. 163-166.
198. Moskovits, M., *Solid State Commun*, **1979**. *32,* p. 59-62.
199. Le Ru, E.C., Blackie, E., Meyer, M.,Etchegoin, P.G., *J Phys Chem C*, **2007**. *111,* p. 13794-13803.
200. Wang, Y.Q., Yan, B.,Chen, L.X., *Chem Rev*, **2013**. *113,* p. 1391-1428.
201. Tripp, R.A., Dluhy, R.A.,Zhao, Y.P., *Nano Today*, **2008**. *3,* p. 31-37.
202. Zheng, J.K.,He, L.L., *Compr Rev Food Sci F*, **2014**. *13,* p. 317-328.
203. Fan, M.K., Andrade, G.F.S.,Brolo, A.G., *Anal Chim Acta*, **2011**. *693,* p. 7-25.
204. Haynes, C.L.,Van Duyne, R.P., *J Phys Chem B*, **2001**. *105,* p. 5599-5611.
205. Baker, G.A.,Moore, D.S., *Anal Bioanal Chem*, **2005**. *382,* p. 1751-1770.
206. Wang, Y.S., Polavarapu, L.,Liz-Marzan, L.M., *Acs Appl Mater Inter*, **2014**. *6,* p. 21798-21805.
207. Polavarapu, L.,Xu, Q.H., *Langmuir*, **2008**. *24,* p. 10608-10611.
208. Polavarapu, L.,Liz-Marzan, L.M., *Phys Chem Chem Phys*, **2013**. *15,* p. 5288-5300.
209. Guerrini, L.,Graham, D., *Chem Soc Rev*, **2012**. *41,* p. 7085-7107.
210. Eustis, S.,El-Sayed, M.A., *Chem Soc Rev*, **2006**. *35,* p. 209-217.

211. Rycenga, M., Cobley, C.M., Zeng, J., Li, W.Y., Moran, C.H., Zhang, Q., Qin, D.,Xia, Y.N., *Chem Rev*, **2011**. *111,* p. 3669-3712.
212. Garcia-Leis, A., Garcia-Ramos, J.V.,Sanchez-Cortes, S., *J Phys Chem C*, **2013**. *117,* p. 12397-12397.
213. Fales, A.M., Yuan, H.K.,Vo-Dinh, T., *J Phys Chem C*, **2014**. *118,* p. 3708-3715.
214. Tiwari, V.S., Oleg, T., Darbha, G.K., Hardy, W., Singh, J.P.,Ray, P.C., *Chem Phys Lett*, **2007**. *446,* p. 77-82.
215. Ciou, S.H., Cao, Y.W., Huang, H.C., Su, D.Y.,Huang, C.L., *J Phys Chem C*, **2009**. *113,* p. 9520-9525.
216. Felicia, T., Monica, B., Lucian, B.,Simion, A., *Nanotechnology*, **2007**. *18,* p. 255702.
217. Rodriguez-Lorenzo, L., Alvarez-Puebla, R.A., Pastoriza-Santos, I., Mazzucco, S., Stephan, O., Kociak, M., Liz-Marzan, L.M.,de Abajo, F.J.G., *J Am Chem Soc*, **2009**. *131,* p. 4616-4618.
218. Muniz-Miranda, M., Pergolese, B., Bigotto, A.,Giusti, A., *J Colloid Interf Sci*, **2007**. *314,* p. 540-544.
219. Pazos-Perez, N., Barbosa, S., Rodriguez-Lorenzo, L., Aldeanueva-Potel, P., Perez-Juste, J., Pastoriza-Santos, I., Alvarez-Puebla, R.A.,Liz-Marzan, L.M., *J Phys Chem Lett*, **2010**. *1,* p. 24-27.
220. Lu, G., Li, H.,Zhang, H., *Chem Commun*, **2011**. *47,* p. 8560-8562.
221. Toderas, F., Baia, M., Baia, L.,Astilean, S., *Nanotechnology*, **2007**. *18,* p. 255702.
222. Su, Q.Q., Ma, X.Y., Dong, J., Jiang, C.Y.,Qian, W.P., *Acs Appl Mater Inter*, **2011**. *3,* p. 1873-1879.
223. Zhai, W.L., Li, D.W., Qu, L.L., Fossey, J.S.,Long, Y.T., *Nanoscale*, **2012**. *4,* p. 137-142.
224. Fan, M., Andrade, G.F.S.,Brolo, A.G., *Anal Chim Acta*, **2011**. *693,* p. 7-25.
225. Shiohara, A., Langer, J., Polavarapu, L.,Liz-Marzan, L.M., *Nanoscale*, **2014**. *6,* p. 9817-9823.
226. Zhu, H., Du, M.L., Zhang, M., Wang, P., Bao, S.Y., Zou, M.L., Fu, Y.Q.,Yao, J.M., *Biosens Bioelectron*, **2014**. *54,* p. 91-101.
227. Scarpettini, A.F.,Bragas, A.V., *Langmuir*, **2010**. *26,* p. 15948-15953.
228. Torres, V., Popa, M., Crespo, D.,Calderón Moreno, J.M., *Microelectron Eng*, **2007**. *84,* p. 1665-1668.
229. Yi, Z., Xu, X., Wu, X., Chen, C., Li, X., Luo, B., Luo, J., Jiang, X., Wu, W., Yi, Y.,Tang, Y., *Appl Phys A*, **2013**. *110,* p. 335-342.
230. Wu, S., *J Adhesion*, **1973**. *5,* p. 39-55.
231. Sheik-Bahae, M., Said, A.A., Wei, T.H., Hagan, D.J.,Stryland, E.W.V., *Ieee J Quantum Elect*, **1990**. *26,* p. 760-769.
232. Sheik-bahae, M., Said, A.A.,Van Stryland, E.W., *Opt Lett*, **1989**. *14,* p. 955-957.

233. Chapple, P.B., Staromlynska, J., Hermann, J.A., McKay, T.J.,McDuff, R.G., *J Nonlinear Opt Phys*, **1997**. *6,* p. 251-293.
234. Xia, T., Hagan, D.J., Sheikbahae, M.,Vanstryland, E.W., *Opt Lett*, **1994**. *19,* p. 317-319.
235. Kuzyk, M.G.,Dirk, C.W., *Characterization techniques and tabulations for organic nonlinear optical materials*. 1998, New York: Marcel Dekker.
236. Sakakibara, Y., Rozhin, A.G., Kataura, H., Achiba, Y.,Tokumoto, M., *Jpn J Appl Phys*, **2005**. *44,* p. 1621.
237. Yim, J.H., Cho, W.B., Lee, S., Ahn, Y.H., Kim, K., Lim, H., Steinmeyer, G., Petrov, V., Griebner, U.,Rotermund, F., *Appl. Phys. Lett.*, **2008**. *93,* p. 161106-3.
238. Solodyankin, M.A., Obraztsova, E.D., Lobach, A.S., Chernov, A.L., Tausenev, A.V., Konov, V.I.,Dianov, E.M., *Opt Lett*, **2008**. *33,* p. 1336-1338.
239. Schibli, T., Minoshima, K., Kataura, H., Itoga, E., Minami, N., Kazaoui, S., Miyashita, K., Tokumoto, M.,Sakakibara, Y., *Opt Express*, **2005**. *13,* p. 8025-8031.
240. Wang, F., Rozhin, A.G., Scardaci, V., Sun, Z., Hennrich, F., White, I.H., Milne, W.I.,Ferrari, A.C., *Nat Nanotechnol*, **2008**. *3,* p. 738-742.
241. Kim, H.-J., Choi, H.-J., Nam, S.-M.,Song, Y.-W., *Opt Express*, **2011**. *19,* p. 4762-4767.
242. Stöber, W., Fink, A.,Bohn, E., *J Colloid Interf Sci*, **1968**. *26,* p. 62-69.
243. Kong, J.,Dai, H., *J Phys Chem B*, **2001**. *105,* p. 2890-2893.
244. Sheikbahae, M., Said, A.A., Wei, T.H., Hagan, D.J.,Vanstryland, E.W., *Ieee J Quantum Elect*, **1990**. *26,* p. 760-769.
245. Gurudas, U., Brooks, E., Bubb, D.M., Heiroth, S., Lippert, T.,Wokaun, A., *J Appl Phys*, **2008**. *104,* p. 073107-8.
246. Guang-Hua, F., Shi-Liang, Q., Zhong-Yi, G., Qiang, W.,Zhong-Guo, L., *Chinese Phys B*, **2012**. *21,* p. 047804.
247. Cesca, T., Calvelli, P., Battaglin, G., Mazzoldi, P.,Mattei, G., *Radiat Eff Defect S*, **2012**. *167,* p. 520-526.
248. Wang, X., Nan, F., Liang, S., Zhou, L.,Wang, Q., *Wuhan Univ J Nat Sci*, **2013**. *18,* p. 201-206.
249. Sheik-Bahae, M., Said, A.a., Wei, T.-H., Hagan, D.J.,Stryland, E.W.V., *IEEE J. Quantum Electron.*, **1990**. *26.*
250. Fan, G.H., Qu, S.L., Wang, Q.A., Zhao, C.J., Zhang, L.,Li, Z.G., *J Appl Phys*, **2011**. *109.*
251. Boonstra, A.H.,Bernards, T.N.M., *J Non-Cryst Solids*, **1989**. *108,* p. 249-259.
252. Pilipavicius, J., Kazadojev, I., Beganskiene, A., Melninkaitis, A., Sirutkaitis, V.,Kareiva, A., *Mater Sci-Medzg*, **2008**. *14,* p. 283-287.
253. Guha Thakurta, S.,Subramanian, A., *Colloids Surf A*, **2012**. *414,* p. 384-392.

254. Vincent, A., Babu, S., Brinley, E., Karakoti, A., Deshpande, S.,Seal, S., *J Phys Chem C*, **2007**. *111,* p. 8291-8298.
255. Xiao, J.,Qi, L., *Nanoscale*, **2011**. *3,* p. 1383-1396.
256. Mock, J.J., Smith, D.R.,Schultz, S., *Nano Lett*, **2003**. *3,* p. 485-491.
257. Malinsky, M.D., Kelly, K.L., Schatz, G.C.,Van Duyne, R.P., *J Am Chem Soc*, **2001**. *123,* p. 1471-1482.
258. Zub, Y.L., Stolyarchuk, N.V., Barczak, M.,Dąbrowski, A., *Appl Surf Sci*, **2010**. *256,* p. 5361-5364.
259. Kotkowiak, M., Grześkiewicz, B., Robak, E.,Wolarz, E., *J Phys Chem C*, **2015**. *119,* p. 6195-6203.
260. Yang, S., Zhang, Z., Zhao, J., Yu, Z.,Jiang, H., *Mater Lett*, **2014**. *131,* p. 78-81.
261. Zhao, L., Blackburn, J.,Brosseau, C.L., *Anal Chem*, **2015**. *87,* p. 441-447.
262. Le Ru, E.C., Blackie, E., Meyer, M.,Etchegoin, P.G., *J Phys Chem C*, **2007**. *111,* p. 13794-13803.
263. Cho, W.J., Kim, Y.,Kim, J.K., *Acs Nano*, **2012**. *6,* p. 249-255.
264. Shao, F., Lu, Z.C., Liu, C., Han, H.Y., Chen, K., Li, W.T., He, Q.G., Peng, H.,Chen, J.N., *Acs Appl Mater Inter*, **2014**. *6,* p. 6281-6289.